NUMERICAL MODELLING OF WAVE-STRUCTURE INTERACTION
PROBLEMS THROUGH CFD METHODS

A THESIS SUBMITTED TO
THE GRADUATE SCHOOL OF NATURAL AND APPLIED SCIENCES
OF
MIDDLE EAST TECHNICAL UNIVERSITY

BY

HASAN GÖKHAN GÜLER

IN PARTIAL FULFILLMENT OF THE REQUIREMENTS
FOR
THE DEGREE OF DOCTOR OF PHILOSOPHY
IN
CIVIL ENGINEERING

MARCH 2020

Approval of the thesis:

NUMERICAL MODELLING OF WAVE-STRUCTURE INTERACTION PROBLEMS THROUGH CFD METHODS

submitted by **HASAN GÖKHAN GÜLER** in partial fulfillment of the requirements for the degree of **Doctor of Philosophy in Civil Engineering, Middle East Technical University** by,

Prof. Dr. Halil Kalıpçılar
Dean, Graduate School of **Natural and Applied Sciences**

Prof. Dr. Ahmet Türer
Head of the Department, **Civil Engineering**

Prof. Dr. Ahmet Cevdet Yalçıner
Supervisor, **Civil Engineering, METU**

Assist. Prof. Dr. Cüneyt Baykal
Co-Supervisor, **Civil Engineering, METU**

Examining Committee Members:

Prof. Dr. Yalçın Yüksel
Civil Engineering, Yıldız Technical University

Prof. Dr. Ahmet Cevdet Yalçıner
Civil Engineering, METU

Prof. Dr. Mehmet Ali Kökpınar
Civil Engineering, TED University

Assoc. Prof. Dr. Utku Kanoglu
Aerospace Engineering, METU

Assist. Prof. Dr. Gülizar Özyurt Tarakcıoğlu
Civil Engineering, METU

Date: 12.03.2020

I hereby declare that all information in this document has been obtained and presented in accordance with academic rules and ethical conduct. I also declare that, as required by these rules and conduct, I have fully cited and referenced all material and results that are not original to this work.

Name, Last name : Hasan Gökhan Güler

Signature :

ABSTRACT

NUMERICAL MODELLING OF WAVE-STRUCTURE INTERACTION PROBLEMS THROUGH CFD METHODS

Güler, Hasan Gökhan
Doctor of Philosophy, Civil Engineering
Supervisor: Prof. Dr. Ahmet Cevdet Yalçıner
Co-Supervisor: Assist. Prof. Dr. Cüneyt Baykal

March 2020, 168 pages

The major focus of this study is the computational fluid dynamics (CFD) modelling of wave-structure interaction problems. In the first part of this study, the performance of Haydarpaşa Breakwater under tsunami attack is assessed both experimentally and numerically. It is concluded that the major failure mechanism of this breakwater is the sliding of the crown-wall, and the stability of the stones located at the harbour side is also significant. Design recommendations are given based on the stability of the single stone located at the top layer at the harbour side of the breakwater. Next, the motion and collision of two spherical particles under solitary wave attack are studied both experimentally and numerically. The strengths and weaknesses of the two available CFD solvers used in these studies are discussed.

In the second part of this study, two CFD solvers are developed and validated using OpenFOAM CFD Library regarding the discussions in the first part. Both models are capable of solving flow properties inside the porous medium, capturing the free-surface using the Volume of Fluid (VOF) Method, and linked to wave generation

and absorption boundary conditions previously established in this library. The first CFD solver is based on the body-force immersed boundary method (IBM) for stationary boundaries. VOF method is applied using both algebraic and geometric algorithms in this solver. It is the first time that the geometric method called isoAdvector is used with IBM and within the porous media. This numerical solver is validated against four experimental datasets in comparison with a CFD solver working on conventional body-fitted grids. The second numerical model is based on the cut-cell IBM for both stationary and moving boundaries. This model is the first example that considers the moving boundaries, free-surface, porous media flow and wave generation/absorption in the same numerical model and validated against data from an analytical study.

Keywords: Tsunami, Immersed Boundary Method, Free-surface Capturing, Porous Media Flow

ÖZ

DALGA-YAPI ETKİLEŞİMİ PROBLEMLERİNİN HAD YÖNTEMLERİ İLE SAYISAL MODELLENMESİ

Güler, Hasan Gökhan
Doktora, İnşaat Mühendisliği
Tez Yöneticisi: Prof. Dr. Ahmet Cevdet Yalçıner
Ortak Tez Yöneticisi: Dr. Öğr. Üyesi Cüneyt Baykal

Mart 2020, 168 sayfa

Bu çalışmanın ana odağını dalga-yapı etkileşimi problemlerinin hesaplamalı akışkanlar dinamiği (HAD) yönlemleriyle modellenmesi oluşturmaktadır. Çalışmanın ilk kısmında, Haydarpaşa Dalgakıranı'nın tsunami etkisi altındaki performansı deneysel ve sayısal olarak incelenmiştir. Bu dalgakıranın temel yıkılma mekanizmasının kronman duvarının kayması olduğu ve liman tarafındaki taşların denge durumlarının da etkili olduğu sonucuna ulaşılmıştır. Liman tarafının en üstündeki taşın dengesine bağlı olarak tasarım önerileri verilmiştir. Bunun ardından, iki küresel cismin soliter dalga etkisi altındaki hareketleri deneysel ve sayısal olarak çalışılmıştır. Kullanılan mevcut HAD çözücülerinin güçlü ve zayıf yönleri tartışılmıştır.

Çalışmanın ikinci kısımında, OpenFOAM HAD Kütüphanesi kullanılarak ve birinci kısımdaki tartışmalara odaklanan iki HAD çözücüsü geliştirilmiş ve doğrulanmıştır. Her iki model de gözenekli ortamdaki akım özelliklerini çözme, serbest akım yüzeyini Akışkan Hacmi Yöntemi (AHY) ile belirleme özelliklerine sahiptir ve dalga üretimi/soğurulması işlevleri için bu kütüphanede bulunan sınır koşulları ile ilintilendirilmiştir. İlk HAD çözücüsünde hareket etmeyen sınırlar için gövde

kuvveti batık sınır metodu (BSM) kullanılmaktadır. Bu çözücüde AHY hem cebirsel ve hem de geometrik algoritmalar ile uygulanmıştır. Bu çalışma, isoAdvector isimli geometrik AHY algoritmasının BSM ile birlikte ve gözenekli ortam içerisinde kullanıldığı ilk örnektir. İlk HAD çözücüsü dört ayrı deneysel veri seti kullanılarak ve sınırlara uyumlu çözüm ağları üzerinde çalışan bir HAD çözücüsü ile karşılaştırmalı olarak doğrulanmıştır. İkinci sayısal modelde hareket eden ve etmeyen sınırlar için kesik hücre BSM kullanılmaktadır. Bu model, hareket eden sınırları gözeten, serbest akım yüzeyinin belirlendiği, gözenekli ortamdaki akım özelliklerinin çözülebildiği ve dalga üretimi/soğurulması kapasitesine sahip olan ilk örnektir ve bir analitik çalışmanın sonuçları kullanılarak doğrulanmıştır.

Anahtar Kelimeler: Tsunami, Batık Sınır Metodu, Serbest Akım Yüzeyinin Belirlenmesi, Gözenekli Ortamda Akım

To Ezgi, Ege Barış and my parents…

ACKNOWLEDGMENTS

would like to extend my thanks to my granddad Hasan Hüseyin Özden and my late grandmother Meliha Özden. As being my first teachers, they always directed me to the way of science. I would like to thank Sevinç Doğan for her continuous support and encouragement, who is a part of our family.

I would like to express my sincere thanks to my mother, Canan Güler, my father Mehmet Güler, and my sister Oya Güler. They were always there for me. They never got disappointed under any circumstances, and they always supported me without any question. I am grateful for their support, encouragement, and unconditional love. This study would not be possible without them.

The most special gratitude goes to my wife, Ezgi Güler. During the last six years, she never gave up supporting me even if I had to go to Japan for a long time one month after we got married. It is impossible to count how many times I had to stole from our spare time to work more. I am grateful for her love, patience, and encouragement. It would be impossible to finish this study without her. I would like to extend my gratitude to my son Ege Barış Güler who uniquely contributed this study within his first 43 days in life. His presence motivated me a lot and made it easier to overcome stress during the last month when I am writing this thesis study.

TABLE OF CONTENTS

LIST OF TABLES

LIST OF FIGURES

FIGURES

LIST OF ABBREVIATIONS

ABBREVIATIONS

CFD	Computational Fluid Dynamics
ADV	Acoustic Doppler Velocimeter
BiCGSTAB	Bi-Conjugate Stabilized Gradient
CS	Control Surface
CV	Control Volume
DEM	Discrete Element Method
FS	Factor of Safety
GCI	Grid Convergence Index
IB	Immersed Boundary
IBM	Immersed Boundary Method
MAC	Marker and Cell
MMFVM	Moving Mesh Finite Volume Method
MULES	Multidimensional Universal Limiter with Explicit Solution
OpenFOAM	Open-source Field Operation and Manipulation
PG	Pressure Gauge
PARI	Port and Airport Research Institute
PISO	Pressure Implicit with Splitting Operator
RANS	Reynolds-Averaged Navier-Stokes
SPH	Smoothed Particle Hydrodynamics
SST	Shear Stress Transport
VARANS	Volume-Averaged Reynolds-Averaged Navier-Stokes
VOF	Volume of Fluid
WG	Wave Gauge

LIST OF SYMBOLS

SYMBOLS

α	VOF indicator function
α_x	Calibration factor of the VOF indicator function
ε	Difference between fine and coarse grids
γ_v	Volumetric porosity
γ_x	Permeability coefficient in x-direction
γ_y	Permeability coefficient in y-direction
γ_z	Permeability coefficient in z-direction
$\left(\gamma_s\right)_m$	Unit weight of stone in model scale
$\left(\gamma_s\right)_p$	Unit weight of stone in prototype scale
$\left(\gamma_w\right)_m$	Unit weight of water in model scale
$\left(\gamma_w\right)_p$	Unit weight of water in prototype scale
ω	Angular frequency
ω_{pi}	Angular velocity of the particle
ω_{osc}	Frequency of the oscillation
ϕ	A generic variable
ϕ_{rep}	Angle of repose
η	Water surface elevation
η_r	Reflected surface elevation
η_{wave}	Wave profile
θ	Structure slope angle
λ_v	Volumetric porous body model coefficient
λ_x	Porous body model coefficient in x-direction

λ_y	Porous body model coefficient in y-direction
λ_z	Porous body model coefficient in z-direction
λ_W	Weight scale
λ_L	Length scale
λ_T	Time scale
ξ	Paddle trajectory
ζ_n	Coefficient of viscous dashpot in normal direction
ζ_t	Coefficient of viscous dashpot in tangential direction
ρ	Density (water in general)
ρ_l	Density of liquid phase
ρ_g	Density of gas phase
ρ_s	Density of stone
ρ_G	Density of air
$\hat{\rho}_G$	Material derivative of the density of air
μ	Molecular dynamic viscosity
μ_{eff}	Efficient dynamic viscosity
μ_l	Molecular dynamic viscosity of liquid phase
μ_g	Molecular dynamic viscosity of gas phase
μ_s	Static friction coefficient
ν_e	Effective kinematic viscosity
υ_{turb}	Turbulent kinematic viscosity
τ_{ij}	Stress tensor
Ω	Volume
A	Linear closure parameter
a	Linear friction parameter

a_{osc}	Amplitude of the oscillation
A_e	Eroded area
B	Non-linear closure parameter
b	Non-linear friction parameter
c	Wave celerity
C	Added mass coefficient
C_D	Drag coefficient
C_M	Inertia coefficient
C_L	Lift coefficient
d_{center}	Distance of between the center of cylinder and free-surface
d_n	Displacement in normal direction
d_t	Displacement in tangential direction
D_{n50}	Nominal stone diameter
D_x	Wave dissipation parameter in x-direction
D_y	Wave dissipation parameter in y-direction
D_z	Wave dissipation parameter in z-direction
E	Fine grid Richardson error estimator
f_n	Normal force
f_s	Friction force
f_t	Tangential force
$f_{wp,i}$	Wave pressure forces acting on a particle
F_D	Drag force
F_H	Horizontal transferred force
F_I	Inertia force
F_i	Body-force
F_L	Lift force
F_{pi}	Forces acting on the particle

F_x	Pressure forces in x-direction
F_z	Pressure forces in z-direction
g	Acceleration of gravity
h	Tsunami overflow height
h_{water}	Water depth
H	Solitary wave height
$\vec{i}$	Unit vector in ith direction
I	Inertia of the particle
$\vec{j}$	Unit vector in jth direction
k	Wave number
k_{decay}	Outskirt decay coefficient
k_{mom}	Moment arm
k_n	Elastic spring coefficient in normal direction
k_t	Elastic spring coefficient in tangential direction
KC	Keulegean-Carpenter number
m	Mass of the particle
$M_{driving}$	Driving moments
$M_{resisting}$	Resisting moments
n	Porosity
$\vec{n}$	Unit vector
p	Pressure
p_0	Reference atmospheric pressure
$\langle p \rangle^f$	Intrinsic Pressure
R	Rolling parameter
R_{gas}	Gas constant
R_x	Resistance term due to porous media in x direction
R_y	Resistance term due to porous media in y direction

R_z	Resistance term due to porous media in z direction
S	Sliding parameter
S_d	Damage parameter
S_u	Wave generation parameter in x-direction
S_v	Wave generation parameter in y-direction
S_w	Wave generation parameter in z-direction
S_α	Wave generation parameter in VOF-advection equation
S_ρ	Wave generation parameter in material derivative of the air density equation
t	Time
T	Non-dimensional time
T_{emp}	Temperature
T_0	Period of the oscillation
T_{pi}	Torque acting on the particle
$\langle u_i \rangle$	Volume-averaged velocity
$\langle u_i^r \rangle$	Volume averaged compression velocity
u	Velocity in x-direction
u_i	Velocity in ith direction
u_{pi}	Wave generation parameter in VOF-advection equation
u_M	Maximum oscillatory velocity
U	Uniform horizontal velocity
U_{ave}	Average flow velocity
U_c	Correction velocity
U_{IP}	Velocity at the image point
U_m	Velocity below the tsunamis
$U_{particle}$	Particle velocity

v	Velocity in y-direction
v_n	Particle velocity in normal direction
v_t	Particle velocity in tangential direction
$\vec{v}$	Velocity vector
$\vec{v}_b$	Velocity vector of a moving body
V	Velocity of the cylinder
Y	Surface
w	Velocity in z-direction
$W' = W_{sub}$	Submerged weight of stone

CHAPTER 1

INTRODUCTION

1.1   General Description and Objectives of the Study

Accurate prediction of the wave impact on coastal structures is a key element for coastal engineers. Interaction of waves with coastal structures has been widely studied experimentally starting from the early works of Sainflou (1928) on vertical wall breakwaters and Hudson (1959) on rubble mound breakwaters. There is still a tremendous amount of experimental work trying to answer many research questions remaining regarding the physics behind these impacts. Moreover, a significant part of these works try to optimize previous approaches using the new opportunities in the laboratory environments and also based on the accumulation of knowledge.

On the other hand, the use of computational fluid dynamics (CFD) tools for solving the wave-structure interaction problems gained popularity in the last two decades as it is often easier and cheaper to conduct numerical simulations using well-established CFD tools under different design and environmental conditions compared to the physical model experiments. Besides, it is possible to predict and visualize flow properties in microscopic scales with CFD solvers, which is almost impossible to measure in the laboratory environment. Even if the computational time is still a significant barrier, full-scale simulations are also accomplishable.

Most of the well-established CFD solvers focusing on wave-structure interaction problems are capable of solving flow properties around the coastal structures, including the flow properties inside the porous regions of these structures, when the coastal structure does not suffer from damage due to the wave attack. However, it is still challenging to estimate damage on a coastal structure, although it is theoretically

possible and there are some attempts to overcome this challenge. The major problems are to compute the flow properties when the structural elements are moving due to the wave impact and to predict the motion and interaction of structural elements. It might be possible to predict the damage on the coastal structures under wave attack by coupling CFD solvers with i) structural stability solvers for structural elements such as caissons and crown-walls or ii) particle motion/interaction solvers for structural elements such as rubble stones and artificial units. Thus, it would be possible to develop a numerical model that would be directly used for the design of the coastal structures. Although the present state-of-art is promising, there is a long way to develop a single numerical model that covers all the possible failure mechanisms of coastal structures, which might be used directly as a design tool.

This thesis study is focused on the numerical modelling of the wave-structure interaction using CFD tools based on the conventional methods in addition to the immersed boundary method. The wave action is limited to solitary waves, tsunami overflow, and dam-break waves; therefore, the context of this study can also be regarded as numerical modelling of tsunami-structure interaction. Both impermeable and permeable structures (or structural elements) are taken into consideration; however, the main focuses of this study are rubble mound breakwaters and the forces on their structural units. A particular emphasis is given on the algorithms used for capturing the free-surface. The primary objectives of the study are given as follows:

1. To assess tsunami attack on a rubble mound breakwater with an available CFD solver and to develop design recommendations based on the numerical results in comparison with the experimental data

2. To numerically model the motion and collision of the structural elements under solitary wave action using an available CFD solver coupled with a particle motion solver

3. To discuss the strengths and weaknesses of the available CFD solvers that are used to achieve the first two objectives

4. To establish CFD solvers based on the immersed boundary method for not-moving and moving boundaries that might encounter the weaknesses of the available numerical solvers

5. To validate the developed CFD solvers using the available experimental data

In addition to the major objectives listed above, there are several secondary objectives of this study came out as byproducts of the primary objectives given as follows:

1. To discuss the effect of the different free-surface capturing algorithms

2. To discuss the effect the discretization schemes of convection terms, turbulence modelling and air compressibility in accurately predicting impact pressures

1.2   Contents of the Chapters

This study is structured in two main parts, in addition to Chapter 2, which summarizes the literature on wave-structure interaction in scope of the present study. In the first part (Chapters 3 and 4), the available CFD solvers are applied to achieve the first three primary objectives. This part can be regarded as an introduction to CFD modelling of wave-structure interaction where the strengths and weaknesses are presented, and the need for the new numerical solvers are discussed. In the second part of the study (Chapters 5 and 6), the developed CFD solvers in this study are presented in detail, and these solvers are validated against the available experimental data. The second part of this study is planned to focus on the remaining primary objectives and the secondary objectives.

In *Chapter 2*, the summary of the available literature is presented in two steps. First, physical model experiments in the scope of this thesis study are reviewed. Secondly, the theoretical background for the main components of a CFD solver that should be presented for wave-structure problems is summarized, referring to the related

literature. Besides, the applications of these solvers are presented in particular for tsunami-structure interaction problems. Furthermore, the particle motion solvers are discussed based on the available literature. The present information on the coupling of the CFD solvers with the particle motion solvers are briefly summarized given.

In *Chapter 3*, the tsunami attack on a rubble mound breakwater is studied both experimentally and numerically. In the first part of this chapter, the physical model experiments conducted on Haydarpaşa rubble mound breakwater are presented. In the second part of this chapter, the numerical assessment study carried out using a widely used CFD solver called IHFOAM (Higuera et al., 2014a, 2014b) is presented in comparison with the physical model experiments. The Volume Averaged Reynolds Averaged Navier-Stokes (VARANS) equations are solved in this solver to account for the porous media flow. As the VARANS equations are firstly introduced here, these equations are described in detail in this chapter, and referred from the following chapters whenever required. In the numerical modelling part, the forces on the single rubble stone at the top layer of the harbour side of the breakwater are also computed based on the results of numerical simulations to predict the damage on the rubble mound breakwater and to provide design recommendations. Furthermore, the impact of a potential tsunami on the same breakwater is also studied numerically, noting that it is not possible to create this potential wave in a wave channel with the current state-of-art. The physical modelling and numerical modelling parts of this study are previously presented by Guler et al. (2015) and Guler et al. (2018a), respectively.

Although it is possible to use IHFOAM to evaluate forces on the rubble stones, it is seen that a numerical model is required that evaluates the motion and the collision of the rubble stones to predict the damage along the rubble slopes. Therefore, in *Chapter 4*, a numerical model called CADMAS-2VF-DEM (Arikawa et al., 2011) coupling a CFD solver and a particle motion solver based on the Discrete Element Method (DEM) is used to predict the motion and the collision of the particles. A simple study focusing on the motion and the collision of two spheres under solitary wave attack is studied both experimentally and numerically. The particle motion

solver is slightly improved in order to study this selected case numerically. CADMAS-2VF-DEM is regarded as a non-resolving or weakly-coupled numerical solver since the solid particles inside the computational domain are recognized as porous regions at the CFD solver side. Therefore, the flow field around these particles is not resolved properly. Although this approach is applicable for engineering purposes, it is not possible to simulate the same hydrodynamic conditions in the physical model experiments as the particles are represented as porous regions instead of being represented as solid particles. Both the experimental and numerical studies given in this chapter are previously presented by Guler et al. (2018b).

In *Chapter 5*, the major aim is to develop a CFD solver using an appropriate technique that makes it possible to strongly-couple this CFD solver with a particle motion solver in future studies. This technique is selected as the immersed boundary method, which makes it possible to resolve the flow field around the solid particles. As a starting point, a new CFD solver called ibmPorFoam is developed for not-moving boundaries solving VARANS equations based on the body-force immersed boundary method using OpenFOAM CFD library. It is noticed that the body-force IBM is not robust enough for moving boundary calculations. Therefore, rubbleFoam is developed as a new CFD solver that solves VARANS equations based on the cut-cell immersed boundary method for moving boundaries using OpenFOAM CFD library. It is noted that both of the models are capable of simulating the flow field inside the porous regions as VARANS equations are solved with both of them. The free-surface is captured using the Volume of Fluid (VOF) method in both models; however, the solution algorithms for the VOF method differ as described in this chapter. Finally, both models are linked to wave generating/absorbing boundary conditions previously presented by Higuera et al. (2013). In *Chapter 5,* after a general description of OpenFOAM CFD library, theoretical backgrounds and implementation details of both ibmPorFoam and rubbleFoam are presented.

In *Chapter 6*, the validation studies of the newly developed CFD solvers are presented. ibmPorFoam is validated against four experimental datasets using the

solver with two different VOF solution algorithms for all the cases. Also, all the cases are also studied using IHFOAM. Therefore, three different simulations and the experimental data are compared. In particular, extra simulations are carried out for one of the validation cases that involves pressure measurements to discuss the effect of the discretization schemes, turbulence modelling and air compressibility on predicting impact pressure. It is noted that the development and validation of ibmPorFoam is partly presented in Guler et al. (2018c). On the other hand, rubbleFoam is validated against data from an analytical study. Also, a test study is presented.

In *Chapter 7*, the present study is summarized and the major conclusions are presented. Furthermore, the recommendations for the future development of the presented CFD solvers are stated.

CHAPTER 2

LITERATURE REVIEW

Solving wave-structure interaction problems and predicting the forces acting on the structures under wave/flow conditions using a numerical model reminds the famous claim of Marquis Pierre Simon de Laplace known as "Laplace's Demon". According to Laplace (1820), it would be possible to use the laws of physics to predict positions of all the objects in the future, if the exact positions and the speed of all objects in the universe are somehow known at some time. Even if Laplace's claim was disproved later on especially by Heisenberg's Uncertainty Principle (Heisenberg, 1927), it still seems plausible to develop numerical models with a multiphysics approach in the world of Newtonian physics under certain assumptions for design and evaluation of coastal areas and coastal structures.

The present state-of-art tackles many problems to achieve such a multiphysics model. In this chapter, a literature review is presented addressing some of these problems in the scope of this thesis study. The major focus of this thesis study is numerical modelling of wave-structure interaction. However, physical model experiments were carried out presented in Chapters 3 and 4 in the scope of this study. Therefore, this chapter starts with a section devoted to the physical model experiments that are limited to the context of the tests conducted in this study. In the second part of this chapter, an introduction to computational fluid dynamics tools and particle motion solvers are given presenting both theoretical and practical aspects. In both parts, the type of waves is limited to tsunamis in general, as the simulations carried out in this study are focusing on the solitary waves and dam-break flow.

2.1 Physical Modelling

2.1.1 Physical Model Experiments on Tsunami-Rubble Mound Breakwater Interaction

Physical model experiments on tsunami-rubble mound breakwater interaction are reviewed in this section in relation to Chapter 3. There are many studies focusing on the assessment of tsunami impact on seawalls, vertical wall breakwaters, etc. However, there is a limited number of studies focusing on tsunami-rubble mound breakwaters. Esteban et al. (2013) studied the stability of armour units of rubble mound breakwaters against solitary wave attack with small scale experiments and derived Hudson-type stability formula. Sakayima (2013) carried out an experimental and numerical study on the flow fields of tsunamis passing over a rubble mound breakwater. Guler et al. (2015) conducted solitary wave and tsunami overflow experiments on a rubble mound breakwater. This study is a part of this thesis presented in Chapter 3. Harbitz et al. (2016) tested a cross-section based on the cross-section tested in Guler et al. (2015) under solitary wave and tsunami bore impact. More recently, Aniel-Quiroga et al. (2018) conducted physical model experiments with solitary waves and tsunami overflow to assess the stability of the rubble mound breakwaters. Later, Aniel-Quiroga et al. (2019) investigated the pressure forces on the crown-wall of the breakwater cross-section in the previous reference due to the tsunami impact.

2.1.2 Physical Model Experiments on the Motion of the Spherical Particles in Fluids

Experimental studied on the motion of the spherical particles in fluids are reviewed in this section in relation with Chapter 4. In the literature, the motion of solid spherical particles in viscous fluids is investigated in two parts, namely particle-wall interactions and particle-particle interactions. All the fluids in these experiments are

stationary in the beginning. In the first study investigating particle-wall interaction by McLaughin (1968), the motion of steel spherical particles freely falling in glycerin and their interaction with a steel wall was studied. Later, Barnocky and Davis (1988) and Davis et al. (2002) studied the collision of spherical particles with a viscous film. Davis et al. (1986), Ten Cate et al. (2002) and Pianet et al. (2007) studied the motion of spheres having different sizes in a viscous fluid and their interaction with walls. Gondret et al. (1999) and Gondret et al. (2002) investigated the motion of spherical particles produced from different materials in various viscous fluids and their interaction with walls. Zenit and Hunt (1999), Joseph et al. (2001), Joseph (2003) studied the motion of steel and glass spheres having various sizes in water and glycerol, and their interaction with a wall.

On the other hand, Zhang et al. (1999) studied the collision of two elastic spherical particles in a viscous fluid where one of the spheres freely falling on the other sphere that is fixed. Donahue et al. (2010a, 2010b) assessed the collision of three spherical particles in a viscous fluid.

Although the motion of the spherical particles in fluids is investigated widely, their motion under wave attack is not studied until recently. Guler et al. (2018b), Chapter 4 of the present thesis study, studied the motion and collision of two spherical particles (billiard balls with 6 cm diameter) under solitary wave attack. Later, Goral et al. (2020) extended these experiments using different spherical particles having a diameter of 10 cm produced from aluminium and changed the experimental conditions such as the number of particles (one or two), bottom configuration (porous or impermeable), water depth (dry or half-depth condition) and type of the wave (breaking or non-breaking).

2.2 Numerical Modelling

2.2.1 Computational Fluid Dynamics Modelling

Both Eulerian and Lagrangian approaches are used in the computational fluid dynamics (CFD) solvers. Most popular Eulerian methodologies are finite difference method, finite volume method and finite element method. Basically, a fixed grid is used to discretize governing equations in these techniques. On the other hand, there are Lagrangian approaches such as Smoothed Particle Hydrodynamics (SPH) in which the motion of flow is simulated tracking the motion of particles representing fluid and solid regions. In this study, the literature review is limited to Eulerian methodologies.

In CFD simulations, one of the first questions is the dependency of the solution to mesh resolution. This section starts with a subsection presenting a common methodology used to answer this question. On the hand, CFD simulations of wave-structure interaction problems comprise of complexities such as impervious boundaries, porous regions and the interface in between liquid and gas phases. Solving the flow properties within these complexities, capturing/tracking the motion of the free surface and wave generation and absorption at the boundaries of the computational domain are the main computational challenges that must be addressed appropriately to solve the wave-porous structure interaction problems in a reasonable accuracy. In the sub-sections after the discussion on the dependency of the solution to mesh resolution, a literature review on these challenges is presented. CFD applications focusing on tsunami-structure interaction are given as a final sub-section.

2.2.1.1 The Dependency of the CFD Solution to Mesh Resolution

A methodology given by Roache (1998) is used throughout this thesis study to make sure that the numerical solution is independent of the grid resolution. This method is

referred to as Grid Convergence Index (GCI) analysis. GCI is based on Richardson extrapolation comparing the solution at two different grid size. The Richardson error estimator for fine grids is given by Equation 2.1:

$$E = \left[\frac{\varepsilon}{1 - r^p} \right] \quad where \quad \varepsilon = f_2 - f_1 \qquad \text{Eq. 2.1}$$

In Equation 2.1, E is the fine grid Richardson error estimator; r is the refinement factor between the coarse and fine grid; p is the formal order of accuracy of the algorithm; f_2 is the result of a coarse grid simulation and f_1 is the result of a fine grid resolution. Unless otherwise stated, r is taken as 2 as recommended by Roache (1998). Based on the Richardson error estimator, GCI is calculated using Equation 2.2.

$$GCI = FS|E| \qquad \text{Eq. 2.2}$$

In Equation 2.2., FS is the factor of safety. It is taken as 3 throughout this study as recommended by Roache (1998).

In this analysis, the differences in the peaks of the flow properties are usually considered. In the present thesis study, the differences throughout the time-series of all parameters are compared, and it is tried to keep the maximum GCI along the time-series below 2%.

2.2.1.2   Porous Media Modelling

The porous media modelling approaches are grouped as macroscopic and microscopic approaches (Losada et al., 2016). In macroscopic approach, modified flow equations are solved volume-averaging the flow properties disregarding the actual geometry to determine the flow properties inside the porous media (among others Liu et al., 1999; Arikawa et al., 2008; Higuera et al., 2014a-2014b; Jensen et al., 2014). Small-scale variations due to porous media heterogeneities and pore

irregularities are smoothed in this approach while the mean flow properties are mostly captured accurately.

On the other hand, in the microscopic approach, the actual geometry of structural units forming a porous region is constructed in the computational domain to solve flow properties inside the porous media (Dentale et al., 2014a-2014b; Wu et al., 2014; Xu and Liu, 2017). In this approach, each structural unit is treated as impervious solid boundaries. Although the microscopic approach is theoretically more accurate, it is rarely preferred as the conventional body-fitted mesh generation is relatively challenging, and the computational demand of this method is much higher. On the other hand, the microscopic approach might be used more frequently in the next decades as it is required to consider the actual geometry of the structure (e.g.: a rubble mound breakwater) in the computational domain when evaluating the forces on the structural units (e.g.: armour layer stones of the rubble mound breakwater) (Latham et al., 2013). It is noted that it would be easier to implement the microscopic approach with an immersed boundary method with a relatively simple mesh generation procedure.

2.2.1.3   Immersed Boundary Methods

Conventionally, body conformal meshes are generated to model flow around the impervious solid boundaries in computational fluid dynamics (CFD) applications. Alternatively, immersed boundary methods (IBM) that are firstly developed by Peskin (1972) can be used. Udaykumar et al. (2001) and Mittal and Iaccarino (2005) state that the significant advantage of the IBMs is the simplicity in mesh generation compared to generating body conformal mesh configurations, especially when there are complex solid boundaries. Moreover, IBMs make it easier to work with moving boundaries since it is not required to regenerate the mesh configuration when the solid boundaries change their position as in the case of numerical models based on body conformal mesh configurations (Tezduyar, 2001). In surface water wave-structure interaction problems, IBM is preferred to represent relatively complex

geometries (Suzuki and Arikawa, 2010; Grigoriadis et al., 2012; Nielsen et al., 2013), and used to simulate flow field around moving objects (Peng et al., 2012; Zhang et al., 2013; Bihs and Kamath, 2017).

There is a limited number of studies solving porous media flow in combination with IBM. In Van Gent et al. (1994), the model given by Petit et al. (1994) that used IBM was extended to account for the porous media. In Nielsen et al. (2013), a porous media model was combined with an IBM to simulate the flow around offshore wind turbine foundations. Jensen (2014) developed a numerical model using the IBM based on body-force approach (Liu, 2013, 2014) modifying the porous media model presented by Jensen et al. (2014). This numerical model was successfully applied in resolving unidirectional flow past a cylinder and a sphere, flow around the rock toe of a porous breakwater (Jensen, 2014), and flow around stone cover layers on a flatbed (Jensen et al., 2017).

2.2.1.4 Free-Surface Capturing/Tracking

Interface capturing/tracking methodologies are widely studied in the literature for multiphase flows. In the scope of this study, these methodologies are referred to as free-surface capturing/tracking algorithms. These methodologies are usually presented in two groups (Ferziger and Peric, 2002):

i) Free-surface tracking: A boundary-fitted grids are used and advanced at each time step as the free-surface is moved. Well-known examples of this approach are Marker and Cell (MAC) method (McKee et al., 2008) and front-tracking method (Tryggvason et al., 2011).

ii) Free-surface capturing: A fixed grid is used where the fraction of the fluids in the cells around the interface are computed based on an advection equation. The free-surface capturing methodologies are the Volume of Fluid (VOF) Method (Hirt and Nichols, 1981) and Level-Set Method (Sethian,

1999). Bilger et al. (2017) reported that both models are accurate in capturing free-surface with proper implementation and calibration.

In the present study, the VOF method is used for free-surface capturing. The VOF-advection equation is originally derived using the continuity equation; therefore, it is referred to as an additional continuity equation in some references (Higuera, 2015). In the VOF method, an indicator function is defined in each computational cell. This function takes a value between 0 and 1 according to the volumetric fraction of the fluid inside the cell. In the scope of liquid-gas interfaces, the value of the indicator function takes a value of 1, when the computational cell is full of liquid, and 0 if the cell is full of gas. Two approaches are used to capture free-surface using the VOF method: i) Geometric, ii) Algebraic approaches.

In the geometric approach, the interface is firstly reconstructed in each computational cell based on the knowledge of VOF indicator function. After that, the reconstructed interface is advected by computing the fluxed volume across each computational cell (Mirjalili et al., 2017). On the other hand, in the algebraic approach, the VOF-advection equation is solved using numerical approximations computing the fluxes algebraically without need for geometric reconstruction as stated by Mirjalili et al. (2017).

As the numerical models established and used in the present thesis study are mostly based on the OpenFOAM CFD library, the free-surface capturing algorithms given in this library are also reviewed. In OpenFOAM, the VOF method is applied with an algebraic solution algorithm called Multidimensional Universal Limiter with Explicit Solution (MULES) starting from the very early versions of the library. Limiter functions are used in this algebraic algorithm bounding the VOF indicator function between 0 and 1 (Deshpande et al., 2012). On the other hand, Roenby et al. (2016) recently proposed a geometric VOF algorithm referred to as isoAdvector algorithm implemented in OpenFOAM CFD library. isoAdvector algorithm resolves the interface geometrically. Roenby et al. (2016) showed that isoAdvector algorithm significantly improves the accuracy of the results compared to the MULES in the

scope of the test cases presented in that study. Larsen et al. (2019) also reported significant improvements by isoAdvector algorithm when the cases involving progressive waves and relatively longer propagation distances are considered.

2.2.1.5   Wave Generation and Absorption

Most of the advanced wave generation toolboxes included in various CFD models (Isobe et al., 1999; Jacobsen et al., 2012; Higuera et al., 2013) are capable of generating regular and irregular waves. For the generation of various regular waves, the references presented in Table 2.1 are used in various toolboxes.

Table 2.1 Wave generation methods for regular waves

Wave Theory	References
Stokes I and II waves	Dean and Dalyrmple (1991)
Stokes V waves	Skjelbreia and Hendrickson (1960)
Cnoidal waves	Svendsen (2006)
Streamfunction theory	Fenton (1988)
Solitary waves	Boussinesq theory presented by Lee et al. (1982)

On the other hand, there are two main approaches for wave absorption: i) Passive wave absorption ii) Active wave absorption. In the passive wave absorption, a relaxation zone is defined at the boundaries of the computational domain, where the waves are absorbed. The most important disadvantage of the passive wave absorption methodology used by Wei and Kirby (1995), Pengzhi and Liu (1999), Lara et al. (2006), Losada et al. (2008) and Jacobsen et al. (2012) is the unphysical increase in the mean water level due to the presence of the relaxation zones (Mendez et al., 2001). In the active wave absorption methodology, the target wave profile is achieved by modifying the inputted velocity profiles according to the velocity profiles reflected from the boundaries inside the computational domain. Active wave absorption in the numerical models works in a similar way to the wave generators having active wave absorption capabilities in the physical wave flumes. The theory

given by Schaffer and Klopman (2000) is mostly adopted in the active wave absorption toolboxes such as Higuera et al. (2013).

2.2.1.6 Applications of CFD Solvers to Tsunami-Structure Interaction Problems

Small-scale CFD simulations became more popular especially after the Great East Japan Tsunami in 2011, as the tsunami caused vital damage in many bridges, seawalls, dikes and breakwaters in an unexpected manner (Suppasri et al., 2016). CFD simulations are usually used to estimate the flow properties around these damaged structures and to evaluate the forces acting on these structures for a better understanding of the failure mechanisms.

Both Eulerian and Lagrangian CFD solvers are used to estimate forces and/or damage mechanisms of bridges and coastal defence structures such as seawalls and composite breakwaters induced by tsunami impact. Hsiao and Lin (2010) used a Reynolds-Averaged Navier-Stokes (RANS) solver tracking the free surface using volume of fluid (VOF) method to simulate tsunami-like solitary waves impinging and overtopping an impermeable seawall. Several researchers focused on the damage mechanism of Kamaishi Breakwater (Japan) due to 2011 Tsunami using RANS solvers tracking free surface using VOF method (Arikawa et al., 2012; Bricker et al., 2013; Pringle et al., 2016). Scouring around the coastal structures due to tsunami overflow has also been studied. Wang et al. (2016) studied scouring at the rear side of a seawall due to tsunami overflow using incompressible smoothed particle hydrodynamics (ISPH) method. Analyses on tsunami forces acting on bridges and damage mechanisms of bridges due to tsunami impact also carried out in the literature. Bricker and Nakayama (2014) estimated forces on a bridge in the Tohoku Region (Japan) due to the 2011 Tsunami solving RANS equations and tracking free surface by the VOF method. Azadbakht and Yim (2014) used finite element method to solve Navier-Stokes equations, and tracked free surface using an arbitrary Lagrangian-Eulerian (ALE) method to estimate tsunami forces on several bridges

located in California, USA. Salem et al. (2014) used applied element method to analyze the collapse of a bridge damaged by the 2011 Tsunami in the Tohoku Region (Japan). St-Germain et al. (2014) used weakly compressible smoothed particle hydrodynamics (WCSPH) method to investigate the hydrodynamic forces induced by the impact of tsunami bores on a freestanding column of a square cross-section. Xu and Cai (2015) used a RANS solver tracking the free surface using the VOF method coupled with a spring-damper model to study lateral restraining stiffness effect on bridge deck-wave interaction. Chella et al. (2017) used a RANS solver with a free surface tracking algorithm called level-set method to investigate breaking solitary wave forces on a vertically mounted cylinder.

On the other hand, similar to the situation in the physical model experiments, a very limited number of studies focusing on tsunami-rubble mound coastal structure interactions were carried out. In addition to the experimental studies, Sakayima (2013) presented a numerical study with a RANS solver using VOF method for free-surface tracking. Guler et al. (2018a) conducted a numerical assessment study on a rubble mound breakwater using a Volume-Averaged RANS solver which uses the VOF method for free-surface capturing. This study is the second part of Chapter 3 of this thesis study.

2.2.2   Particle Motion Solvers

Discrete Element Method (DEM) is the most common approach to solve the motion and collision of the particles. DEM solvers are capable of simulating the motion of the solid particles, their collisions, and the final positions of these particles (Matuttis and Chen, 2014). The motion of the solid particles is evaluated based on Newton's equation of motion. The forces acting on each particle are considered in this solution. The solid particles are mostly modelled as spherical particles in DEM simulations, as the contact detection algorithms are straightforwards for this type of particles. On the other hand, there are algorithms for non-spherical particles such as polyhedral DEM method (Sarfaraz and Pak, 2018). The collision between the particles is

commonly modelled with a linear elastic spring and a viscous dashpot (Norouzi et al., 2016). The coefficients of elastic spring and viscous dashpot must be calibrated for better evaluation of the collisions.

An alternative given to DEM in the literature is the Adaptive Collision Time Model (ACTM) (Kempe and Fröhlich, 2012). Similar to DEM, the collision between the particles are modelled using an elastic spring and viscous dashpot. The difference of this methodology is that the coefficients of these spring-dashpot systems can be calculated with an iterative algorithm. It is reported that ACTM gives better results compared to DEM (Kempe and Fröhlich, 2012). However, the improvement in the results is in the order of millimetres; therefore, these errors could be accepted as negligible for coastal engineering applications.

2.2.3 Coupling CFD Solvers and Particle Motion Solvers

Numerical simulations using CFD solvers coupled with particle motion solvers, in particular DEM solvers, for engineering purposes gained popularity in the last two decades, as it is possible to evaluate the motion of the solid particles under flow conditions with these models. There are several applications in the context of coastal engineering using CFD solvers coupled with DEM solvers. Itoh et al. (2002) evaluated the performance of a submerged rubble mound breakwater. Arikawa et al. (2011) computed the motion of a solid object under wave attack. Latham et al. (2013) calculated forces on the armour layer of a rubble mound breakwater and evaluated breakage of the concrete units. Sun and Xiao (2016) studied the transport of sediment particles under flow conditions. Canelas et al. (2016) used an SPH solver coupled with a DEM solver to evaluate the motion of cubic objects under wave attack. More recently, Sarfaraz and Pak (2018) studied the motion of armour units in low-crested breakwaters using an SPH-DEM coupling methodology. Guler et al. (2018b) simulated the motion and collision of two spherical particles under solitary wave attack, presented in Chapter 4 of the present thesis study.

CHAPTER 3

EXPERIMENTAL AND NUMERICAL ASSESSMENT OF TSUNAMI ATTACK ON A RUBBLE MOUND BREAKWATER

In this chapter, the experimental and numerical assessment of tsunami attack on Haydarpaşa rubble mound breakwater, hereafter Haydarpaşa Breakwater, is presented. Haydarpaşa Breakwater is selected for this case study as it protects an important port in the Sea of Marmara that is in the tsunami-prone area (Guler et al., 2014; Aytöre, 2015).

3.1   Physical Model Experiments

The physical model experiments were conducted in the 105 m wave flume of Port and Airport Research Institute (PARI), Japan. In the experiments, although the potential tsunamis in the Sea of Marmara are taken into account, the breakwater was tested until its failure increasing the wave loading as it is aimed to observe the overall performance. The full dimensions of the wave flume are 105 m in length, 3.0 m in width and 2.5 m in depth; however, the tests were held in an inner channel with a width of 0.78 m. The scaling is carried out based on the Froude Law since the gravitational and inertial forces are dominant in these tests. A 1/30 length scale (λ_L) is selected. The time and the weight scales are calculated using Equation 3.1 which is based on the equality of the stability numbers (Hydralab, 2007).

$$\lambda_T = \sqrt{\lambda_L} \quad and \quad \lambda_W = \left(\lambda_L^3\right)\frac{(\gamma_s)_m}{(\gamma_s)_p}\left[\frac{(\gamma_s)_p/(\gamma_w)_p - 1}{(\gamma_s)_m/(\gamma_w)_m - 1}\right]^3 \qquad \text{Eq. 3.1}$$

In Equation 3.1, λ_T is the time scale, λ_W is the weight scale, $(\gamma_s)_m$ and $(\gamma_s)_p$ are the unit weight of the stones in the model and in the prototype that are taken as 2.65 t/m^3

and 2.7 t/m^3, respectively. Furthermore, $\left(\gamma_w\right)_m$ and $\left(\gamma_w\right)_p$ are the unit weight of the water in the model and in the prototype that are taken as 1.025 t/m^3 and 1.0 t/m^3, respectively. Using the given values, the time scale (λ_T) is calculated as 0.183 and the weight scale (λ_W) is calculated as 3.53x10^{-5}.

The water depth in front of the cross-section was set as 0.42 m. The water surface elevations along the wave channel were measured using eight wave gauges (WG1 to WG8) and the water particle velocities were measured using three Acoustic Doppler Velocimeters (ADV1 to ADV3). All the measurements were recorded with a sampling interval of 200 Hz. As expected, the measurements contain noise. This noise is eliminated using a standard procedure based on the Fast Fourier Transform (FFT). The measurements are transformed to the frequency domain using FFT to observe the variance spectrum of the data, and the data with low frequencies are deleted. Next, the data is converted into the time domain again using Inverse FFT. Thus, the mean behavior of the water particle velocities is obtained at each of ADV. The top and side views of the wave channel are presented in Figure 3.1, whereas a closer side view of the rubble mound breakwater cross-section is given in Figure 3.2. The locations of the measurement devices and the scaled stone dimensions are indicated on these figures.
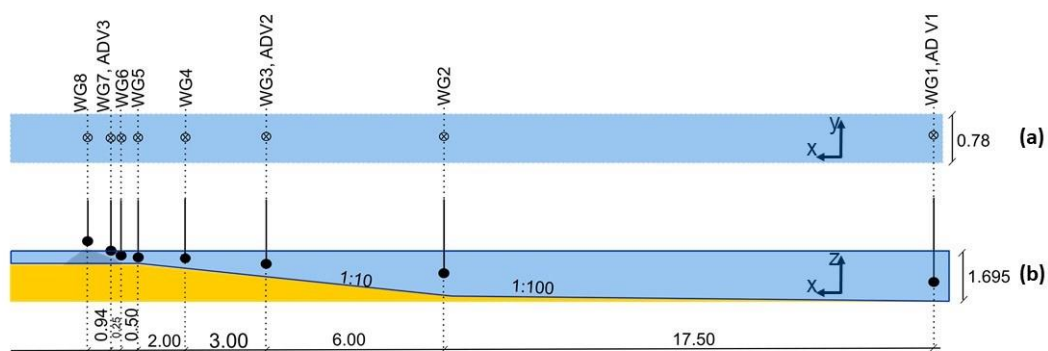
Figure 3.1. The Configuration of the Wave Channel and Locations of the Measurement Devices (Dimensions are given in meters.), (a) Top View (b) Side View
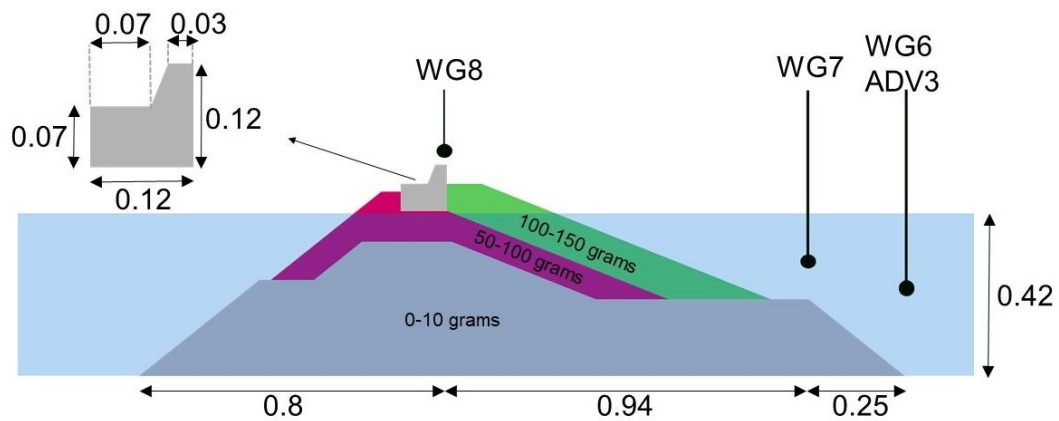
Figure 3.2. A Closer Side View of the Breakwater (Dimensions are given in meters.)

Madsen et al. (2008) showed that solitary waves cannot be represented by solitary waves only. Arikawa et al. (2012) discussed that the time elapsed during tsunami overflow affects the stability of the breakwaters. Therefore, in the present experiments, both solitary waves and tsunami overflow were used to represent tsunamis. The idea is to represent the first impact of the tsunamis using solitary wave experiments and the effect of time elapsed during the continuous flow over the breakwater using tsunami overflow. The solitary waves were generated using a piston-type wave generator whereas the tsunami overflow was produced by a pump system. The magnitude of the tsunami overflow is defined using its height. The tsunami overflow height (h) is defined as the distance between the crown-wall of the breakwater and the water surface elevation at that location measured by WG8. In general, the tsunami overflow height (h) is determined using the solitary wave experiments.

The damage along the cross-section was evaluated based on the profile measurements before and after the wave attack. Three profiles were taken along the cross-section to measure the amount of erosion. The damage parameter (S_d) proposed by Broderick (1984) given by Equation 3.2 was calculated to used for quantification of the damage.

21

$$S_d = \frac{A_e}{D_{n50}^2}$$
Eq. 3.2

In Equation 3.2, A_e is the eroded area in the profile and D_{n50} is the nominal diameter of the stones. The number of profiles may not be sufficient for quantitative evaluation. However, as the main aim is to observe the failure mode, the damage parameters are used for a qualitative assessment of the cross-section. Therefore, the damage parameter was calculated taking the eroded area as the maximum of the eroded areas along with the three profile measurements. The damage parameters were converted to qualitative results according to the damage levels given by CIRIA et al. (2007) where the damage is interpreted as "no damage or start of damage", "initiation of damage or intermediate damage" and "failure" when the damage parameter (S) is around 2, between 3 and 5, and bigger than 8, respectively.

The results of the experiments are presented as tables where the damage parameters (S) and corresponding qualitative results are given for both sea and harbour sides of the breakwater separately for the solitary wave cases and for just harbour side of the breakwater for the tsunami overflow experiments. The condition of the crown-wall was also indicated as "sliding", "small sliding" and "not sliding". "Small sliding" means that the sliding of the crown-wall is in the order of 1-2 cm horizontally; however, there is no failure of the cross-section due to the movement of the crown-wall. Furthermore, the tsunami overflow height measured in the solitary wave experiments, and the duration till the failure for the tsunami overflow experiments are also given in the related tables.

3.1.1   Solitary Wave Experiments

The solitary waves used in the experiments were determined according to previous tsunami generation, propagation and amplification studies conducted in the Sea of Marmara (Guler et al., 2014; Aytore, 2015). According to these studies, a tsunami height of 3 m can be expected near Haydarpaşa Breakwater. Therefore, the maximum solitary wave height is selected as 10 cm computed using the length scale of the

experiments. Three different solitary waves with H=5 cm, 7.5 cm, and 10 cm were considered in the tests. It is noted that these solitary wave heights were measured at the wave calibration stage when there is no cross-section in the channel at the wave gauges WG5, WG6 and WG7. When the cross-section is placed in the channel, the solitary wave heights increased due to the reflections from the cross-section. This issue is further discussed in the numerical modelling part (Section 3.2).

The results of the solitary wave experiments are presented in Table 3.1.

Table 3.1 Results of the Solitary Wave Experiments

H (cm)	Sea Side		Harbour Side		Sliding Condition	Overflow Height, h (cm)
	S_d	Damage Level	S_d	Damage Level		
5	-	No Damage	-	No Damage	No Sliding	-
7.5	3.27	Initiation of Damage	0.28	No Damage	No Sliding	1.7
10	8.33	Failure	9.30	Failure	Sliding	4.6

In Table 3.1, it is seen that there was no damage at the harbour side due to solitary wave attack when the solitary wave height was 7.5 cm, although the damage was initiated at the seaside. Several snapshots from the solitary wave experiment with H=10 cm are given in Figure 3.3 to extend the discussions.
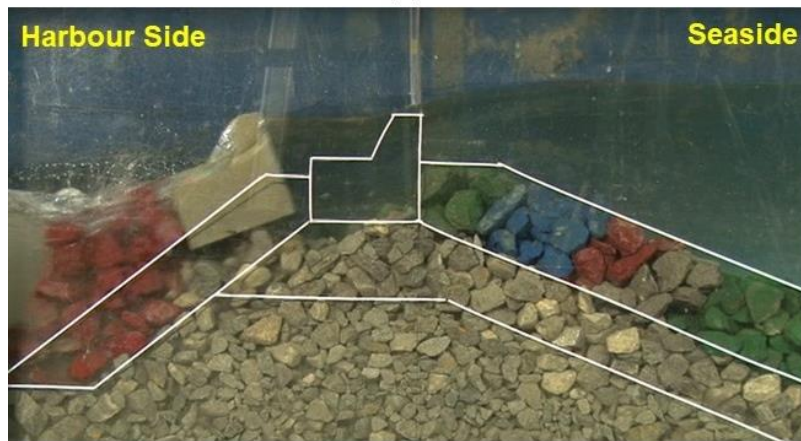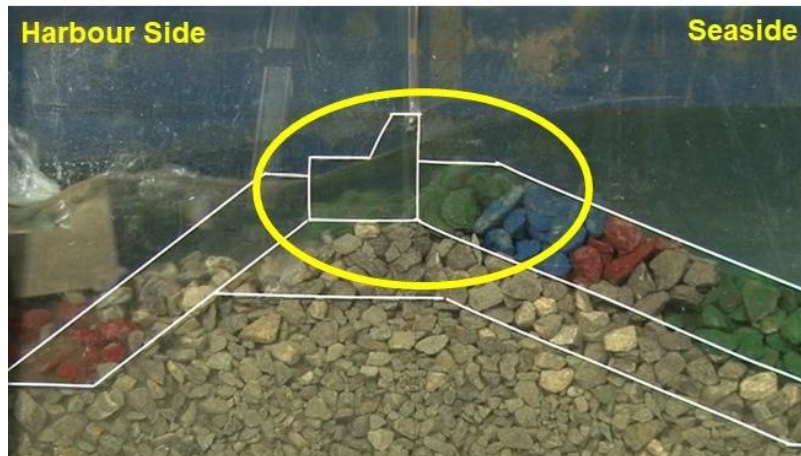
Figure 3.3. Solitary Wave Experiment (H=10 cm), (a) Overflow Height (b) Sliding of the Crown-Wall (c) Motion of the Stones at the Upper Layer of the Seaside Cross-Section

It is observed from Table 3.1 and Figure 3.3 that the cross-section was failed when the solitary wave height was 10 cm, and the failure was mainly due to the sliding of the crown-wall. It is further seen in Figure 3.3 that the upper layers of the armour stones at the seaside were dragged together with the crown-wall. However, the lower layers of the armour stones stayed almost in the same position. In the failure cases, there was no time for the scouring of the rubble stones at the harbour side; therefore, the sliding of the crown-wall is directly related to the pressure forces acting around the crown-wall.

3.1.2   Tsunami Overflow Experiments

The tsunami overflow experiments were firstly planned in a range tsunami overflow height range of 1.1-4.6 cm as 1.1 cm was the minimum height that could be generated by the available pumping system and 4.6 cm of overflow height corresponds to the maximum solitary wave height. However, the original cross-section of Haydarpaşa Breakwater was failed much earlier around a tsunami overflow height of 1.9 cm. Therefore, a counter-measure cross-section was proposed doubling the armour layer at the harbour side of the breakwater. Thus, it is aimed to increase supporting force. Details of the experiments are given below:

3.1.2.1   Original Cross-Section of Haydarpaşa Breakwater

The tsunami overflow heights in the tsunami overflow experiments on the original cross-section were ranging between h=1.1 cm and h=1.95 cm. The results of the experiments are presented in Table 3.2.

Table 3.2 Results of the Tsunami Overflow Experiments on the Original Cross-Section

#	h (cm)	S_d	Damage Level	Sliding Condition	Failure Time*
1	1.1	-	No Damage	No Sliding	-
2	1.15	-	No Damage	No Sliding	-
3	1.2	-	No Damage	No Sliding	-
4	1.3	-	No Damage	No Sliding	-
5	1.4	1.36	No Damage	Small Sliding	-
6	1.7	8.37	Failure	Sliding	2 mins
7	1.85	1.73	No Damage	Small Sliding	-
8	1.9	10.24	Failure	Sliding	6.5 mins
9	1.95	10.63	Failure	Sliding	2 mins 10 secs
Failure time is given in terms of recording time.					

It is seen from Table 3.2, there is certainly no damage in the cross-section until h=1.4 cm. After that, there is region where both failure and no damage with small sliding cases are observed. This indicates that the arrangement of the stones at the harbour side can change the experimental condition and increase the uncertainty in between h=1.7 cm and h=1.9 cm. Starting with h=1.9 cm, failure cases were observed. Furthermore, the failure times indicate that the placement of the stones significantly affected the results. Overall, it is seen that the failure of the cross-section is due to the sliding of the crown-wall, and the scouring of the stones at the harbour side is also significant in addition to the pressure forces acting on the crown-wall. That's the simple explanation why the cross-section was failed due to a much lower tsunami overflow height corresponding to the solitary wave height of 7.5 cm compared to the overflow height of 4.6 cm corresponding to the solitary wave with a wave height of 10 cm. A snapshot from the tsunami overflow experiment with a tsunami overflow height of h=1.9 cm is presented in Figure 3.4.

Figure 3.4. Sliding of the Crown-Wall in the Tsunami Overflow Experiment on the Original Cross-Section (h=1.9 cm)

In Figure 3.4, the motion of the crown-wall is observed due to tsunami overflow.

3.1.2.2   Counter-Measure Cross-Section for Haydarpaşa Breakwater

The counter-measure cross-section was proposed as the doubling of the armour layer width at the seaside. The tsunami overflow heights in the tsunami overflow experiments on the counter-measure cross-section were ranging between h=1.5 cm and h=4.6 cm. A snapshot from the experiment with h=4.6 cm is given in Figure 3.5.
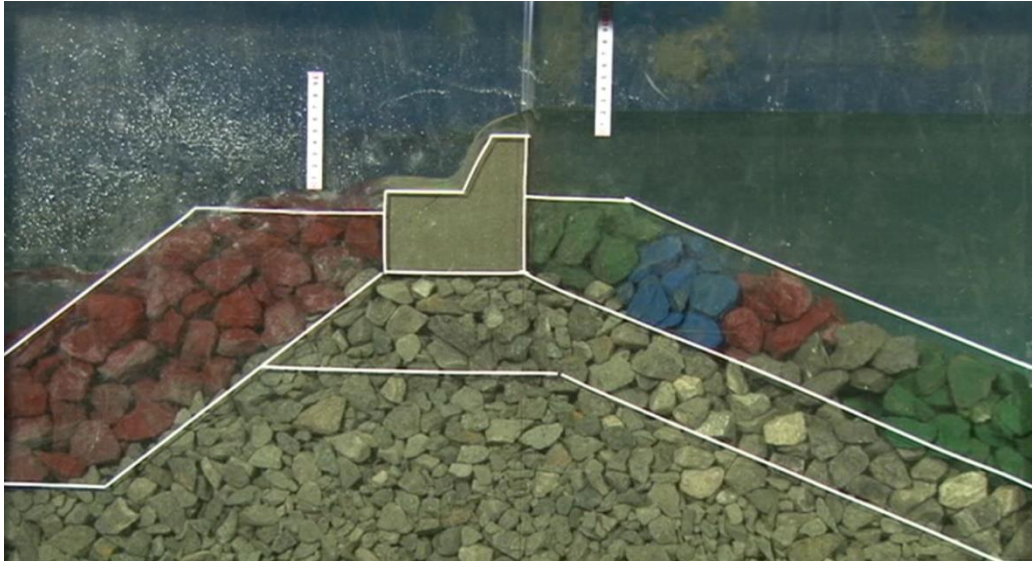
Figure 3.5. Sliding of the Crown-Wall in the Tsunami Overflow Experiment on the Counter-Measure Cross-Section (h=4.6 cm)

Table 3.3 Results of the Tsunami Overflow Experiments on the Counter-Measure Cross-Section

#	h (cm)	S_d	Damage Level	Sliding Condition	Failure Time*
1	1.5	-	No Damage	No Sliding	-
2	1.6	-	No Damage	No Sliding	-
3	2.1	6.23	Intermediate Damage	No Sliding	-
4	2.7	4.66	Intermediate Damage	No Sliding	-
5	2.8	6.42	Intermediate Damage	No Sliding	-
6	3.4	5.98	Intermediate Damage	Small Sliding	-
7	3.65	5.10	Intermediate Damage	Small Sliding	-
8	4.3	6.07	Intermediate Damage	Small Sliding	-
9	4.4	9.31	Failure	Sliding	2 mins 50 secs
10	4.6	18.88	Failure	Sliding	3 mins 53 secs
Failure time is given in terms of recording time.					

It is seen from Table 3.3 that the cross-section was failed when the tsunami overflow height was equal and bigger than 4.4 cm which is in the same order with the target h=4.6 cm. Therefore, it can be said that the counter-measure cross-section significantly improved the stability of the breakwater under tsunami overflow comparing to the original cross-section of Haydarpaşa Breakwater. In Figure 3.5, the action of overflow is seen.

3.2   Numerical Modelling Studies

The numerical modelling study is carried out using a widely used computational fluid dynamics (CFD) solver called IHFOAM developed based on the CFD library OpenFOAM. IHFOAM is firstly released as wave generating and absorbing boundary conditions (Higuera et al., 2013), and it is linked to an OpenFOAM solver called interFoam. interFoam solves Reynolds-Averaged Navier-Stokes (RANS) equations with a two-phase approach and captures free-surface using the Volume of Fluid (VOF) method. Later, Higuera et al. (2014a, 2014b) modified interFoam solver of the OpenFOAM to account for flow inside the porous media; this numerical solver, including the boundary conditions, is also called IHFOAM. IHFOAM solves Volume-Averaged RANS (VARANS) equations in order to compute flow properties inside the porous medium. Outside the porous medium, VARANS equations reduce to RANS equations. As the present problem is to simulate the physical model experiments conducted on Haydarpaşa Breakwater, which is a rubble mound breakwater, these numerical tools are appropriate for such a study. As discussed in Chapter 2, this type of modelling is called macroscopic porous media modelling. As the geometry inside the layers of Haydarpaşa Breakwater cannot be known exactly, the macroscopic approach is the most relevant methodology for this case.

In Section 3.2, firstly, the numerical model is described. It is noted that details of OpenFOAM environment and implementation of solvers in this environment are addressed in Chapter 5 in relation to the development of the new CFD solvers. Furthermore, the calibration and the validation studies are presented based on the

physical model experiments on Haydarpaşa Breakwater. After that, the numerical model is used to predict the effect of a potential tsunami on Haydarpaşa Breakwater, showing the combined effect of the solitary wave and tsunami overflow experiments. Finally, the outcomes of the simulations are interpreted in terms of engineering applications presenting the pressure distribution around the crown-wall of Haydarpaşa Breakwater and estimating the forces on the single rubble stone located at the top layer at the harbour side of the breakwater. All the numerical simulations are carried out on the original cross-section of Haydarpaşa Breakwater.

3.2.1   Description of the Numerical Model

IHFOAM used in this part of the present study is compiled with OpenFOAM version 2.1.1 distributed by OpenFOAM Foundation (OpenFOAM, 2012). VARANS equations solved in IHFOAM are the continuity equation given by Equation 3.3 and the momentum equation given by 3.4.

$$\frac{\partial \langle u_i \rangle}{\partial x_i} = 0 \qquad\qquad \text{Eq. 3.3}$$

$$\frac{(1+C)}{n} \frac{\partial \rho \langle u_i \rangle}{\partial t} + \frac{1}{n} \frac{\partial}{\partial x_j} \left(\frac{\rho \langle u_i \rangle \langle u_j \rangle}{n} \right) =$$

$$-\frac{\partial \langle p \rangle^f}{\partial x_i} + \rho g_i + \frac{1}{n} \frac{\partial}{\partial x_j} \left(\mu_{eff} \frac{\partial \langle u_i \rangle}{\partial x_j} \right) - A \frac{\langle u_i \rangle}{n} - B \langle u_i \rangle \frac{\sqrt{\langle u_j \rangle \langle u_j \rangle}}{n} \qquad \text{Eq. 3.4}$$

In Equations 3.3 and 3.4, $\langle u_i \rangle$ is the volume-averaged velocity of the ith coordinate (x_i); n is the porosity defined as the volume of the voids over the total volume; $\langle p \rangle^f$ is the intrinsic pressure; ρ is the density; g is the acceleration of gravity; μ_{eff} is the efficient dynamic viscosity defined as $\mu_{eff} = \mu + \rho \upsilon_{turb}$ where μ is the dynamic molecular viscosity and υ_{turb} is the turbulent kinetic viscosity computed by the selected turbulence model. As the model considers two incompressible phases (gas

and liquid), the density and the molecular viscosity values are updated in the presence of gas and liquid interface that is discussed further below in relation with the free-surface modelling. *A*, *B* and *C* are the closure parameters related to the physics that cannot be solved when volume-averaging. In other words, these parameters are related to macroscopic porous media modelling approach. For the details of the volume-averaging procedure, the reader is referred to Jensen et al. (2014) and Higuera (2015).

There are various closure models in the literature to define *A* and *B*. In IHFOAM, the formulation developed by Engelund (1953) is employed in a form given in Burcharth and Andersen (1995). The definitions of the parameters A and B are given by Equations 3.5 and 3.6, respectively.

$$A = a\frac{(1-n)^3}{n^2}\frac{\mu}{D_{n50}^2}$$

Eq. 3.5

$$B = b\left(1+\frac{7.5}{KC}\right)\frac{1-n}{n^2}\frac{\rho}{D_{n50}}$$

Eq. 3.6

In Equations 3.5 and 3.6, *a* and *b* are the linear and non-linear friction parameters, respectively; D_{n50} is the nominal mean diameter of the porous material; *KC* is the Keulegean-Carpenter number that introduces additional friction due to the oscillatory nature and unsteadiness of the system defined by Equation 3.7.

$$KC = \frac{T_0 u_M}{D_{n50} n}$$

Eq. 3.7

In Equation 3.7, T_0 is the period of the oscillation and u_M is the maximum oscillatory velocity.

In order to solve VARANS equations accurately, one must calibrate the parameters *a*, *b* and *C*. Jensen et al. (2014) were the first to present a comprehensive calibration taking into account a wide range of flow regimes. Later, an extensive literature review on the porous media modelling approaches, closure parameters and these

parameters are presented by Losada et al. (2016). On the other hand, it is recommended to take added mass coefficient (*C*) as 0.34 by del Jesus et al. (2012) that does not have vital importance in most of the cases.

OpenFOAM is developed using the finite volume discretization on collocated grids. In IHFOAM, Pressure Implicit with Splitting Operator (PISO) algorithm presented by Issa (1986) is used to solve VARANS equations. The reader is referred to Moukalled et al. (2012) for the details of the implementation of the PISO algorithm in OpenFOAM library, and Deshpande et al. (2012) for the specific details of the implementation in interFoam solver which is the basis of IHFOAM. In OpenFOAM CFD library, the turbulence modelling is generic. It is straightforward to use various two-equation models.

The volume of fluid (VOF) method is used to capture free-surface in IHFOAM. In the VOF method, there is an indicator function (α) defined at each cell in the computational domain, takes a value of 1 when the cell is full of liquid; on the other hand, it takes a value of 0 when the cell is full of gas. The details of this method will be discussed in Section 5.2.3. A volume-averaged version of VOF-advection equation given by Equation 3.8 is solved in IHFOAM.

$$\frac{\partial \alpha}{\partial t} + \frac{1}{n}\frac{\partial \alpha \langle u_i \rangle}{\partial x_i} + \frac{1}{n}\frac{\partial \alpha (1-\alpha)\langle u_i^r \rangle}{\partial x_i} = 0 \qquad\qquad \text{Eq. 3.8}$$

In Equation 3.8, is the volume-averaged compression velocity defined as $u_i^r = u_i^l - u_i^g$ where u_i^l is the velocity of the liquid phase and u_i^g is the velocity of the gas phase. In IHFOAM, Equation 3.8 is solved in the same way with interFoam solver of OpenFOAM using a scheme called Multidimensional Universal Limiter with Explicit Solution (MULES). MULES limits the value of the indicator function between 1 and 0.

According to the variation of VOF indicator function, density and the molecular viscosity are updated at each cell in the computational domain with the equations

given in Equations 3.9 and 3.10. Thus, the effect of two incompressible phases is taken into account.

$$\rho = \alpha \, \rho_l + \left(1 - \alpha\right) \rho_g \qquad \qquad \text{Eq. 3.9}$$

$$\mu = \alpha \, \mu_l + \left(1 - \alpha\right) \mu_g \qquad \qquad \text{Eq. 3.10}$$

In Equations 3.9 and 3.10, the sub-indices l and g stand for the liquid and gas phases.

IHFOAM solver, linked with the appropriate boundary conditions given by Higuera et al. (2013), is capable of generating and absorbing waves. These boundary conditions include generation of waves Stokes I, II and V order, cnoidal, streamfunction, solitary and irregular waves in addition to piston-type wavemaker. In the present study, the piston-type wavemaker is used; therefore, the description below is limited to the piston-type wavemaker. There are several options for the piston-type wavemaker in this boundary condition. Either the displacement or velocity time series of the wavemaker is inputted to generate waves. In the present study, the velocity time series is inputted that will be described in the section related to the numerical settings. The boundary conditions are capable of active wave absorption for 2D, Quasi-3D and 3D conditions. The idea of the active wave absorption is to generate target wave modifying the initial input based on the feedback preventing the re-reflections. Active wave absorption can also be used for purely absorbing boundaries, i.e., outlets. In the present study, 2D active wave absorption algorithm is used at wave generating boundaries at the inlet and outlet. This algorithm is implemented by Higuera et al. (2013) as it appears in Schaffer and Klopman (2000) that is based on the shallow water theory. As the velocity along the water column height is constant in front of a piston-type wavemaker, the velocity profile can be given by Equation 3.11.

$$U = \frac{c\eta}{h} \qquad \qquad \text{Eq. 3.11}$$

In Equation 3.11, U is the uniform horizontal velocity, c is the wave celerity, h_{water} is the water depth and η water surface elevation. h_{water} and η is taken from the measurements, and the wave celerity is given by Equation 3.12.

$$c = \sqrt{gh_{water}}\sqrt{\frac{tanh\left(kh_{water}\right)}{kh_{water}}}$$

Eq. 3.12

In Equation 3.12, k is the wave number, and g is the acceleration of gravity. The wave generating boundary must generate a velocity equal to the incoming one but in the opposite direction to eliminate the effect of the reflected waves. Therefore, a correction velocity (U_c) is applied to the wave tank given by Equation 3.13.

$$U_c = -\sqrt{\frac{g}{h}}\eta_r$$

Eq. 3.13

where η_r is the reflected water surface elevation computed by subtracting the target water surface elevation from the measured water surface elevation in front of the wavemaker.

3.2.2   Settings of the Numerical Model

The numerical simulations are carried out in a two-dimensional numerical tank as the experiments could be accepted as two-dimensional. As stated above, the experiments were conducted in 105 m wave channel of PARI. However, a much shorter computational domain is considered in the numerical simulations to save computational time. The length (horizontal direction) and height (vertical direction) of the computational domain are selected as 33.3 m and 1.95 m, respectively. The bottom slope and the crown wall are removed from the computational domain to achieve a body-fitted mesh configuration. The number of cells along the transverse direction is kept as one. Side view of the computational domain is given in Figure 3.6.
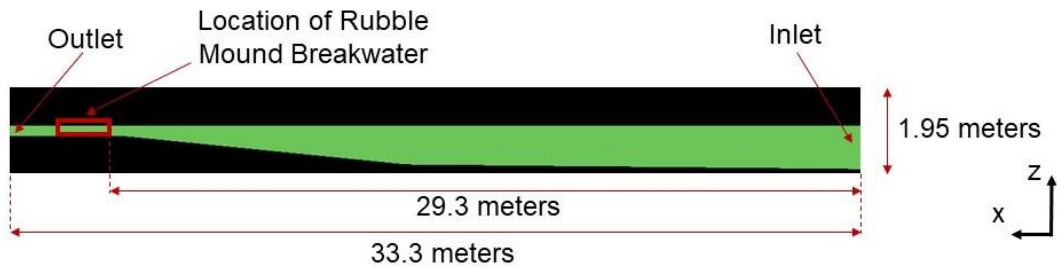
Figure 3.6. Side view of the computational domain

A regular mesh size of 1 cm and 0.5 cm are chosen along x and z directions, respectively. The mesh size around the crown-wall is refined, resulting in mesh size of 0.5 cm and 0.25 cm along x and z directions, respectively. The total number of cells is approximately one million with this configuration. The grid independence tests are conducted based Grid Convergence Index (GCI) described in Chapter 2. The maximum GCI is calculated as 1.8% comparing the abovementioned mesh sizes with half of them. The resulting GCI shows grid-independent solution.

As a particular portion of the wave channel considered in this numerical simulation, the measured water surface elevation at WG1 and water particle velocity at ADV1 are used when generating waves at the inlet for the solitary wave experiments. On the other hand, these data cannot be inputted for the tsunami overflow experiments, as excessive simulation time might be needed to reach the expected tsunami overflow height. Instead of these data, the water surface elevations and the particle velocities are increased faster than the physical model experiments at the beginning; and the simulation is stopped where the constant overflow is obtained. Finally, a long sinusoidal wave is used to simulate the effect of the potential tsunami on the breakwater. Details of this case are given in Section 3.2.6. At the outlet, the wave absorbing boundary condition is used for all the cases. The top boundary of the simulations is set as "atmosphere" whereas the bottom boundary is set as a "wall". The boundary conditions along the transverse direction are determined as "empty". When the solvers based on OpenFOAM are used, the "empty" boundary condition is used to transform the simulations into two dimensions.

In this numerical modelling study, the standard k-ω SST turbulence model is used in all simulations which is firstly introduced by Menter (1994). This is a well-known turbulence model combining k-ε model with k-ω model as k-ε model performs better in the free flow region whereas k-ω model gives better results near solid boundaries.

The simulation duration also differs. The simulation durations are selected as 30, 30, and 50 seconds for the solitary wave experiments, the tsunami overflow experiments, and the potential tsunami case, respectively.

3.2.3 Model Calibration (Solitary Wave Case, H=7.5 cm)

The calibration of IHFOAM is carried out based on the data from the solitary wave experiments with H=7.5 cm. As stated in the physical model experiments part, this case resulted in minor damage, and the crown-wall was not slid. The calibrated porous media coefficients are presented in Table 3.4 for each layer of the rubble mound breakwater in addition to the diameters of the stones in these layers and porosities of these layers. The added mass coefficient (*C*) is taken as 0.34 as recommended by del Jesus et al. (2012).

Table 3.4 Parameters used in the Numerical Simulations

Layers	Diameter of Stones (D_{n50}) in meters	Porosity (*n*)	Porous Media Coefficients		
			a	*b*	*C*
Armour	0.040	0.40	50	0.6	0.34
Filter	0.033	0.35	50	2.0	0.34
Core	0.015	0.30	50	1.2	0.34

The solitary wave overflows the crown-wall of the rubble mound breakwater between t=13.8 sec and t=15.2 sec as seen in the numerical simulation. In Figure 3.7, snapshots from the simulation showing the velocity field in the wave channel are given.
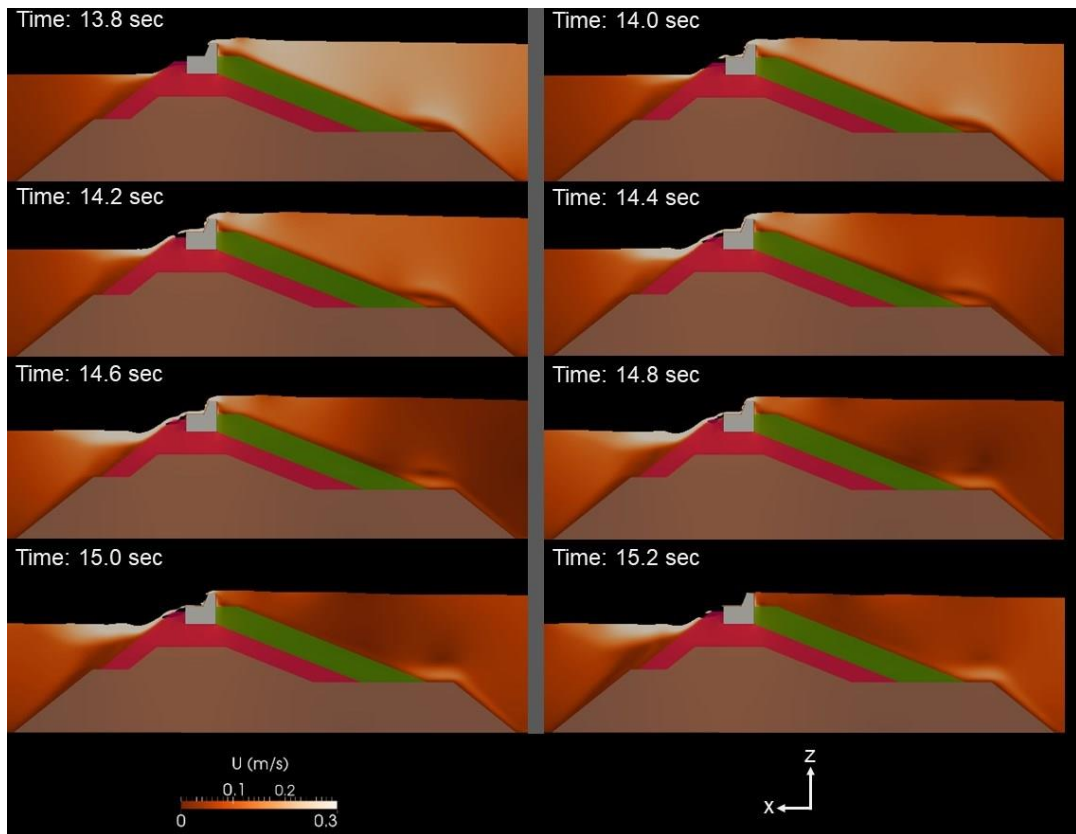
Figure 3.7. Snapshots from the numerical simulation (Solitary wave case, H=7.5 cm)

In Figure 3.7, it is seen that the maximum velocity is around 0.3 m/s at the front of the wave. The magnitudes of the velocities at the harbour side of the breakwater are higher than the sea side of the breakwater that is parallel to the observations in the physical model experiments as lower damage is observed at the sea side. In Figure 3.8 and Figure 3.9, the water surface elevations along the wave channel computed in the numerical simulation are compared to the experimental measurements.
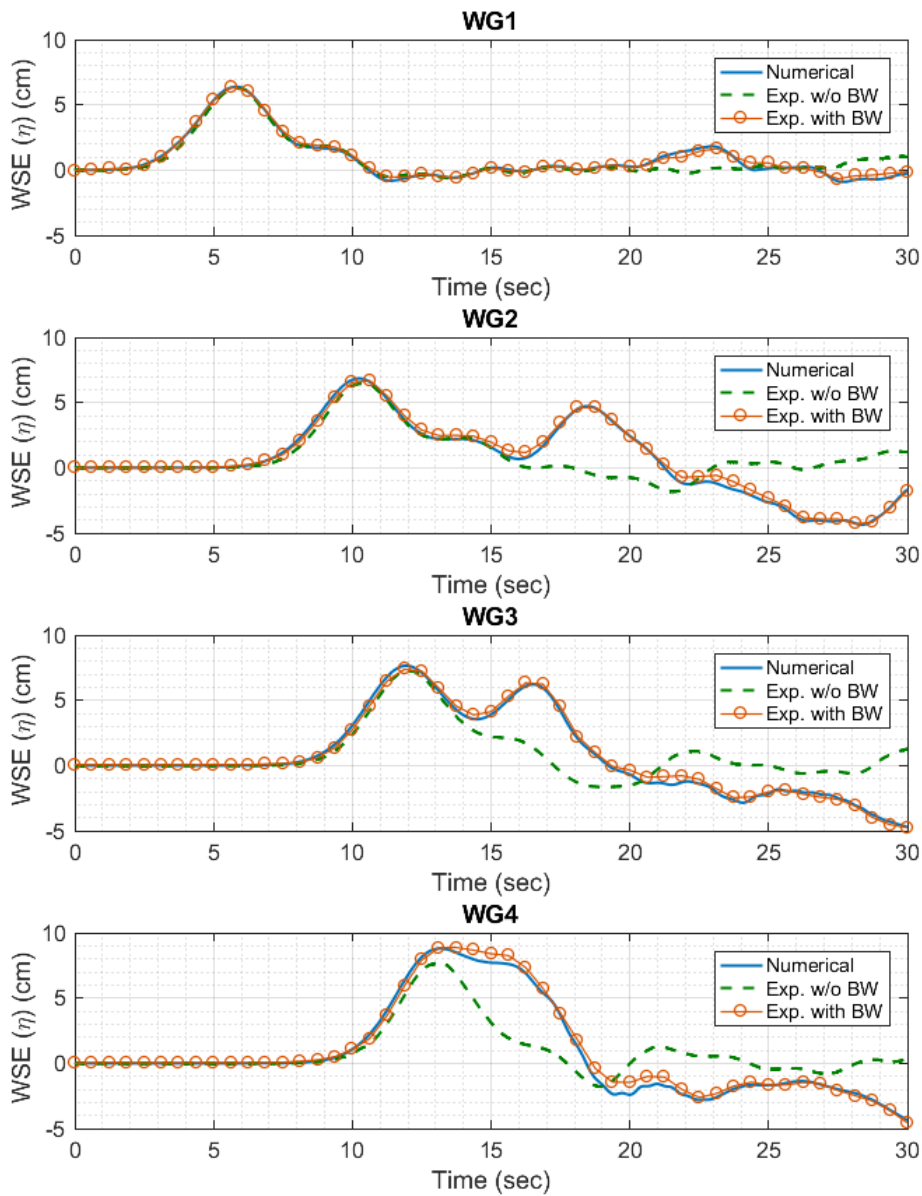
Figure 3.8. Comparison of water surface elevations at WG1-WG4: Numerical results (blue solid line), Experimental measurements with breakwater (solid orange line and orange circles), Experimental measurements without breakwater (dashed green line)
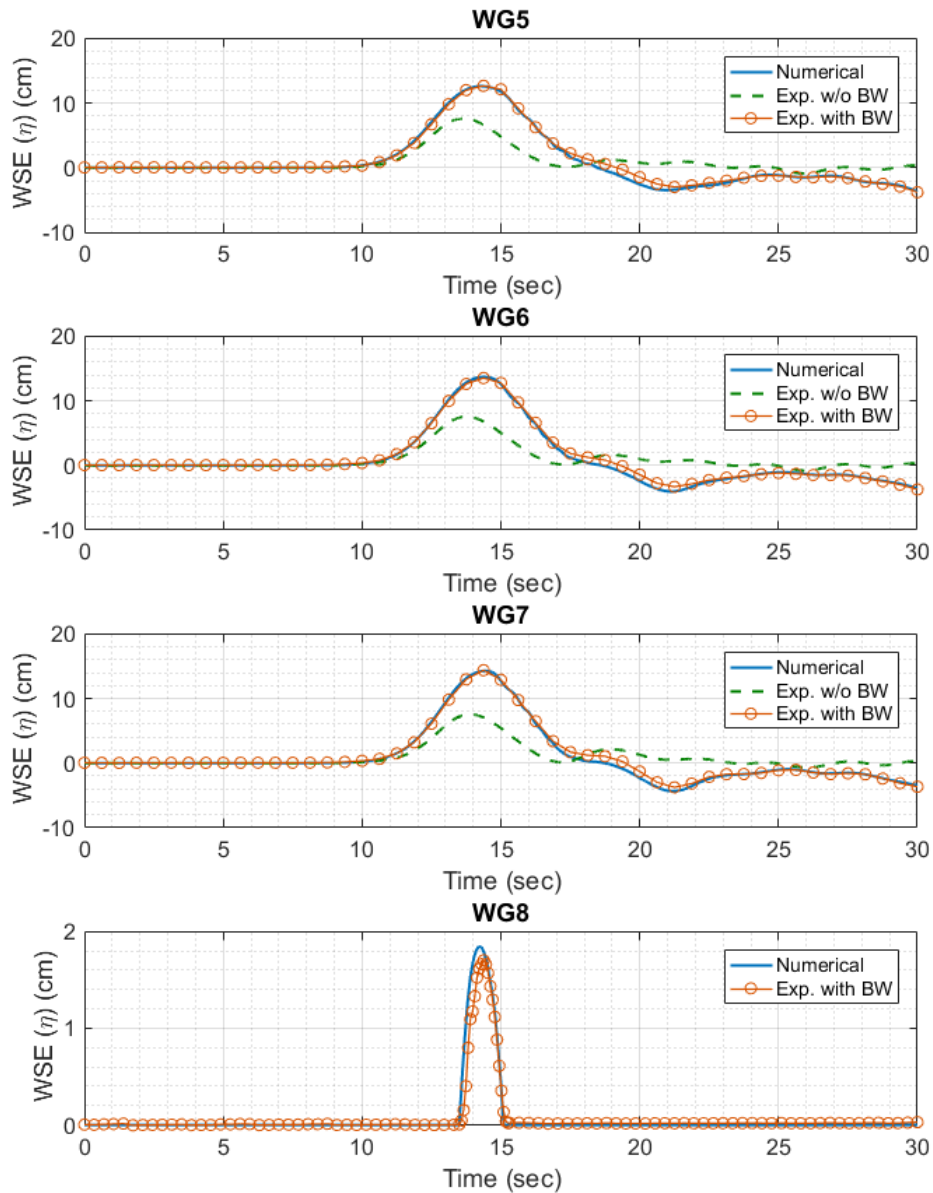
Figure 3.9. Comparison of water surface elevations at WG5-WG8: Numerical results (blue solid line), Experimental measurements with breakwater (solid orange line and orange circles), Experimental measurements without breakwater (dashed green line)

It is noted in the physical model experiments part (Section 3.1) that the solitary wave heights are given as the values where there is no cross-section in the wave channel. However, the solitary wave heights are increasing as these waves are very long. Therefore, the water surface elevation data from the experiments are plotted Figure 3.8 for with breakwater and without breakwater cases. The water surface elevation

at WG8 for without breakwater case is not plotted as it is focused on the tsunami overflow at this wave gauge. It is seen in Figure 3.8 for WG1-WG4 and in Figure 3.9 for WG5-WG8 that the numerical and experimental results with the breakwater are in a good agreement. In Figure 3.10, the numerical results of particle velocity along horizontal direction are compared to the ADV measurements from the physical model experiments with breakwater.
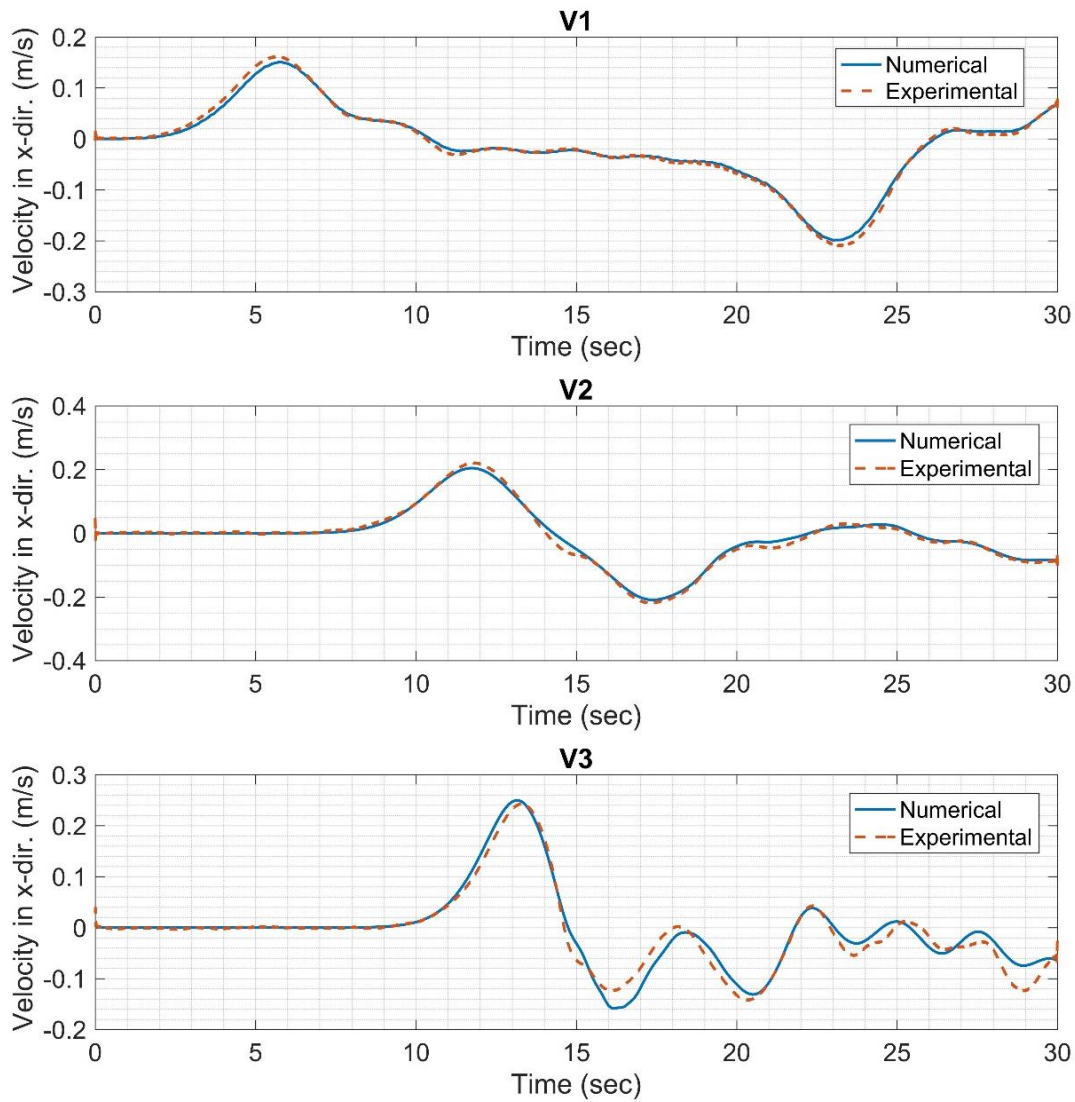
Figure 3.10. Comparison of water particle velocities in the horizontal (in x-) direction: Numerical results (solid blue line), Experimental results (solid orange line)

It is seen from Figure 3.10 that the particle velocities are computed with reasonable accuracy. Although the general trend and magnitudes are computed in a good agreement with the physical model experiments in general, there are some differences at V3 (ADV3) in the numerical results. As the location of V3 is above the toe of the breakwater, these differences originated most probably due to the volume averaging assumption.

Thus, the calibration of the numerical model is completed based on the experimental data from solitary wave experiments with H=7.5 cm.

3.2.4   Model Validation Study I (Solitary Wave Case, H=10 cm)

The validation of IHFOAM is carried out based on the experimental data of the solitary wave experiments with H=10 cm. As stated in the physical model experiments part, this case resulted in the failure of the cross-section, and the crown-wall was slid. The calibrated model parameters given in Table 3.4 are used in the simulation.

The water surface elevations calculated using the numerical model are compared to the data from the physical model experiments in Figure 3.11 for WG1-WG4 and in Figure 3.12 for WG5-WG8.
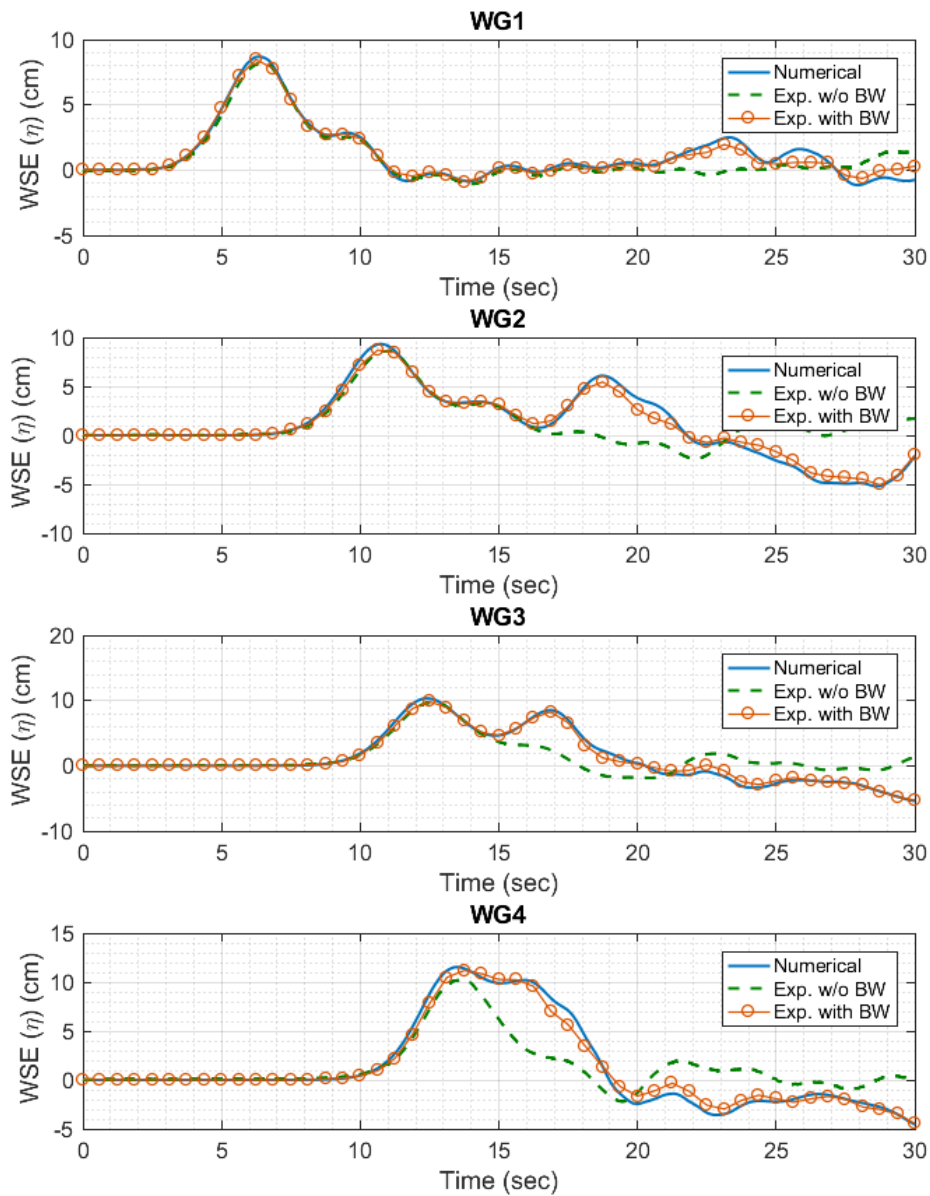
Figure 3.11. Comparison of water surface elevations for WG1-WG4: Numerical results (blue solid line), Experimental measurements with breakwater (solid orange line and orange circles), Experimental measurements without breakwater (dashed green line)
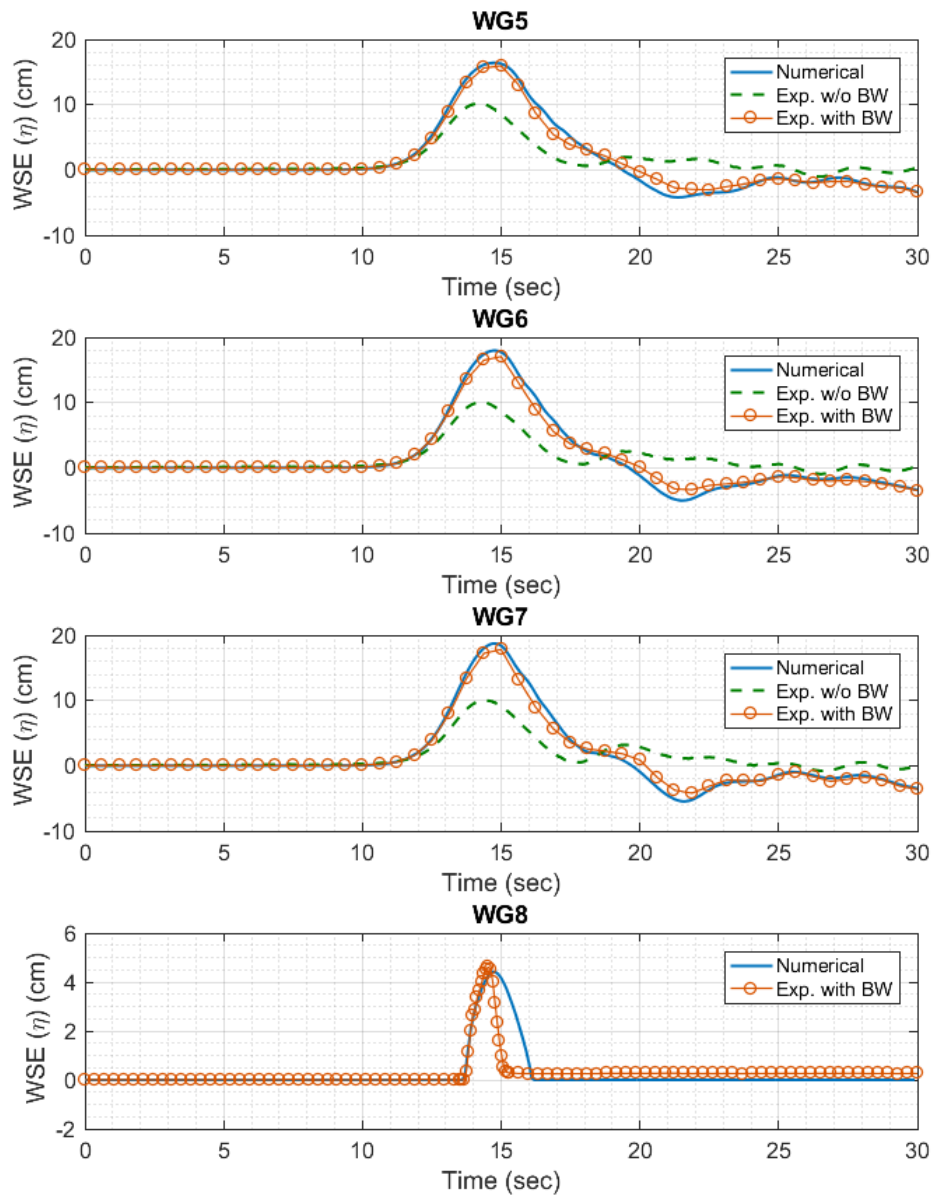
Figure 3.12. Comparison of water surface elevations for WG5-WG8: Numerical results (blue solid line), Experimental measurements with breakwater (solid orange line and orange circles), Experimental measurements without breakwater (dashed green line)

It is seen from Figure 3.11 and Figure 3.12 that the numerical results and the measurements from the experiments with breakwater are in a good agreement at all the wave gauges except for WG8. As the crown-wall was slid, the water surface elevation decreases faster than the numerical simulation at this wave gauge. In Figure

3.13, the numerical results of particle velocity along horizontal direction are compared to the ADV measurements from the physical model experiments with breakwater.
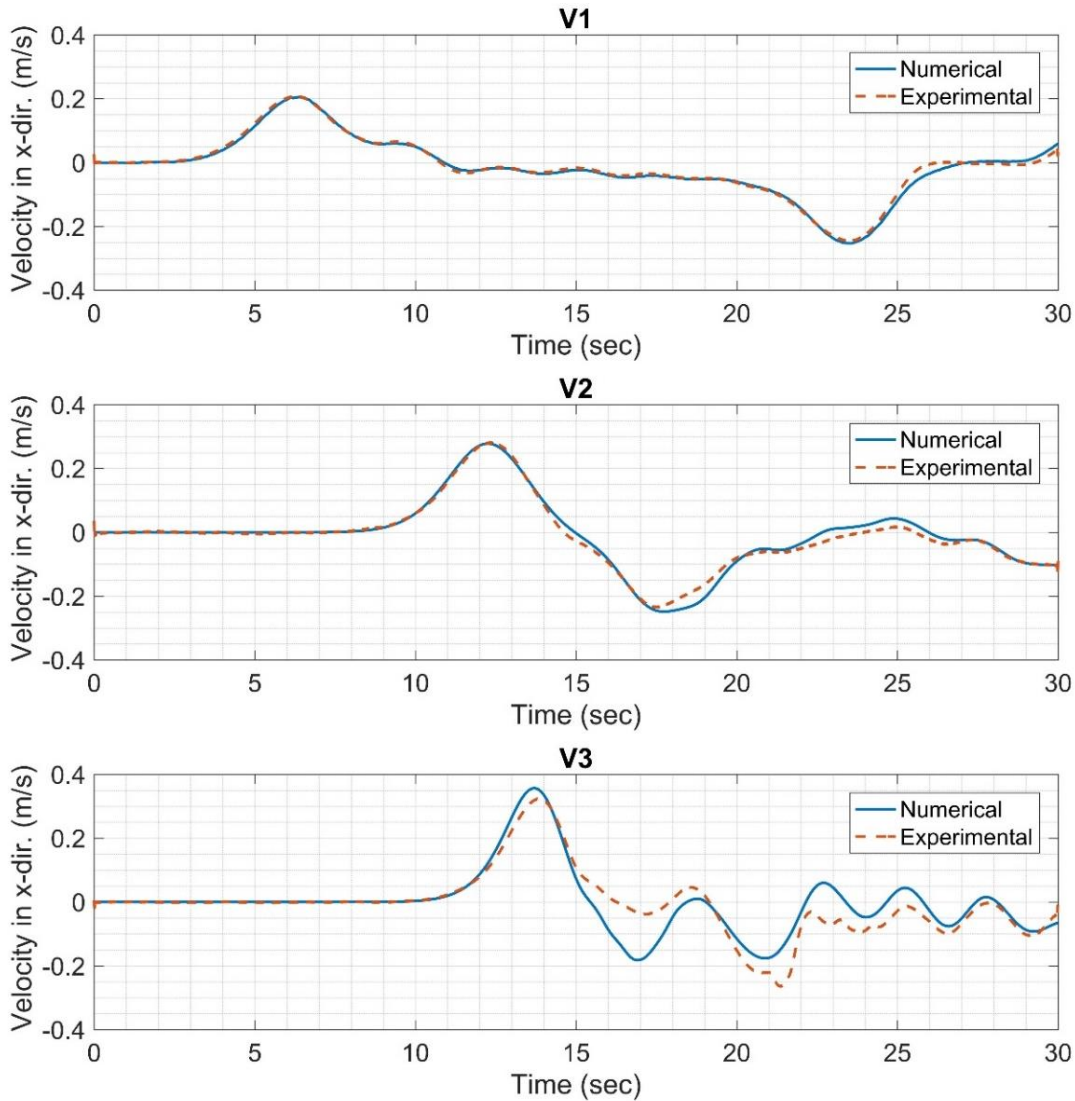
Figure 3.13. Comparison of water particle velocities in the horizontal (in x-) direction: Numerical results (solid blue line), Experimental results (dashed orange line)

It is seen from Figure 3.13 that the particle velocities are computed with reasonable accuracy; however, there is a significant deviation in the numerical results from the

experimental data at V3 (ADV3). This deviation is due to the sliding of the crown-wall around t=14.5 sec.

Thus, the validation of the numerical model is completed based on the experimental data from the solitary wave experiments with H=10 cm since an accurate numerical simulation can be conducted using the previously calibrated model parameters given in Table 3.4.

3.2.5   Model Validation Study II (Tsunami Overflow Case, h=1.9 cm)

In the physical model experiments, h=1.9 cm corresponds to the H=7.5 cm solitary wave case. Although the solitary wave experiment with H=7.5 cm resulted in no damage, the tsunami overflow case with h=1.9 cm resulted in the failure of the cross-section indicating the importance of the time elapsed during the tsunami overflow. This case is also studied numerically to validate IHFOAM for the tsunami overflow cases, and to discuss the difference in between these different type of experiments.

The generation of tsunami overflow is discussed in Section 3.2.3. In summary, the water level is increased faster than the physical model experiments to reach steady tsunami overflow in a rather short duration in the numerical simulation. Once the steady tsunami overflow is reached, it is trivial to compare all the wave gauges and the ADVs. Therefore, the numerical and experimental comparisons are presented only for WG7, WG8 and ADV3 in Figure 3.14.
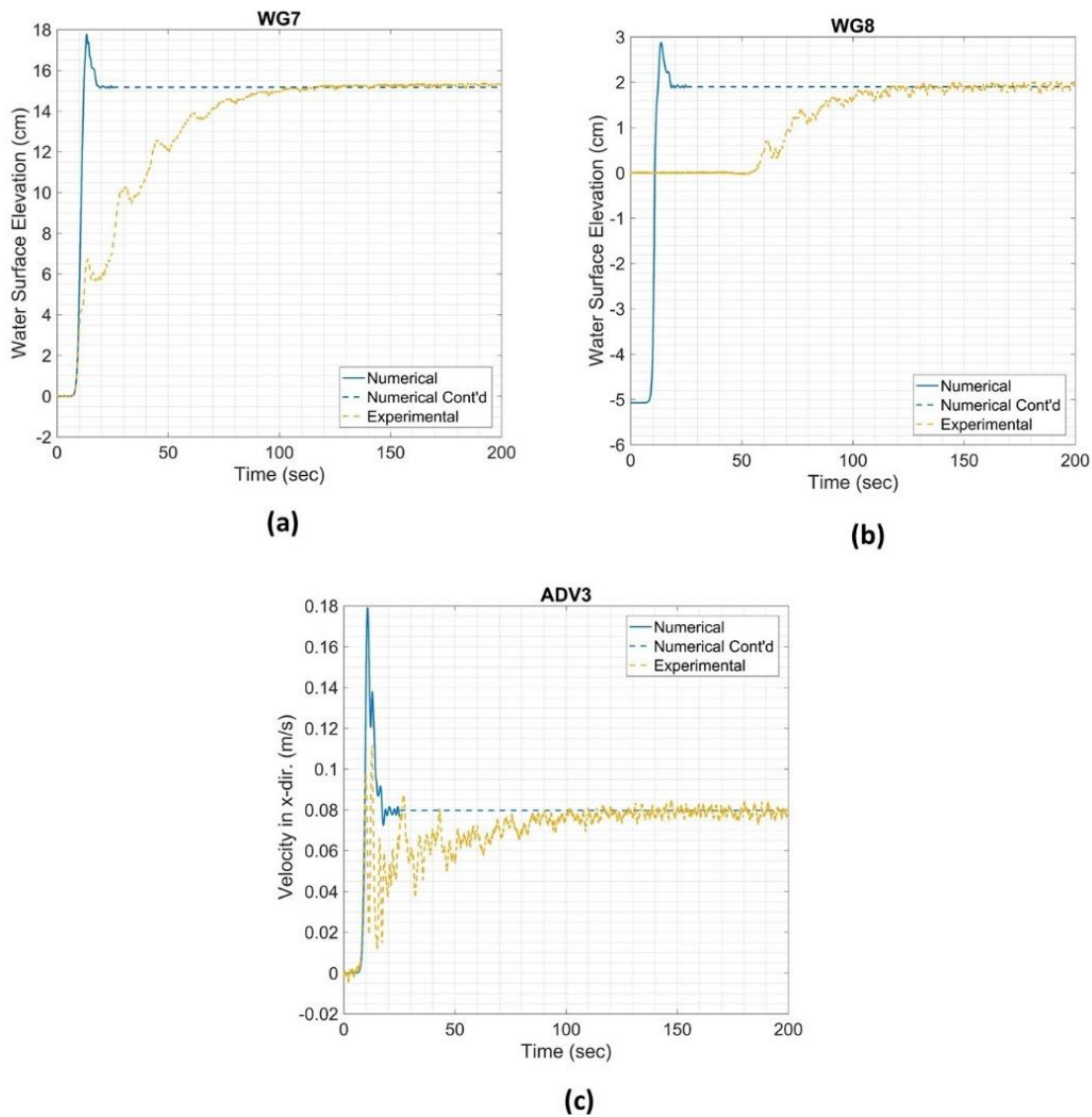
Figure 3.14. Comparison of the numerical (solid blue line, continuation line is dashed blue) and experimental data (dashed orange line): (a) Water surface elevation at WG7, (b) Water surface elevation at WG8, (c) Particle velocities in horizontal (in x) direction

In Figure 3.14, there is a significant time-lag between the numerical and experimental results. This lag is due to the methodology used to generate tsunami overflow. However, continuation lines plotted in Figure 3.14 showed that the water surface elevations at WG7 and WG8, and the particle velocities at ADV3 can be

simulated using the numerical model when the steady tsunami overflow is reached. A snapshot from the tsunami overflow simulation is presented in Figure 3.15.
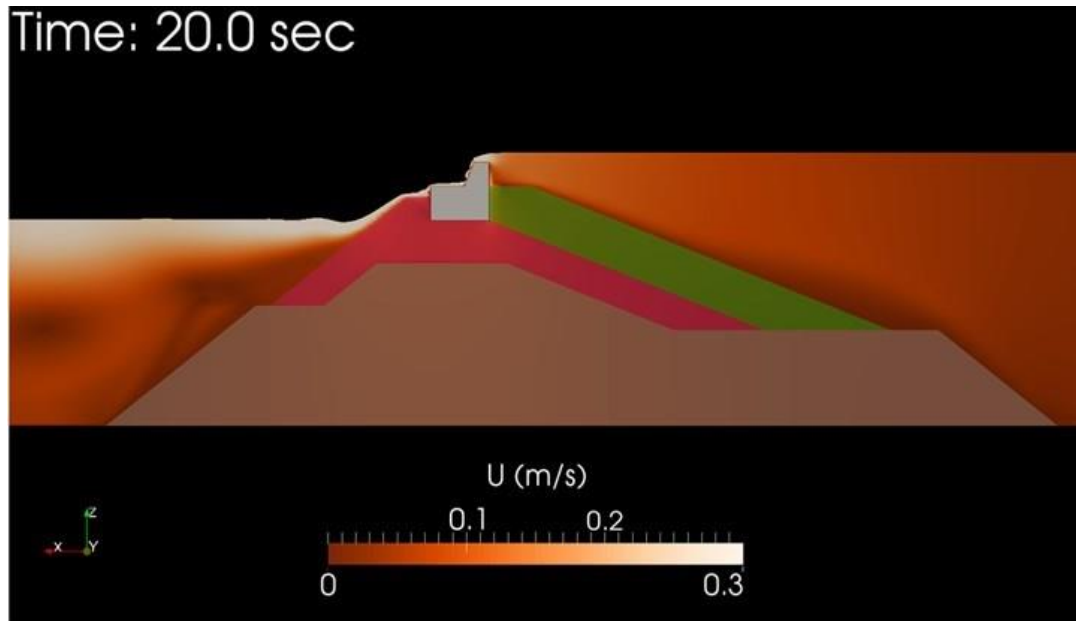
Figure 3.15. A snapshot from the tsunami overflow simulation showing the velocity field around the breakwater (h=1.9 cm)

In Figure 3.15, the velocity field around the breakwater is presented. It is seen that the magnitude of the particle velocities is around 0.3 m/s over the breakwater and at the harbour side.

Thus, the validation of the numerical model is completed based on the experimental data from the tsunami overflow experiment h=1.9 cm since the numerical and experimental results are in agreement in a tsunami overflow simulation conducted with the previously calibrated model parameters given in Table 3.4.

3.2.6   Simulation of a Potential Tsunami Case

Generation of a real tsunami in a wave flume is not possible with the current state-of-art technology as the tsunamis are extremely long waves. One might achieve this by a wave generator having a very long stroke length. However, there is no such

boundaries in the numerical simulations. Therefore, the effect of a potential tsunami on Haydarpaşa Breakwater is studied in this section with the calibrated and validated numerical model, IHFOAM.

Madsen and Fuhrman (2008) studied several wave recordings from the Indian Ocean Tsunami (December 26, 2004) at both deep and relatively shallow water depths, and showed that sufficiently long sinusoidal waves could represent tsunamis. Recently, Larsen et al. (2017) used this argument in the numerical simulations on tsunami-induced scouring. In this section, the effect of a potential tsunami on Haydarpaşa Breakwater, conducting a similar simulation to the calibration/validation stage with a sinusoidal wave.

At this stage, the definitions of the wave heights of solitary and sinusoidal waves and a tsunami used in the present study are given as these changes in different references. The solitary wave height and the tsunami wave height are taken as the distance between the still water level and the crest of these waves. The distance between the still water level and the crest of this wave is defined as the wave amplitude. Therefore, the solitary wave height or tsunami height is assumed to be the amplitude of the sinusoidal wave.

The amplitude and the period of the potential tsunami are selected using the results of a tsunami assessment study conducted in the Sea of Marmara (Aytore et al., 2016). In this reference study, NAMIDANCE is used as the tsunami modelling software that is based on the non-linear shallow equations. The most critical earthquake source for Haydarpaşa Region is shown to be Yalova Normal Fault. The simulated water-surface elevations for Yalova Normal Fault are investigated at eight different locations using the zero-up-crossing methodology, and the average wave period of the potential tsunami in the selected region is calculated as 4 minutes. This period corresponds to 43.8 seconds in the model scale. Aytore et al. (2016) concluded that 3.5 m of tsunami height can be expected in the selected region. The tsunami height is selected as 2.25 m in the prototype scale corresponding to 7.5 cm in the model scale for the present study to make relevant comparisons with the solitary wave

experiment with H=7.5 cm. In the solitary wave experiment with H=7.5 cm, the wave height is measured as 6.34 cm at WG1; therefore, the amplitude and the period of the potential tsunami case are determined as 6.34 cm and 43.8 seconds at WG1, respectively. Water surface elevations and corresponding water particle velocities are taken as inputs at WG1 given by Equations 3.14 and 3.15 assuming that the wave is started with the drawback of water level.

$$\eta(t) = -a_{wave}\, sin(\omega t) \qquad\qquad \text{Eq. 3.14}$$

$$U_{particle}(t) = -U_m\, sin(\omega t)\ \ where\ \ U_m = a_{wave}\sqrt{\frac{g}{h}} \qquad \text{Eq. 3.15}$$

In Equations 3.14 and 3.15, η is the water surface elevation; t is time; a_{wave} is the amplitude of the sinusoidal wave; ω is the angular frequency; $U_{particle}$ is the particle velocity and U_m is the velocity below the tsunamis.

In Figure 3.16, the snapshots from the numerical simulation with the potential tsunami are presented between t=39.0 sec and t=40.0 sec.
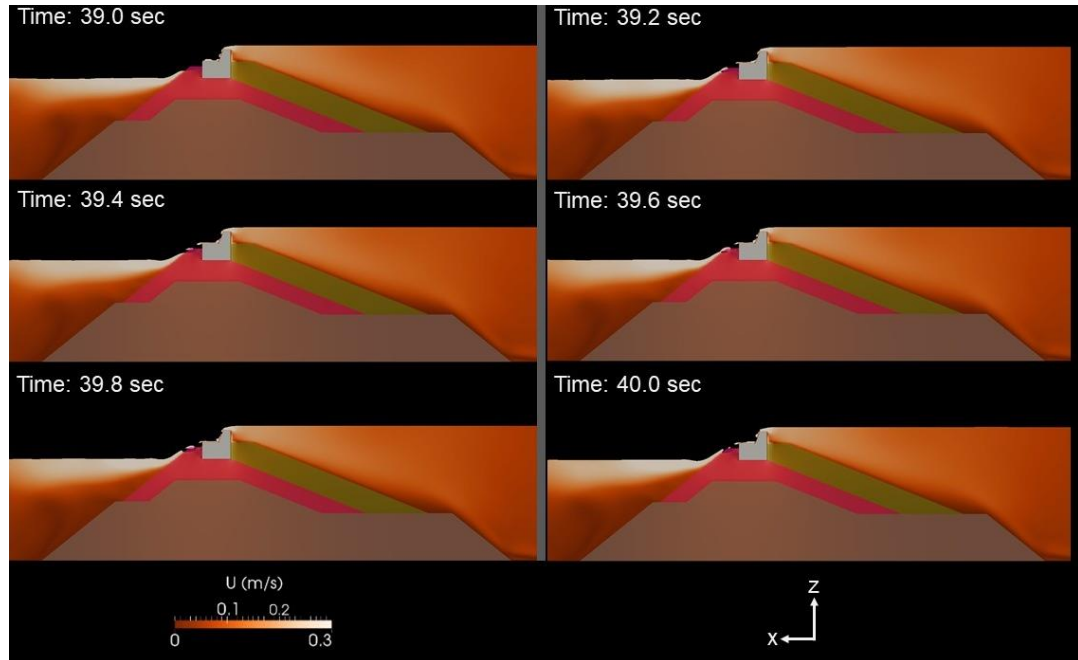
Figure 3.16. The snapshots from the numerical simulation with the potential tsunami

49

It is seen from Figure 3.16 that the maximum velocity around the breakwater is calculated as 0.3 m/s. The water surface elevation at WG8 is plotted in comparison with the corresponding solitary wave (H=7.5 cm) in Figure 3.17.
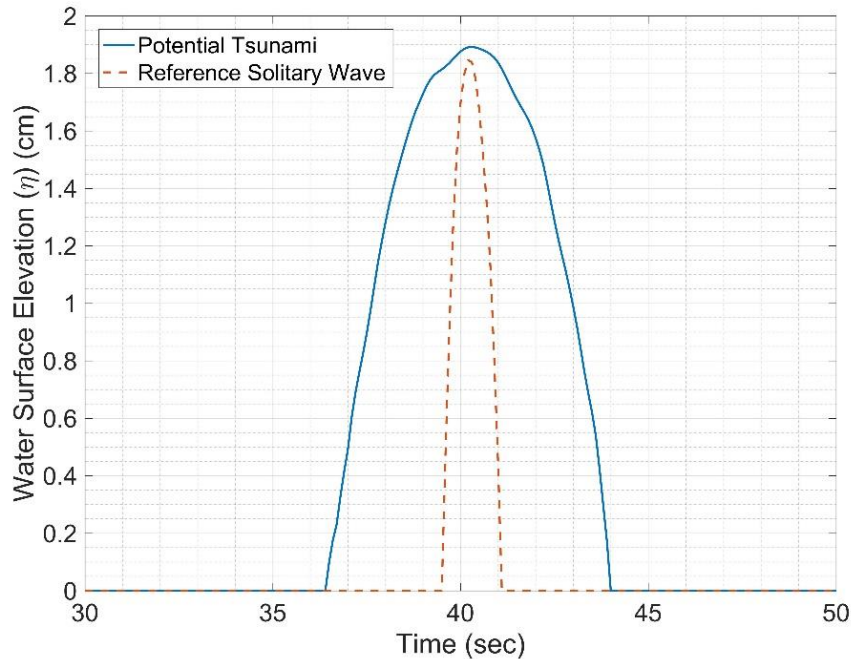
Figure 3.17. Comparison of overflow height at WG8: Potential tsunami (solid blue line), Reference solitary wave (dashed orange line)

Apparently, the peaks of the overflow heights from the solitary wave experiments and the potential tsunami case are matched in Figure 3.17. The overflow height is almost 1.9 cm for both cases. It is observed that the duration of the overflow due to the action of potential tsunami is much longer than the overflow due to the solitary wave. This result shows that the usage of the solitary wave and tsunami overflow experiments together is adequate.

3.2.7   Practical Engineering Applications

One of the principal aims of the present study is to assess the capabilities of the available CFD solvers and to come up with design recommendations based on the

CFD solvers. In this section, two practical engineering applications are performed to achieve these goals.

3.2.7.1   Pressure Forces around the Crown-Wall of the Breakwater and Evaluation of the Stability of the Crown-Wall

The pressure forces around the crown-walls of rubble mound breakwaters are usually computed using empirical relations. These formulas are usually given for the front edge and the bottom edge of the crown-walls, have certain experimental limits and are given for the wind-wave attack in general. For example, there is no formula for estimating pressure forces on all edges of the crown-wall of a rubble mound breakwater. Moreover, there is no explicit formula for evaluating pressure force on the crown-wall of a rubble mound breakwater under solitary wave attack. One of the major opportunities in the CFD modelling is the opportunity of calculating flow parameters on the structures regardless of the geometrical conditions in a rather straightforward way.

In Figure 3.18, the pressure distribution around the crown-wall of Haydarpaşa Breakwater is plotted between t=14.2 sec and t=14.8 sec under the attack of the solitary wave with H=7.5 cm. The edge lengths of the crown-wall are normalized by the solitary wave height (H), and the pressure distributions are normalized with a factor of $\rho g H$ where ρ is the density of the water and g is the gravitational acceleration.
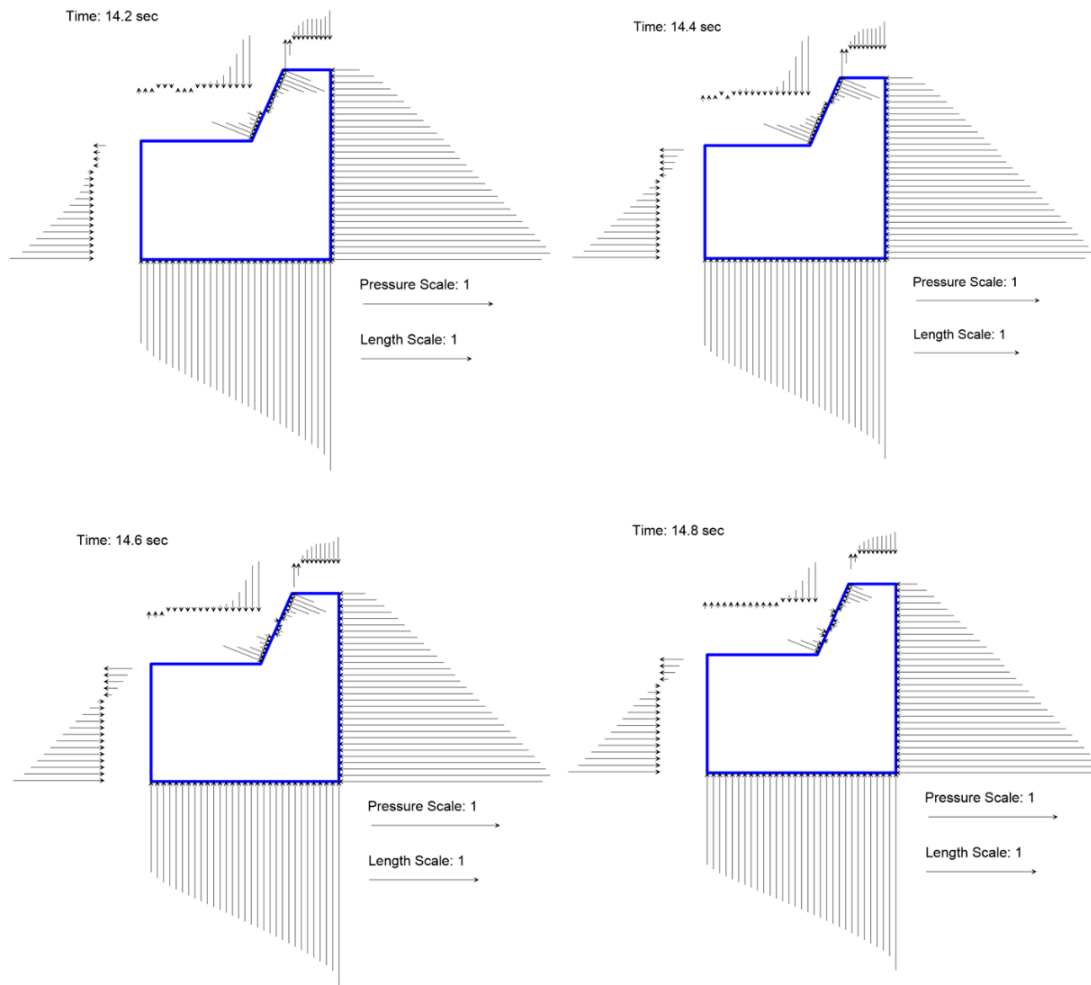
Figure 3.18. The evolution of the pressure distribution around the crown-wall of Haydarpaşa Breakwater under the attack of the solitary wave with H=7.5 cm

In Figure 3.18, it is seen that the primary forces around the crown-wall are acting along the front and bottom edges, and these forces do not change significantly during the overflow of the solitary wave. It would be useful for a designer to observe the forces along the other edges of the crown-wall.

Another opportunity can be computing the stability of the crown-wall under these forces based on the safety factors. In the rest of this section, the variations of the safety factors in time are presented. The factors of safety against sliding and overturning are calculated using Equations 3.16 and 3.17, respectively.

$$FS_{sliding} = \frac{\mu_s \sum F_z}{\sum F_x}$$

Eq. 3.16

$$FS_{overturning} = \frac{\sum M_{resisting}}{\sum M_{driving}}$$

Eq. 3.17

In Equation 3.16, $\sum F_z$ is the vectoral summation of the weight of the crown-wall and the pressure forces in the vertical direction; $\sum F_x$ is the vectoral summation of the pressure forces in the horizontal direction and μ_s is the static friction coefficient between the crown-wall and the rubble stones. The value of the friction coefficient is taken as 0.45 as measured in the physical model experiments. In Equation 3.17, $M_{resisting}$ is the summation of the resisting moments and $M_{driving}$ is the summation of the driving moments in clockwise and counter-clockwise directions, respectively. In these equations, the supporting forces due to the stone at the harbour side of the breakwater is not considered. Although this force could be a game-changer in the calculations, it is not included as an estimation of this force is not straightforward, and this force is investigated in Section 3.2.7.2. Therefore, qualitative discussions are carried out with the variation of safety factors in time. In other words, when the factor of safety (FS) is bigger than one (FS>1), the crown-wall is certainly stable according to the numerical calculations as the supporting force is a resisting force. However, if FS is lower than one (FS<1), one cannot conclude whether the crown-wall is stable or not using the numerical results. The variations of safety factors are given in Figure 3.19, Figure 3.20 and Figure 3.21 for the solitary wave case with H=7.5 cm, for the tsunami overflow case with h=1.9 cm and the potential tsunami case, respectively.
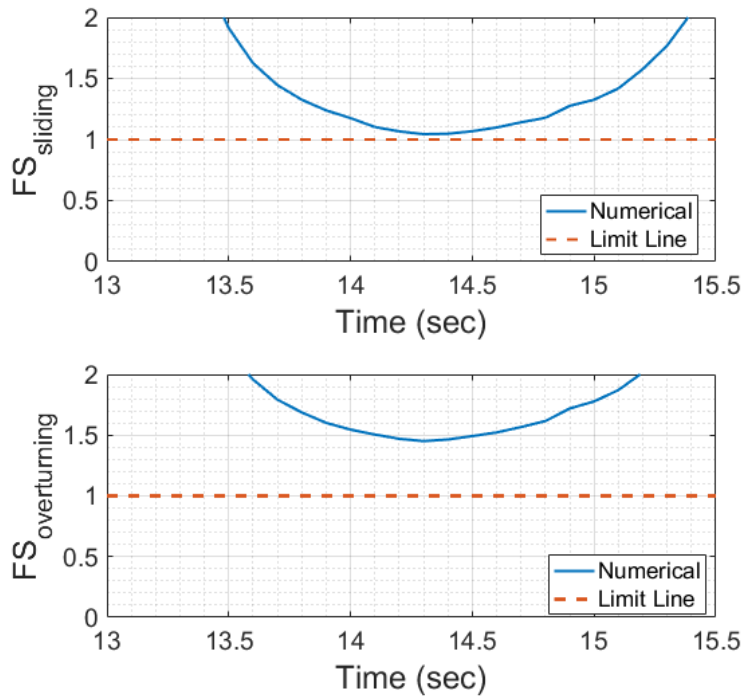
Figure 3.19. Variation of safety factors for the solitary wave case with H=7.5 cm
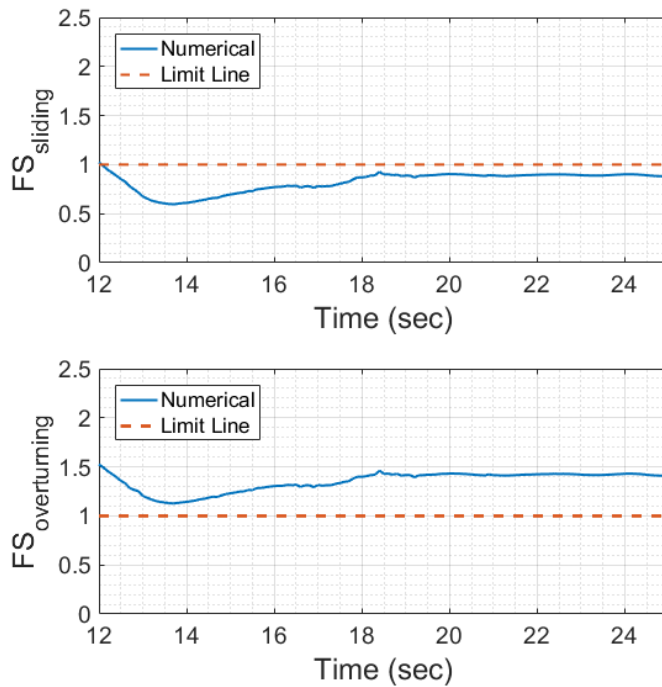
Figure 3.20. Variation of safety factors for the tsunami overflow case with h=1.9 cm
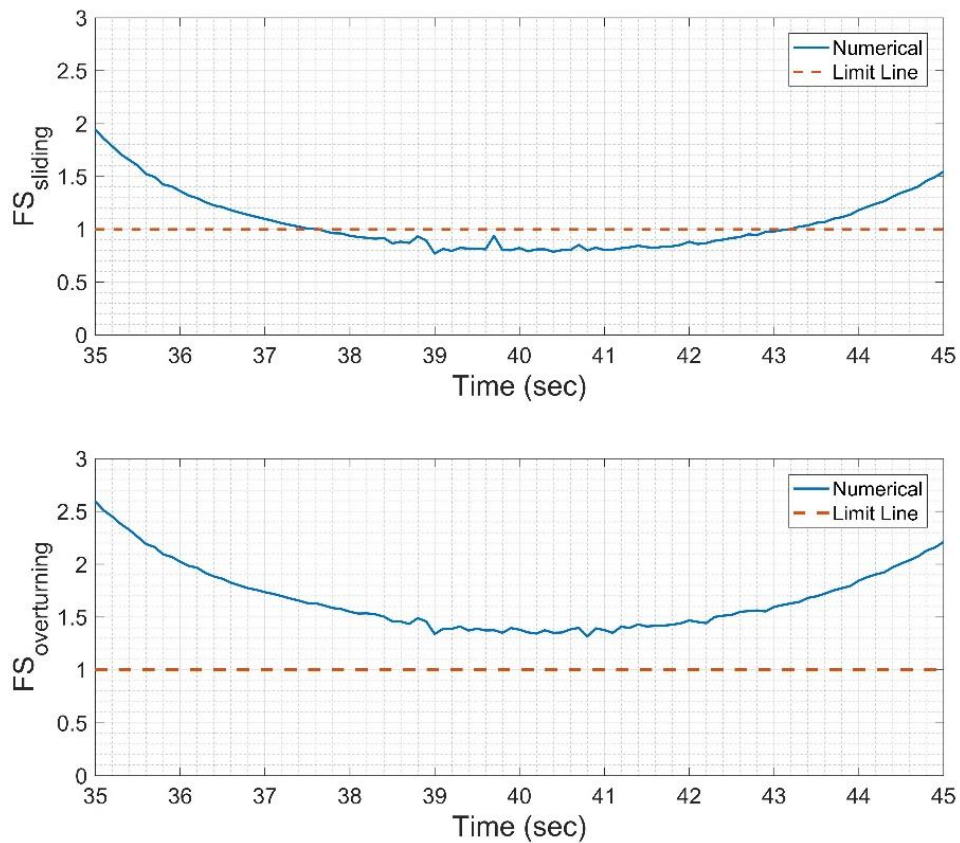
Figure 3.21. Variation of safety factors for the potential tsunami case

In Figure 3.19, it is seen that the crown-wall is stable against both sliding and overturning parallel to the experimental observation. As the supporting force adds more stability, this result is reliable. It is observed from Figure 3.20 and Figure 3.21 that the crown-wall is stable against overturning; on the other hand, the crown-wall is not stable against sliding. Although the increase in the safety factors due to the supporting force can push the curve over the limiting line, the effect of the supporting force cannot be concluded precisely due to the lack of information for these cases. However, the empirical formulas used to assess the stability of the crown-wall under wind-wave attack such as Pedersen (1996) also do not consider the effect of the supporting forces. Therefore, one might still use this type of results in deciding the stability condition without considering the supporting forces being on the safe side.

3.2.7.2   Estimation of the Forces Acting on the Single Stone Behind the Crown-Wall at the Harbour Side of the Breakwater

In the previous section, it is shown that the supporting force acting on the crown-wall can be significant in deciding the stability condition of the breakwater. There is no direct way to estimate the supporting force using the present numerical model. In the physical model experiments part, it is seen that the stability of the crown-wall; and thus, the overall cross-section, strongly depends on the stability of the stones at the harbour side of the breakwater. As these stones move, the supporting forces decrease, and the crown-wall might be slid. Therefore, the forces acting on the single stone behind the crown-wall located at the top layer of harbour side armour layer, -hereafter the single stone- are evaluated in this section approximately to provide a design recommendation. In the rest of this section, the forces acting on the single stone are derived theoretically, and these forces are computed using the information from the numerical simulation. A free-body diagram for the forces acting on the single stone is presented in Figure 3.22.
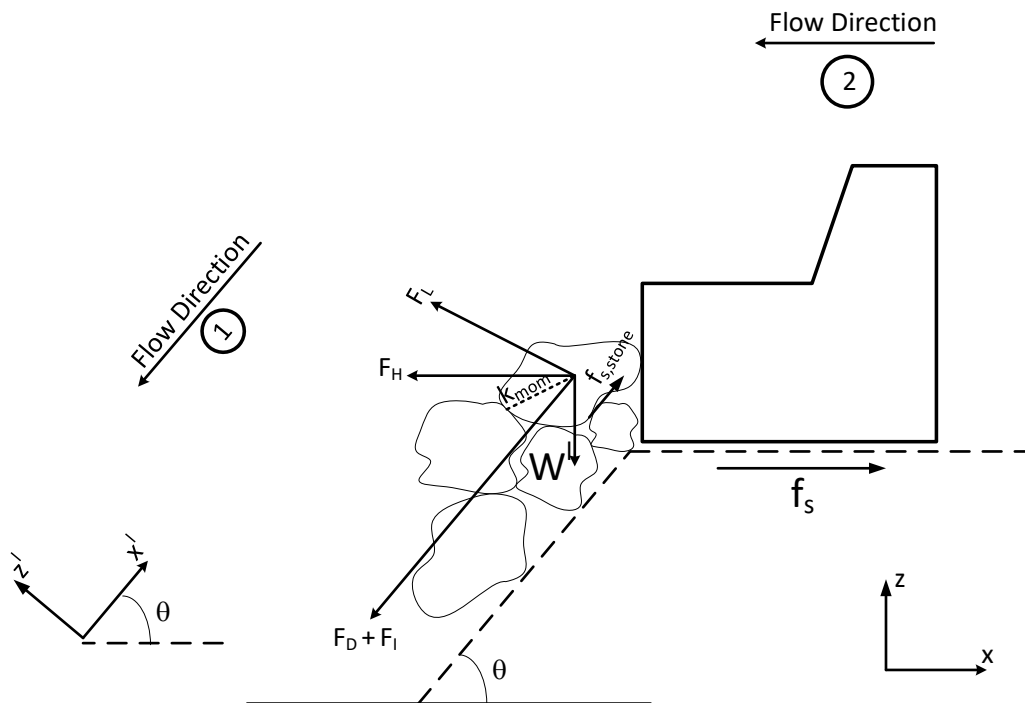
Figure 3.22. Free-body diagram of forces acting on the single stone

In Figure 3.22, F_D, F_L and F_I are drag, lift and inertia forces, respectively; W' (W_{sub}) is the submerged weight of the stone; $f_{s,stone}$ is the friction force between the single stone and the underlying stones; F_H is the horizontal transferred force induced from the pressure forces acting around the crown-wall; f_s is the friction force between the crown-wall and the underlying stones and k_{mom} is the moment arm for the single stone. Furthermore, the acting flow directions are also shown on this free-body diagram.

Drag, inertia and lift forces are defined in Equations 3.18-3.20 as follows:

$$F_D = \frac{1}{2} C_D \, \rho U_{ave}^2 \left(\frac{\pi D_{50}^2}{4} \right)$$ Eq. 3.18

$$F_I = C_M \, \rho \frac{dU_{ave}}{dt} \left(\frac{\pi D_{50}^2}{4} \right)$$ Eq. 3.19

$$F_L = \frac{1}{2} C_L \, \rho U_{ave}^2 \left(\frac{\pi D_{50}^2}{4} \right)$$ Eq. 3.20

In these equations, ρ the density of water which is 1000 kg/m³; U_{ave} is the average flow velocity; dU_{ave}/dt is the instantenous acceleration computed using the change in the average velocity; D_{50} is the nominal stone diameter, and C_D, C_M and C_L are the drag, inertia and lift coefficients, respectively. The average velocity (U_{ave}) is computed by integrating the velocity distribution along the line perpendicular to the flow direction 1 at each time step during the flow over the single stone. The velocity information is taken from the cells along this line having at least 0.5 of VOF function value.

The horizontal transferred force is given by Equation 3.21.

$$F_H = \sum F_x - f_s = \sum F_x - \mu \sum F_z$$ Eq. 3.21

In this equation, $\sum F_x$ and $\sum F_z$ is the vectorial summation of the forces acting on the crown-wall in the horizontal and vertical directions, respectively, and μ is the

friction coefficient between the crown-wall and the underlying stones. The submerged weight of the stone is given by Equation 3.22.

$$W' = W_{sub} = (\rho_s - \rho) D_{50}^3$$
Eq. 3.22

where the density of the stones (ρ_s) is taken as 2650 kg/m³.

There are three stability conditions for the single stone: i) Sliding along x' direction, ii) Movement normal to the structure slope, iii) Rolling about the contact point. The first condition is given by Equation 3.23.

$$F_D + F_I + F_H \cos\theta + W_{sub} \sin\theta \le f_{s,stone}$$
Eq. 3.23

where θ is the structure slope angle taken as 39°. $f_{s,stone}$ is given by Equation 3.24.

$$f_{s,stone} = (W_{sub} \cos\theta - F_L - F_H \sin\theta) \tan\phi_{rep}$$
Eq. 3.24

where ϕ is the angle of repose.

The second condition is given by Equation 3.25.

$$F_L + F_H \sin\theta \le W_{sub} \cos\theta$$
Eq. 3.25

The final stability condition is given by Equation 3.26.

$$k_{mom}\left[(F_L + F_H \sin\theta) \sin\phi_{rep} + (F_H \cos\theta + F_D + F_I) \cos\phi_{rep}\right]$$
$$\le k_{mom} W_{sub} \sin(\phi_{rep} - \theta)$$
Eq. 3.26

It is noted that these equations are written disregarding the stone angularity or shape, stone interlocking, supporting forces due the stones at the lower layers at the harbour side and surface friction. Furthermore, the first and third stability conditions are considered for further computations, as the movement of the stones due to second stability condition is not observed in the physical model experiments. Equations 3.23 and 3.26 are reorganized to collect the terms that can be calculated with the information from the numerical simulations given by Equations 3.27 and 3.28, respectively.

58

$$C_D + C_L \, tan\,\phi_{rep} \leq$$

$$\frac{W_{sub}\, cos\,\theta\, tan\,\phi_{rep} - F_H\, sin\,\theta\, tan\,\phi_{rep} - F_H\, cos\,\theta - W_{sub}\, sin\,\theta - C_M\, \rho\, \dfrac{dU_{ave}}{dt}\left(\dfrac{\pi D_{50}^2}{4}\right)}{\dfrac{1}{2}\rho U_{ave}^2\left(\dfrac{\pi D_{50}^2}{4}\right)} \qquad \text{Eq. } 3.27$$

$$C_D \, cos\,\phi_{rep} + C_L \, sin\,\phi_{rep} \leq$$

$$\frac{W_{sub}\, sin\left(\phi_{rep}-\theta\right) - F_H\left(sin\,\theta\, sin\,\phi_{rep} + cos\,\theta\, cos\,\phi_{rep}\right) - C_M\, \rho\, \dfrac{dU_{ave}}{dt}\left(\dfrac{\pi D_{50}^2}{4}\right)cos\,\phi_{rep}}{\dfrac{1}{2}\rho U_{ave}^2\left(\dfrac{\pi D_{50}^2}{4}\right)} \qquad \text{Eq. } 3.28$$

The right-hand sides of these Equation 3.27 and 3.28 are named as *S (Sliding)* and *R (Rolling)*, respectively. These parameters are non-dimensional, and calculated using the numerical simulations to find approximate stability conditions based on these parameters. The inertia coefficient (C_M) and the angle of repose (ϕ_{rep}) are taken as 1.5 and 50°, respectively, as recommended by Kobayashi and Greenwald (1986) and Kobayashi and Otta (1987). The major uncertainty in these equations is the inertial coefficient which can be experimentally determined. However, the inertia force corresponds to 5-7% of driving forces; therefore, it is assumed that this approximation of the inertia coefficient suggested by the associated literature is acceptable. The computations are firstly carried for the tsunami overflow experiment with h=1.9 cm. The results are presented for this case in Figure 3.23.
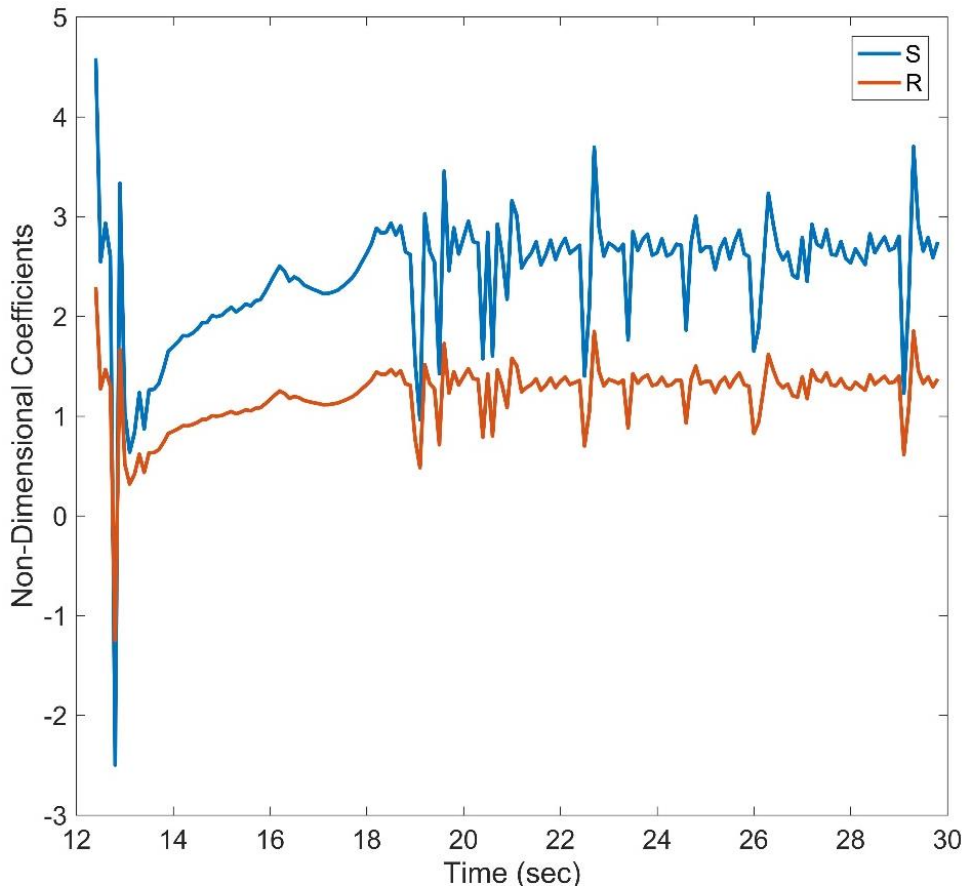
Figure 3.23. Variation of the non-dimensional S (blue solid line) and R (orange solid line) parameters in time for the tsunami overflow experiment with h=1.9 cm

In order to interpret Figure 3.23, the averages of S and R parameters denoted as $\overline{S}$ and $\overline{R}$, respectively, are computed between t=20 sec and t=30 sec, which are calculated as $\overline{S} = 2.62$ and $\overline{R} = 1.31$ for this case.

These calculations are extended with additional tsunami overflow simulations ranging between h=1.05 cm and h=2.15 cm as the movement of the harbour side stones has a significant effect on the stability of the cross-section for these cases. In the physical model experiments, the tsunami overflow experiments conducted on the original cross-section of Haydarpaşa Breakwater was in between h=1.1 cm and h=1.95 cm. In Table 2, both the numerical and experimental results are presented.

Table 3.5 Comparison of non-dimensional parameters with experimental results

Physical Model Experiment #	h (cm)	Stability Condition	Numerical Test #	h (cm)	$\bar{S}$	$\bar{R}$
1	1.1	No damage	tr25	1.05	3.29	1.65
2	1.15	No damage	tr26	1.22	3.13	1.56
3	1.2	No damage	tr27	1.4	2.98	1.45
4	1.3	No damage	tr28	1.63	2.87	1.39
5	1.4	No damage	tr29	1.75	2.66	1.34
6	1.7	Failure	tr30	1.9	2.62	1.31
7	1.85	No damage	tr31	2.0	2.58	1.29
8	1.9	Failure	tr32	2.15	2.35	1.17
9	1.95	Failure				

It is seen from Table 3.5 that $\bar{S}$ and $\bar{R}$ decrease as the tsunami overflow height increases. This is an expected result as the lower values of these non-dimensional values indicate a lower level of stability. This results also show that the sliding of the stone is more critical than the rolling of the stone.

These non-dimensional parameters are also calculated for the solitary wave experiments with H=7.5 cm and H=10 cm and the potential tsunami case. As the overflow duration is shorter for these cases, the averages of these non-dimensional parameters are calculated assuming 50% of the overflow duration is significant for the motion of the single stone. These durations are taken in the neighbourhood of the time corresponds to the peak overflow height. The non-dimensional parameters for the solitary wave experiment with H=7.5 cm are calculated as $\bar{S} = 2.98$ and $\bar{R} = 1.45$. According to Table 3.5, these results indicate the stability of the single stone. On the other hand, these parameters take negative values for the solitary wave experiment with H=10 cm as F_H governs the process. Moreover, the non-dimensional parameters are calculated as $\bar{S} = 2.49$ and $\bar{R} = 1.25$ for the potential tsunami case. It is noted that these values correspond to the tsunami overflow case with h=1.9 cm.

Overall, it is seen from these estimations that the experimental results are parallel to the numerical results. Therefore, it is possible to provide design recommendations

from these simulations. As there is a grey region in the physical model experiments between h=1.7 cm and h=1.9 cm, it is suggested that the single stone is stable when $\overline{S}$ is bigger than 2.8 and $\overline{R}$ is bigger than 1.45. Although the results strongly depend on the geometry of the structure and the wave/flow conditions, these threshold values could be used for a starting point in the design of a similar conventional rubble mound breakwater under tsunami attack.

3.3   Overall Conclusions from Experimental and Numerical Studies

The overall conclusions from the physical model experiments and the numerical modelling studies from Chapter 3 are given as follows:

- Both solitary wave and tsunami overflow experiments showed that the major failure mechanism of Haydarpaşa Breakwater is the sliding of the crown-wall of the breakwater. In the solitary wave experiments, the pressure forces govern the process. On the other hand, the scouring of the stones at the harbour side of the breakwater is also significant in the tsunami overflow experiments. The counter-measure cross-section is capable of overcoming this failure mechanism.

- It is seen that the use of solitary waves and tsunami overflow experiments together to assess the performance of a rubble mound breakwater is relevant as it is required to consider the effect of time elapsed during tsunami overflow.

- The numerical model IHFOAM based on the OpenFOAM CFD library is calibrated with and validated against the experiments conducted on Haydarpaşa Breakwater. Effect of a potential tsunami is also studied.

- The computational times are also recorded for each simulation. The computational time required on 12 threads (Intel® Xeon® E5-1650 v3 2.2 GHz with 16 GB RAM) are about 24 hours, 150 hours and 191 hours for the solitary wave experiments, tsunami overflow experiments and potential tsunami case, respectively.

- In the scope of engineering applications, the safety factors around the crown-wall of Haydarpaşa Breakwater are evaluated. The investigations are extended to estimate the forces acting on the single stone at the harbour side. In general, the results of the engineering applications are in parallel to the physical model experiments. Several recommendations for the design of rubble mound breakwaters under tsunami attack are given.

Although the hydrodynamics around the rubble mound breakwater including the estimation of forces acting on the structural elements of the rubble mound breakwater are modelled accurately, the available numerical model cannot evaluate the motion and collision of the rubble stones since it does not provide a solution for moving boundaries and colliding particles. Thus, the damage along the rubble mound breakwaters can be evaluated qualitatively. A quantitative evaluation of the damage can be achieved with a numerical model that can calculate the motion and the collision of the stones which might be a step forward to develop a design tool covering the failure modes of rubble mound breakwaters.

CHAPTER 4

NUMERICAL MODELLING OF THE MOTION AND THE COLLISION OF SOLID SPHERES UNDER WAVE ATTACK: APPLICATION OF A NON-RESOLVING CFD-DEM MODEL

The available computational fluid dynamics solvers are capable of simulating hydrodynamics around coastal structures, as presented in Chapter 3 for rubble mound breakwaters in particular. The next step is to evaluate the damage in these structures. The damage along the rubble slopes could be predicted using computational fluid dynamics (CFD) solvers coupled with particle motion solvers. In engineering applications, the discrete element method (DEM) is the most common approach.

In this part of the study, a simple experimental study is carried out focusing on the motion and collision of two spherical particles representing the rubble stones. These experiments are modeled using a CFD solver coupled with a DEM solver called CADMAS-2VF-DEM (Arikawa et al., 2011). Spherical particles are selected as most of the DEM codes use spheres as the starting point. The reason why is that the contact detection between the spherical particles is trivial; therefore, the calculation of the forces is more straightforward.

4.1   Physical Model Experiments

The physical model experiments are carried out in the wave flume of METU Ocean Engineering Research Center. METU Wave Flume has a length, depth, and width of 26 m, 6 m, and 1 m, respectively. An inner channel having a width of 0.9 m was constructed to conduct these experiments. A 1:20 slope was constructed, followed by a horizontal flat area 30 cm above the ground level. The spherical particles (two billiard balls) were placed on this flat area with a center-to-center distance of 8 cm colored as red and yellow. The diameter of the billiard balls is 6 cm whereas their

density is 1.9 g/cm^3 which is lower than a regular rubble stone. The water level was set as 33 cm; therefore, half of the billiard balls were in the water. The water surface elevation along the wave channel was measured using five-wave gauges (WG1-WG5). The side view of the channel is given in Figure 4.1.
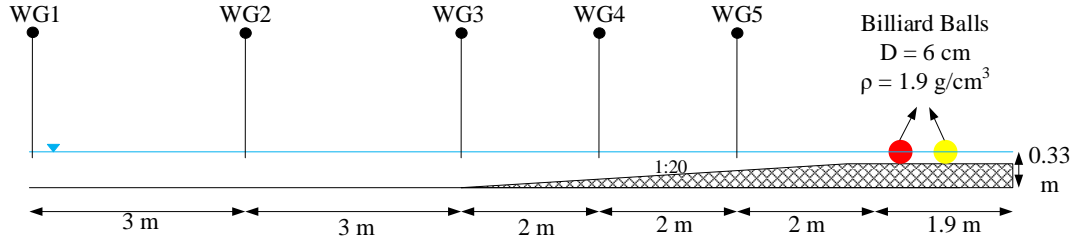
Figure 4.1. Side View of the Experimental Setup

The wave condition was selected as a 6.6 cm solitary wave at WG1 that reaches to 7.8 cm at WG5. This solitary wave breaks on the spherical particles. The solitary waves were generated using a piston-type wave generator based on a new methodology suggested by Malek-Mohammadi and Testik (2010) modifying the typical implicit relationship for wave paddle trajectory given by Goring (1979). Synolakis (1990) reported that Goring (1979) approach does not resolve the unsteady nature of the solitary wave generation. In the new methodology, the evolving nature of the solitary wave generation is considered. Malek-Mohammadi and Testik (2010) argue that more precise solitary waves in terms of the wave height, profile shape and celerity can be generated by this new methodology in both short and long wave flumes where the wave paddle trajectory is given by Equation 4.1 which is an implicit equation. The reader is referred to the reference paper for the derivation of this equation.

$$\frac{d\xi}{dt} = \sqrt{g\frac{\eta_{wave}}{h_{water}}\left(h_{water} + \frac{\eta_{wave}}{2}\right)\left(\frac{\eta_{wave}}{h_{water} + \eta_{wave}}\right)} \qquad \text{Eq. 4.1}$$

In this equation, ξ is wave paddle trajectory, t is time, g is the gravitational acceleration, h_{water} is the still water depth and η_{wave} is the wave profile for the solitary

66

wave. The approximate solution for the solitary wave profile by Boussinesq is given in Equation 4.2.

$$\eta_{wave} = H \operatorname{sech}^2 \left[k_{decay} \left(ct - \xi \right) \right]$$
Eq. 4.2

where H is the solitary wave height, k_{decay} is the outskirt decay coefficient defined as $\sqrt{(3H)/(4h_{water}^3)}$, and c is the wave celerity defined as $\sqrt{g(h_{water} + H)}$.

Equation 4.1 is integrated to generate solitary waves with this new methodology based on the Boussinesq's solution, and included in the METU Wave Flume Wave Generation/Analysis Suite.

In the experiments, the motion of the spheres was recorded using a camera placed on the top of the flat area. The model of the camera is SONY Cybershot DSC-HX7V, and the recordings were taken at 25 Hz. The paths of the particles are computed using an image processing code developed in the scope of this study described in Section 4.1.1. The experiments were repeated five times to reduce the randomness in the results.

4.1.1   Analysis of the Video Recordings

The paths of the spheres under wave attack are tracked using an image processing technique called color-based tracking. A similar algorithm is presented by Stolle et al. (2016) used to track debris motion under wave attack. The algorithm implemented in MATLAB environment in the scope of this study is outlined as follows:

- The video recordings having a sampling rate of 25 Hz are divided into frames.
- Each frame is corrected for lens distortion.
- A calibration factor is determined for each video recording using the checkerboard placed on the flat area in the physical model experiments.

67

- The colors of the spheres are differentiated based on the Hue-Saturation-Value (HSV) at each pixel of the frames. Thus, red and yellow regions in the frames are determined.
- The centroids of these regions are calculated. These centroids correspond to the centers of the spheres.
- The algorithm is repeated until the end of the video recording.

The actual and tracked positions of the spheres are given in Figure 4.2 for t=11.72 sec and t=13.00 sec in the experiments. It is noted that the red sphere is tracked with a black dot, whereas the yellow sphere is tracked by a pink dot.

(a) t=11.72 sec

(b) t=13.00 sec
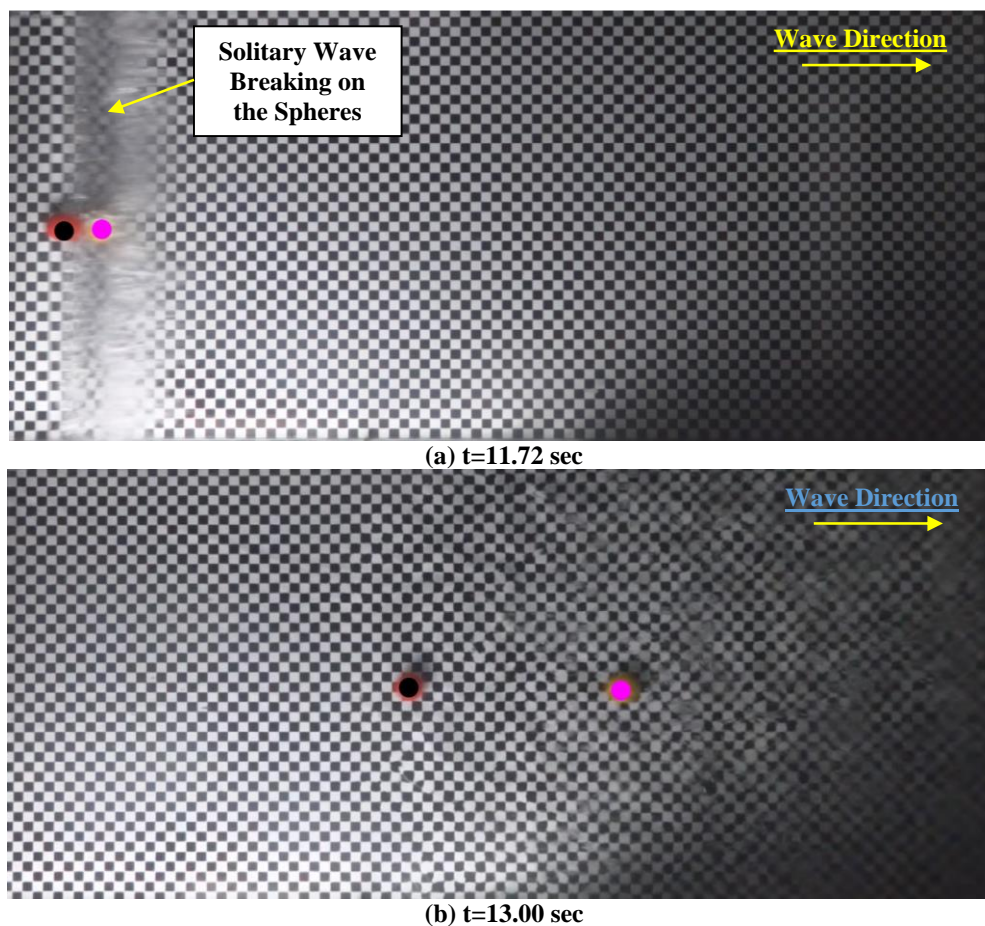
Figure 4.2. The actual and tracked positions of the red and yellow spheres

It is seen from Figure 4.2 that the positions of the particles can be followed in a good accuracy with the image processing code.

4.2 Numerical Modelling Studies

4.2.1 Description of the Numerical Model

The numerical model is developed by Arikawa et al. (2011), coupling a two-phase CFD solver called CADMAS-2VF (Arikawa et al., 2007) with a discrete element method solver called DEM. In each time step, the CFD part solves the flow properties in the computational domain, sends this information to the DEM part to evaluate the positions of the particles. The new position information is sent back to the CFD part. This procedure is repeated until the end of the simulation. The particles are represented as porous regions in the CFD part. Therefore, the velocity and pressure field around the particles cannot be adequately resolved in this numerical model. However, it is still possible to use this type of model when there is no need to resolve the flow properties around these particles. This type of numerical models are solved non-resolving, and the coupling methodology is referred to as weak-coupling.

In the CFD part, multiphase Reynolds-Averaged Navier-Stokes (RANS) equations are solved, including a porous body model. Also, the effect of air compressibility is considered in this solver with a specific term included in the continuity equation given by Equation 4.3 and momentum equations given by Equations 4.4-4.6 for x, y and z directions. The below-given equations are solved using the finite difference method, and the model works on structured computational mesh configurations.

$$\frac{\partial \gamma_x u}{\partial x} + \frac{\partial \gamma_y v}{\partial y} + \frac{\partial \gamma_z w}{\partial z} = \gamma_v S_\rho - \frac{1-\alpha}{\rho_G} \hat{\rho}_G \qquad \text{Eq. 4.3}$$

69

$$\lambda_v \frac{\partial u}{\partial t} + \frac{\partial \lambda_x uu}{\partial x} + \frac{\partial \lambda_y vu}{\partial y} + \frac{\partial \lambda_z wu}{\partial z} = -\frac{\gamma_v}{\rho}\frac{\partial p}{\partial x} - u\frac{1-F}{\rho_G}\hat{\rho}_G$$

$$+ \frac{\partial}{\partial x}\left\{\gamma_x v_e\left(2\frac{\partial u}{\partial x}\right)\right\} + \frac{\partial}{\partial y}\left\{\gamma_y v_e\left(\frac{\partial u}{\partial y} + \frac{\partial v}{\partial x}\right)\right\} \qquad \text{Eq. 4.4}$$

$$+ \frac{\partial}{\partial z}\left\{\gamma_z v_e\left(\frac{\partial u}{\partial z} + \frac{\partial w}{\partial x}\right)\right\} - \gamma_v D_x u - R_x + \gamma_v S_u$$

$$\lambda_v \frac{\partial v}{\partial t} + \frac{\partial \lambda_x uv}{\partial x} + \frac{\partial \lambda_y vv}{\partial y} + \frac{\partial \lambda_z wv}{\partial z} = -\frac{\gamma_v}{\rho}\frac{\partial p}{\partial y} - v\frac{1-\alpha}{\rho_G}\hat{\rho}_G$$

$$+ \frac{\partial}{\partial x}\left\{\gamma_x v_e\left(\frac{\partial v}{\partial x} + \frac{\partial u}{\partial y}\right)\right\} + \frac{\partial}{\partial y}\left\{\gamma_y v_e\left(2\frac{\partial v}{\partial y}\right)\right\} \qquad \text{Eq. 4.5}$$

$$+ \frac{\partial}{\partial z}\left\{\gamma_z v_e\left(\frac{\partial v}{\partial z} + \frac{\partial w}{\partial y}\right)\right\} - \gamma_v D_y v - R_y + \gamma_v S_v$$

$$\lambda_v \frac{\partial w}{\partial t} + \frac{\partial \lambda_x uw}{\partial x} + \frac{\partial \lambda_y vw}{\partial y} + \frac{\partial \lambda_z ww}{\partial z} = -\frac{\gamma_v}{\rho}\frac{\partial p}{\partial x} - w\frac{1-\alpha}{\rho_G}\hat{\rho}_G$$

$$+ \frac{\partial}{\partial x}\left\{\gamma_x v_e\left(\frac{\partial w}{\partial x} + \frac{\partial u}{\partial z}\right)\right\} + \frac{\partial}{\partial y}\left\{\gamma_y v_e\left(\frac{\partial w}{\partial y} + \frac{\partial v}{\partial x}\right)\right\} \qquad \text{Eq. 4.6}$$

$$+ \frac{\partial}{\partial z}\left\{\gamma_z v_e\left(2\frac{\partial w}{\partial z}\right)\right\} - \gamma_v D_z w - R_z + \gamma_v S_w - \frac{\gamma\rho^* g}{\rho}$$

In Equations 4.3-4.6, x, y and z are horizontal, transverse and vertical directions; u, v and w are the velocities in the x, y and z directions, respectively; t is time; ρ is the density of the water; ρ_G is the density of air; $\hat{\rho}_G$ is the derivative of the density of air which is related to the calculation of air compressibility; p is pressure; α is the ratio of fluid volume in a cell; v_e is the effective viscosity defined as the summation of the molecular viscosity and the eddy viscosity; γ_v the volumetric porosity; γ_x, γ_y and γ_z are the permeability coefficients in x, y and z directions, respectively and g is the acceleration of gravity. λ_v, λ_x, λ_y, λ_z, R_x, R_y and R_z are the terms related to the porous body model calculating the damping related to drag and inertia forces in the

porous medium. λ_v, λ_x, λ_y and λ_z are defined in Equation 4.7 based on the inertia coefficient C_M and the permeability coefficients:

$$
\begin{aligned}
\lambda_v &= \gamma_v + (1-\gamma_v)C_M \\
\lambda_x &= \gamma_x + (1-\gamma_x)C_M \\
\lambda_y &= \gamma_y + (1-\gamma_y)C_M \\
\lambda_z &= \gamma_z + (1-\gamma_z)C_M
\end{aligned}
\qquad \text{Eq. 4.7}
$$

R_x, R_y and R_z are defined as resistance terms due to the porous media given by Eq. 4.8:

$$
\begin{aligned}
R_x &= \frac{1}{2}\frac{C_D}{dx}(1-\gamma_x)u\sqrt{u^2+v^2+w^2} \\
R_y &= \frac{1}{2}\frac{C_D}{dy}(1-\gamma_y)v\sqrt{u^2+v^2+w^2} \\
R_z &= \frac{1}{2}\frac{C_D}{dz}(1-\gamma_z)w\sqrt{u^2+v^2+w^2}
\end{aligned}
\qquad \text{Eq. 4.8}
$$

In Equation 4.8, C_D is the drag coefficient; dx, dy and dz are the mesh sizes along x, y and z directions. The effect of the air compressibility is included in this model by taking the rate of change in the density of the air ($\hat{\rho}_G$) evaluated both temporally and spatially given in Equation 4.9:

$$
\hat{\rho}_G = \gamma_v\frac{\partial \rho_G}{\partial t} + \gamma_x u\frac{\partial \rho_G}{\partial x} + \gamma_y v\frac{\partial \rho_G}{\partial y} + \gamma_z w\frac{\partial \rho_G}{\partial z}
\qquad \text{Eq. 4.9}
$$

In CADMAS-2VF, the waves are generated using the source terms S_p, S_u, S_v and S_w and absorbed by employing D_x, D_y and D_z that are energy dissipation coefficients given in the Equations 4.3-4.6. The wave absorption is activated mostly along the boundaries using a sponge layer based on the energy dissipation coefficients.

The free-surface is captured using the Volume of Fluid (VOF) methodology in this flow solver. As stated in the previous chapters, a scalar function (F in this solver) is defined at each cell in the computational domain. F takes a value of 1 when the cell

71

is full of liquid whereas it takes a value of 0 when the cell is full of gas. VOF method is applied by solving the VOF-advection equation given by Equation 4.10.

$$\gamma_v \frac{\partial \alpha}{\partial t} + \frac{\partial \gamma_x u\alpha}{\partial x} + \frac{\partial \gamma_y v\alpha}{\partial y} + \frac{\partial \gamma_z w\alpha}{\partial z} = \gamma_v S_\alpha \qquad \text{Eq. 4.10}$$

In Equation 4.9, S_α is another source term for wave generation. Finally, the RANS equations are closed using k-ε turbulence closure in CADMAS-2VF.

In the DEM part of this coupled numerical model, Newton's equations of motion are solved given by Equations 4.11 and 4.12.

$$m \frac{du_{pi}}{dt} = F_{pi} \qquad \text{Eq. 4.11}$$

$$I \frac{d\omega_{pi}}{dt} = T_{pi} \qquad \text{Eq. 4.12}$$

In Equations 4.11 and 4.12, t is time; m is the mass and I is the moment of inertia of the particle; u_{pi} and ω_{pi} are the velocity and angular velocity of the particle, respectively; F_{pi} is the forces and T_{pi} is the torque acting on the particle. The forces acting on the particle are grouped as forces due to the fluid motion (f_{wp}, taken as wave pressure forces in this model), collision forces between the particles and the reaction forces from the walls (boundaries) of the computational domain. The reaction forces are also evaluated as collision forces, and these two forces together referred to as f_c.

This DEM code is originally developed for evaluating the damage in the vertical walls under wave attack. The vertical walls are represented with spherical particles, and these particles are connected with bonds. The DEM code computes the forces on these particles based on the wave pressure and evaluates whether the bonds are broken or not. In the present study, the DEM code is slightly modified as the problem of interest is different. In this new version of the DEM code, the wave pressures are integrated on the particle from the cells around the particle with a distance-based weighting factor. The force update equation is given by Equation 4.13 for x, y and z

directions, and the integration of the pressure forces is schematized for x-direction in Figure 4.3.

$$f_{wp,i} = f_{wp,i} + f_1 - f_2$$

In Equation 4.13, $f_{wp,i}$ is the force acting on the particle along i'th direction, f_1 is the driving force and f_2 is the resisting force.
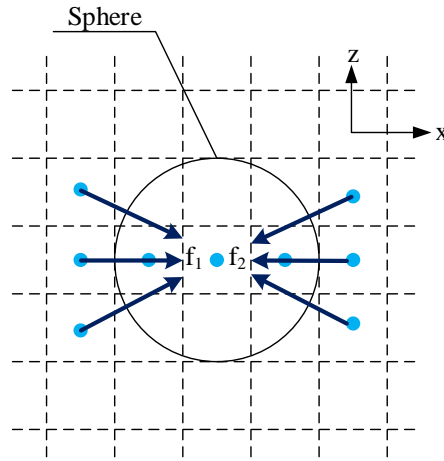
Figure 4.3. Integration of the pressure forces around a spherical particle along the x-direction

The collision forces (f_c) are modeled using an elastic spring-viscous dashpot system also known as Cundall and Strack's model presented by Tsuji et al. (1993). In this model, the collision forces are divided into two parts: i) Normal forces (f_n) and ii) Tangential forces (f_t). These forces are calculated using Equation 4.14 and 4.15.

$$f_n = -k_n d_n - \zeta_n v_n$$

$$f_t = -k_t d_t - \zeta_t v_t$$

In Equations 4.14 and 4.14, k is the elastic spring coefficient, ζ is the coefficient of viscous dashpot (damping coefficient), d is the particle displacements, and v is the particle velocity. The sub-index n and t are normal and tangential, respectively. These terms are usually calibrated in the numerical simulations. Besides, these

parameters can also be determined experimentally in idealized cases. For details of the experimental procedure, the reader is referred to (Norouzi et al., 2016).

4.2.2   Settings of the Numerical Model

The length, height, and width of the computational domain are determined as 18 m, 0.5 m, and 0.4 m presented in Figure 4.4. Although the width of the channel was 0.9 m in the physical model experiments, as the motion along the y-axis is not significant, it is taken shorter in the numerical simulations.
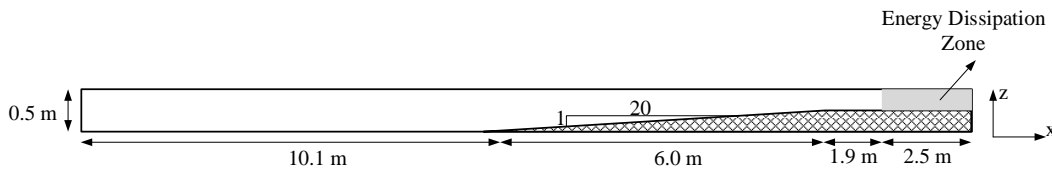
Figure 4.4. Side View of the Computational Domain

Grid Convergence Index (Roache, 1998) analysis described in Chapter 2 concluded that using 2 cm of grid size in all directions gives a solution independent from the grid resolution resulting in approximately one million cells. An energy dissipation zone (sponge layer) is placed at the end of the channel which as 2.5 m length. The solitary wave is generated using a theoretical water particle velocity and wave profile data based on Equation 4.1 and Equation 4.2, respectively. The velocity is assumed to be constant along the water column at the inlet. The k-ε turbulence model is activated in the simulations with default parameters.

4.3   Comparison of Physical Model Experiments and Numerical Modelling Studies

The DEM model parameters are calibrated, comparing the numerical and experimental results iteratively. The calibrated parameters are presented in Table 4.1.

Table 4.1 DEM Model Parameters

Spring Coefficient (k)		Viscous Dashpot Coefficient (ζ)	
Normal Direction	Tangential Direction	Normal Direction	Tangential Direction
$1*10^8$ N/m	$2.5*10^8$ N/m	$1*10^4$ kg/s	$2.5*10^3$ kg/s

The water surface elevations measured at five-wave gauges along the wave channel are compared to numerical results in Figure 4.5
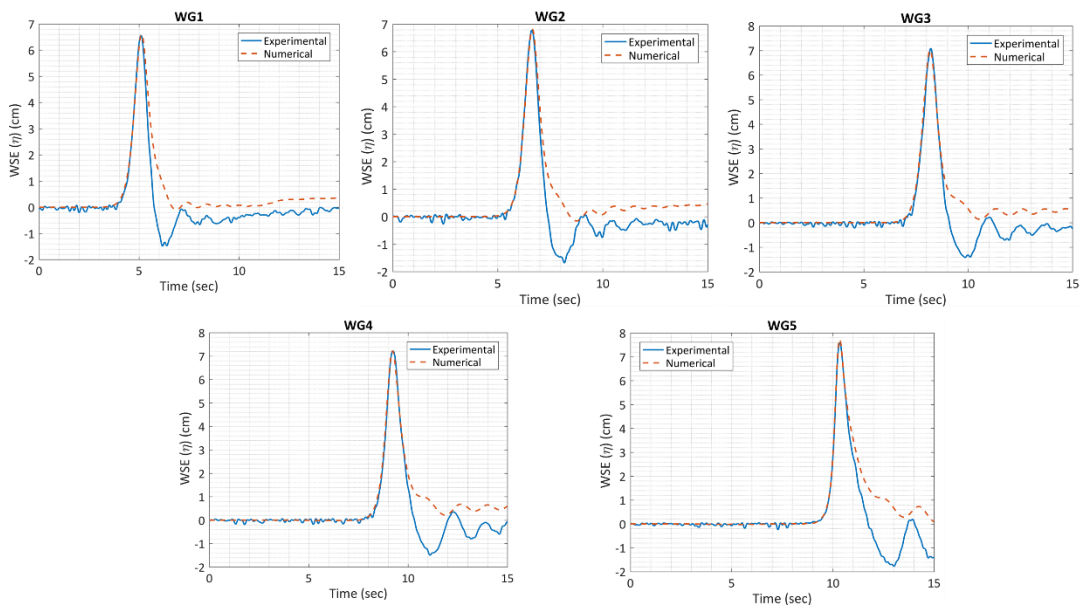
Figure 4.5. Comparison of water surface elevations: Numerical results (dashed orange lines), Experimental results (solid blue lines)

It is seen from Figure 4.5 that the experimental and numerical results are fairly in good agreement. However, there are slight deviations from the experimental measurements along the second half of the solitary waves. As the theoretical wave profile and water particle velocity data are used for the wave generation, these deviations are present between experimental and numerical results. As there are no water particle velocity data from these experiments, it cannot be used in the simulations.

The paths of the particles in x-direction measured in the experiments and computed by the numerical model are compared in Figure 4.6 for both the red and yellow spheres. In Figure 4.6, the five experimental trials are plotted as grey lines, and the numerical result is plotted as orange lines. In both experiments and numerical simulations, no collision is observed, and the breaking solitary wave pushed the yellow ball faster than the red ball; therefore, the distance in between the balls is increased. The results for y-direction are not presented as there is negligible motion along the y-axis in both physical model experiments and the numerical simulations. Several snapshots from the numerical simulations are also presented in Figure 4.7.
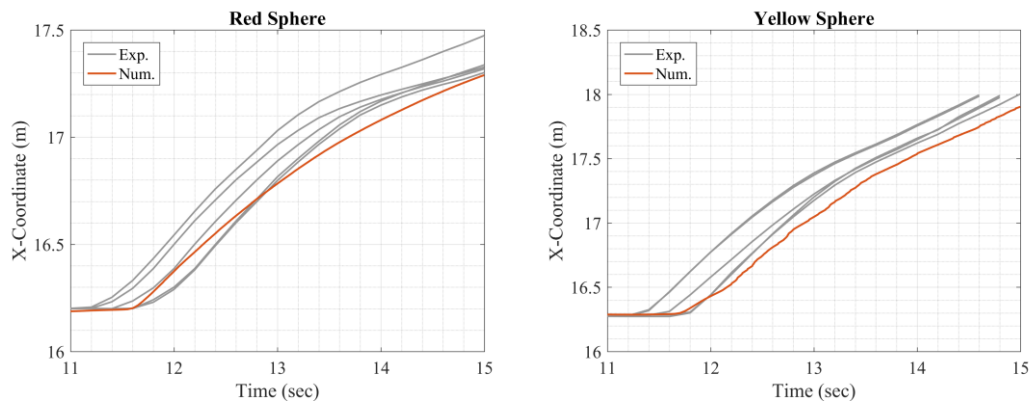
Figure 4.6. Comparison of the paths of the spheres in x-direction: Numerical results (orange lines), Experimental results (grey lines)

It is seen from Figure 4.6 that the numerical results and the experimental results are in good agreement with the numerical results especially for the red sphere. Although the path of the yellow sphere computed in the numerical simulations is similar to experimental measurements and acceptable in general for engineering applications considering the randomness in the experimental data, there is still an apparent difference for the yellow sphere. The possible reason for this situation is the coupling methodology in the present model. A resolving model might give better results as the flow field around the particles can be solved more accurately.
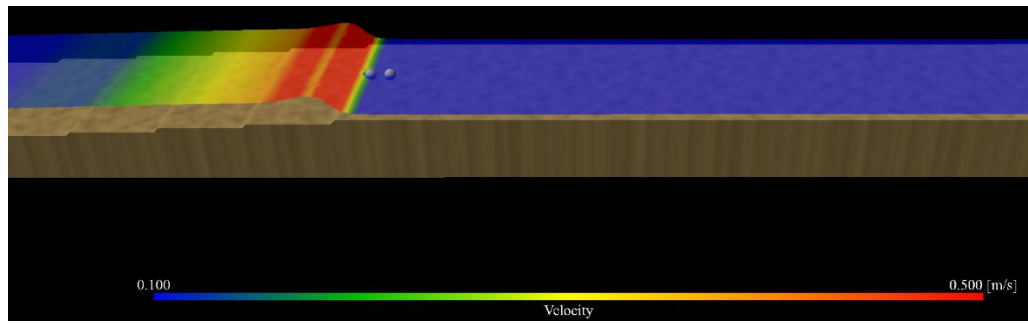
(a) t=11.55 sec
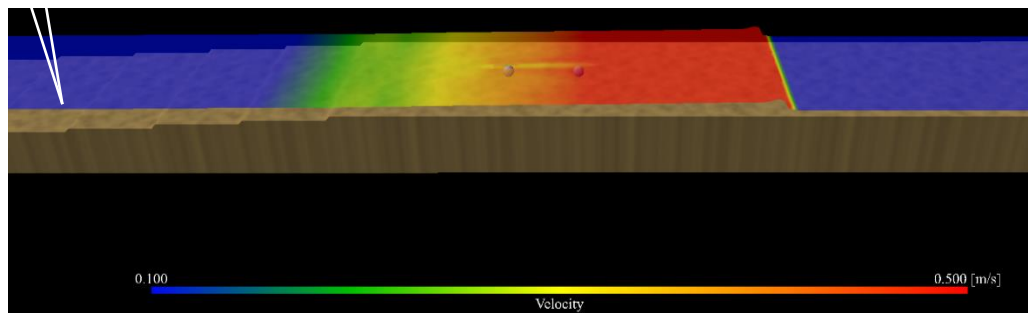
(b) t=13.33 sec

Figure 4.7. Snapshots from the numerical simulation

In Figure 4.7, it is seen that the solitary waves break on the particles. The magnitude of the velocity reaches 0.5 m/s as the wave passes over the spheres. Parallel to the experimental observations, the yellow ball moves faster than the red ball in the numerical simulations.

4.4   Concluding Remarks

In this chapter, an experimental and numerical study was carried out. It is seen from this study that the motion of spheres can be modeled with a non-resolving CFD-DEM numerical model with a certain degree of accuracy. A more accurate solution could be achieved with a resolving CFD-DEM solver. In the next chapter, the development of a CFD solver is described in detail that is based on the immersed boundary method, and that could be coupled with a DEM solver to obtain a resolving CFD-DEM numerical model.

The experiments presented in this chapter are within an introductory set of experiments, and it is the first time that the motion of spherical particles is investigated under wave attack. Therefore, there are many research questions remaining. As stated in Chapter 2, Goral et al. (2020) extended these experiments to find answers to these research questions.

CHAPTER 5

MODEL DEVELOPMENT

The strengths and weaknesses of the available CFD solvers are discussed in Chapters 3 and 4. In this section, the primary aim is to develop a CFD solver using the immersed boundary method (IBM). This solver would be strongly-coupled with a particle motion solver in future studies. Thus, the flow field around the particles can be resolved accurately.

The IBM is a numerical technique to represent solid boundaries (structures, bottom slopes, etc.) inside a computational domain. In the conventional method, the solid boundaries are removed from the computational mesh, which is referred to as body-conformal mesh configurations. On the other hand, the solid boundaries are either represented as body-force terms in the governing equations or the computational mesh around the solid boundary is modified locally in the immersed boundary methods. The former and latter IBMs are generally called as body-force IBM and cut-cell IBM, respectively. The IBMs make it easier to work with complex geometries and moving solid boundaries. In the present thesis study, firstly ibmPorFoam is established based on the body-force IBM for stationary boundaries as a starting point. After that, rubbleFoam is developed using the cut-cell IBM for moving boundaries as it is reported that the cut-cell IBM is a more robust technique when the moving boundaries are concerned (Udaykumar et al., 2001; Mittal and Iaccarino, 2005). Apparently, the cut-cell IBM is also applicable for stationary boundaries.

It is noted that both ibmPorFoam and rubbleFoam are capable of simulating porous media flow as the Volume-Averaged Reynolds-Averaged Navier-Stokes (VARANS) equations are solved in both models. Both solvers are also linked to the wave generating and absorbing boundary conditions given by Higuera et al. (2013).

In other words, both ibmPorFoam and rubbleFoam are developed modifying IHFOAM. Therefore, as details of the VARANS equations and wave generation and absorption boundary conditions are presented in Section 3.2.1, these aspects of the new solvers have not repeated again here in Chapter 5 unless there is a difference.

In this chapter, firstly, the OpenFOAM CFD library is briefly introduced. After that development of ibmPorFoam is described in detail. Different free-surface capturing algorithms used to apply the Volume of Fluid method are addressed in this section in relation to ibmPorFoam. Next, the development of rubbleFoam is presented. Finally, the chapter is completed with a brief summary of the capabilities of the numerical models stressing their novelties.

5.1 OpenFOAM CFD Library

OpenFOAM (stands for **Open**-source **F**ield **O**peration **A**nd **M**anipulation) is a library developed using C++ programming language for the computational fluid dynamics problems in general. There are three main distributions of OpenFOAM listed below:

- OpenFOAM distribution by OpenCFD Ltd. which is associated with ESI Group (referred to as ESI distribution in this study, released in www.openfoam.com)
- Foam-extend distribution by Wikki Ltd. (referred to as foam-extend in this study, released in www.foam-extend.org)
- OpenFOAM Foundation Inc. distribution by the OpenFOAM Foundation (referred to as OpenFOAM Foundation in this study, released in www.openfoam.org)

Although the main structure of these distributions are very similar, there are different group of libraries in each of them having various capabilities, and it is not straightforward to compile a CFD solver developed in one of these distributions with

another distribution as the numerical approaches, library structures, class and function names, etc. may differ.

In OpenFOAM, the differential equations (in particular Navier-Stokes equations) are solved using the finite volume method on collocated grids. OpenFOAM primarily consists of libraries and solvers. In the libraries, there are compulsory packages for the application of finite volume methods and optional packages for the use of specific numerical methods such as the immersed boundary method. Also, a variety of temporal and spatial discretization schemes, linear equation solvers, and turbulence models are available in addition to the standard boundary conditions such as atmosphere, wall, etc. implemented as sublibraries. On the other hand, there are many solvers focusing on the different types of CFD problems. These solvers are grouped according to the major assumptions. For example, the "incompressible group" of solvers focus on the incompressible flow, whereas the "multiphase group" of solvers works on the problems where there is an interface between two phases. These solvers call the libraries whenever required.

Although the structure of OpenFOAM is complex for "beginners," in general, the modular approach and dynamic linking capabilities of OpenFOAM make it easier to add different tools to your solver implemented by other researchers if you are aware of the capabilities and the limitations of the environment. For example, assume that there is a boundary condition that is implemented in OpenFOAM environment. If this boundary condition is theoretically compatible with your solver, you may add the capabilities of this boundary condition by adding a few lines to your input files and organizing related inputs for this boundary condition. Therefore, OpenFOAM is an efficient tool to solve CFD problems.

In the present study, ibmPorFoam is developed using the ESI distribution of OpenFOAM, and it is compiled with version 1706 (OpenFOAM, 2017). On the other hand, rubbleFoam is established based on the foam-extend distribution of OpenFOAM, and it is compiled with version 4.1 (foam-extend, 2020). Two different

distributions of OpenFOAM are used since the different sublibraries from each distribution are required.

Although different distributions are used, both ibmPorFoam and rubbleFoam are in the multiphase group of solvers. The basis solver of the multiphase group of solvers is interFoam. In other words, all other solvers in this group are developed modifying interFoam, including IHFOAM presented in Chapter 3. Reynolds-Averaged Navier-Stokes equations are solved in interFoam with a multiphase approach using the Pressure Implicit with Splitting Operator (PISO) algorithm (Issa, 1986). In the multiphase approach, the density and the molecular viscosity at each time step are updated according to the fraction of fluids (amount of the matter from each of the phases) in the computational cells along the interface between two different incompressible phases. The location of the interface is captured using the Volume of Fluid (VOF) method in interFoam. In the VOF method, the fraction of fluids at each computational cell is calculated solving the VOF-advection equation. In the present study, these incompressible phases are air and water, noting that air is assumed to be incompressible in this solution as the velocity and pressure field of air is not the focus. A detailed description of interFoam is given by Deshpande et al. (2012), and the performance of interFoam in simulating the surface waves is recently evaluated by Larsen et al. (2019).

5.2   Development of ibmPorFoam

As stated in the introduction of Chapter 5, ibmPorFoam is developed modifying IHFOAM solver described in Section 3.2. There are four major differences between these solvers:

- The porous media models are slightly different in these two models.
- In ibmPorFoam, the body-force immersed boundary method is used to represent stationary solid boundaries inside the computational domain whereas conventional body-fitted mesh configurations are used in IHFOAM.

- Although the VOF method is used to capture free-surface in both models, a recent algorithm called isoAdvector is also used in ibmPorFoam in addition to Multidimensional Universal Limiter with Explicit Solution (MULES) algorithm.
- A variant of ibmPorFoam is also established which is called ibmPorFoam-C. This variant is capable of include the effect of air compressibility.

A flowchart is given in Figure 5.1 summarizing the solution sequence and properties of ibmPorFoam. The equations related to the items in the flowchart are described within the following sub-sections in relation to the abovementioned items.
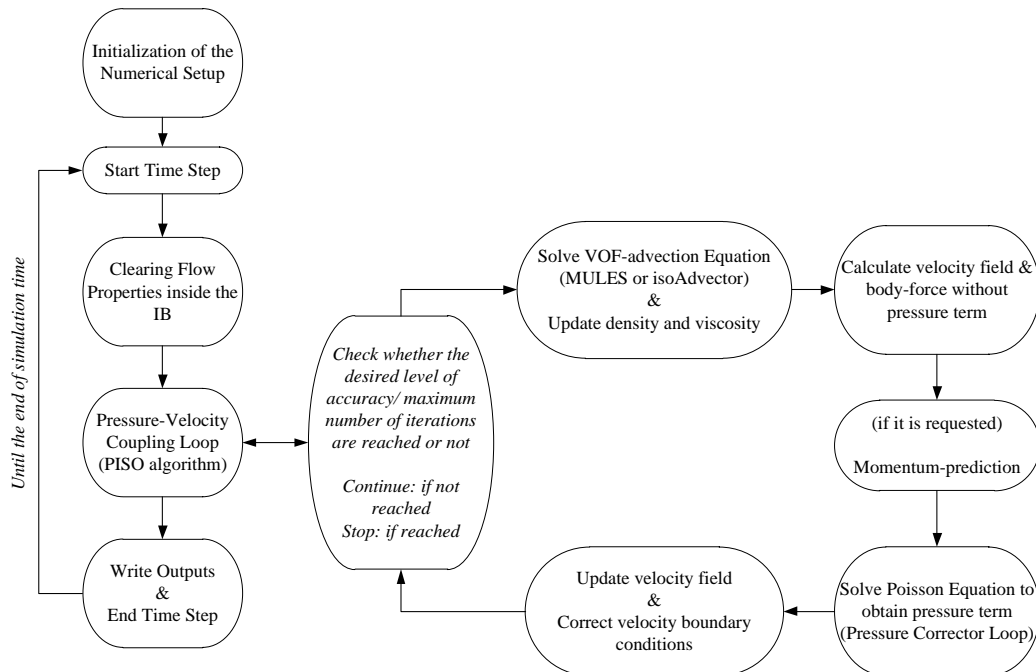
Figure 5.1. The structure of ibmPorFoam

In Figure 5.1, it is shown that the numerical setup is initialized first. In this step, the basic parameters required to start the simulations such as categories of the cells (see Section 5.2.2), initial time step, porous media coefficients, etc., are read from the related input documents. At each time step, the flow properties inside the IB is cleared. This is required as the unrealistic values around the IB may cause penetration of flow inside the IB. In the pressure-velocity coupling loop, the

VARANS equations are solved using the PISO algorithm. In this loop, first, the VOF-advection equation is solved using the selected algorithm, MULES or isoAdvector, and the density and viscosity fields are updated. Then, the velocity field and the body force are calculated without pressure term. If the momentum prediction is requested in the inputs, then the momentum equation is solved with the use of pressure field from the previous time step to achieve an intermediate velocity field. If not, one can continue the velocity field from the previous time step. After that, mass fluxes at the cell face are calculated with either predicted intermediate velocity field or the velocity field from the previous time step. Then, Poisson's equation is solved using the mass fluxes. As the Poisson's equation is solved, the pressure field is obtained for the present time step. This pressure field is used to correct the velocity field. Finally, the boundary conditions are corrected to finish the pressure-velocity coupling loop. When the desired accuracy level or the maximum number of iterations is reached, the loop is finished. The related outputs for the present timesteps are written, and the next time step starts until the end of the simulation.

5.2.1   The Difference in the Porous Media Models of ibmPorFoam and IHFOAM

In order to present the difference in the porous media models, Equation 3.4 is given again by in Equation 5.1, which is the volume-averaged momentum equation.

$$\frac{(1+C)}{n}\frac{\partial\rho\langle u_i\rangle}{\partial t} + \frac{1}{n}\frac{\partial}{\partial x_j}\left(\frac{\rho\langle u_i\rangle\langle u_j\rangle}{n}\right) =$$
$$-\frac{\partial\langle p\rangle^f}{\partial x_i} + \rho g_i + \frac{1}{n}\frac{\partial}{\partial x_j}\left(\mu_{eff}\frac{\partial\langle u_i\rangle}{\partial x_j}\right) - A\frac{\langle u_i\rangle}{n} - B\langle u_i\rangle\frac{\sqrt{\langle u_j\rangle\langle u_j\rangle}}{n}$$

Eq. 5.1

Higuera (2015) states that the closure parameters A and B are implemented in IHFOAM in a form given by Burcharth and Andersen (1995). In ibmPorFoam, the formulations given by van Gent (1995) are used. The difference in these closure

parameters is limited to the closure parameter *A* given by Equation 5.2 and Equation 5.3 for IHFOAM and ibmPorFoam, respectively.

$$A_{IHFOAM} = a \frac{(1-n)^3}{n^2} \frac{\mu}{D_{n50}^2}$$

Eq. 5.2

$$A_{ibmPorFoam} = a \frac{(1-n)^2}{n^2} \frac{\mu}{D_{n50}^2}$$

Eq. 5.3

It can be followed from these equations that A_{IHFOAM} and $A_{ibmPorFoam}$ are different by a factor of *(1-n)*. Other closure parameter *B* is the same in both models. The reason for this change is to correctly implement the closure parameters in ibmPorFoam, as it is recognized that the implementation of this parameter is not correct in IHFOAM. In the original references, both Burcharth and Andersen (1995) and van Gent et al. (1995) gave the closure parameter *A* as given in Equation 5.3. Also, Losada et al. (2016), which is a comprehensive literature review on the modelling of wave-porous structure interaction, presented this closure parameter as given in the original references. There might be an inherited error in IHFOAM. However, this issue does not violate any of the discussions given in the related studies including Chapter 3, since the linear friction parameter *a* is calibrated even if there is an error in the whole closure term *A*. In other words, the error is somehow corrected as the calibration parameter is a multiplier in the closure term *A*.

5.2.2   Implementation of the Body-Force Immersed Boundary Method

The body-force IBM used in the present study is previously given by Liu (2013, 2014), and further developed by Jensen (2014) and applied in Jensen et al. (2017). The momentum equation given by Equation 5.1 is modified to impose the solid boundaries (immersed boundaries). The continuity equation is left as it is in IHFOAM given by Equation 3.3 as no change is required. On the other hand, the momentum equation is modified as presented in Equation 5.4.

$$\frac{(1+C)}{n}\left(\frac{\rho^{k+1}\langle u_i\rangle^{k+1}-\rho^k\langle u_i\rangle^k}{\Delta t}\right)+\frac{1}{n}\frac{\partial}{\partial x_j}\left(\frac{\rho^k\langle u_i\rangle^k\langle u_j\rangle^k}{n}\right)=\left(-\frac{\partial\langle p\rangle^f}{\partial x_i}\right)^k$$

$$+\rho^k g_i+\frac{1}{n}\frac{\partial}{\partial x_j}\left(\mu_{eff}\frac{\partial\langle u_i\rangle^k}{\partial x_j}\right)-A\frac{\langle u_i\rangle^k}{n}-B\langle u_i\rangle\frac{\sqrt{\langle u_j\rangle^k\langle u_j\rangle^k}}{n}+F_i^k$$

Eq. 5.4

In Equation 5.4 Δt is the time step size and F_i is the body-force. The superscripts k and $k+1$ are denoting the present and next time steps, respectively, for a first-order temporal discretization of the momentum equation. The body force is defined by Equation 5.5.

$$F_i^k=\gamma\left[\frac{(1+C)}{n}\left(\frac{\rho^{k+1}U_{des}-\rho^k\langle u_i\rangle^k}{\Delta t}\right)+\frac{1}{n}\frac{\partial}{\partial x_j}\left(\frac{\rho^k\langle u_i\rangle^k\langle u_j\rangle^k}{n}\right)\right.$$

$$\left.\left(\frac{\partial\langle p\rangle^f}{\partial x_i}\right)^k-\rho^k g_i-\frac{1}{n}\frac{\partial}{\partial x_j}\left(\mu_{eff}\frac{\partial\langle u_i\rangle^k}{\partial x_j}\right)+A\frac{\langle u_i\rangle^k}{n}+B\langle u_i\rangle\frac{\sqrt{\langle u_j\rangle^k\langle u_j\rangle^k}}{n}\right]$$

Eq. 5.5

In Equation 5.5, U_{des} is the desired velocity field and γ is a cell marker taking a value of 1 inside an immersed boundary (IB) whereas it is 0 outside an IB. Thus, Equation 5.5 imposes the desired velocity field using the body force term inside the IBs. Note that the density at the next time step (ρ^{k+1}) is updated at the liquid-gas interface based on the VOF formulation discussed in Section 5.2.3.

In the present IBM, the desired velocity field is computed for the no-slip boundary condition assumption on the IB. To achieve this, cells inside the computational domain divided into groups according to their position concerning the IB using a previously implemented IBM library that uses ghost-cell algorithm (Jasak et al., 2014). This IBM library is presented in foam-extend distribution version 4.0. In the present study, it is compiled with ESI distribution of OpenFOAM version 1706 after appropriate modifications. In this framework of IBM, the geometric representation of IB is usually a 2D manifold for 3D simulation. If the cell center of any cell is

inside the IB, it is called an inside cell whereas the remaining cells are fluid cells. The inside cells are also divided into two groups. If the center of any cell is inside the IB and it has at least one neighbor fluid cell, this cell is called a ghost-cell. On the other hand, if an inside cell does not have any neighbor fluid cells, it is called a solid cell. The cell classification procedure is indeed representing the geometry of the IB. Additional mesh refinement is often performed along the boundary of the solid to represent the geometry of the IB more smoothly. After the cells are classified, the perpendicular distances (d) from the cell centers of the ghost cells to the IB are computed. Then, the ghost cells are mirrored along this perpendicular line to the fluid region to find the image points corresponding to each ghost cell. In other words, points in the fluid region having the shortest distance of 2d to the center of ghost cells are determined as image points. Either these image points can be cell centers of the neighbor fluid cells, or they can be any other point inside the fluid cell. Velocity vectors at the image points are computed using the velocity information at the surrounding fluid cells by interpolation in a selected neighborhood. Finally, the directions of the velocity vectors at the image points are reversed to find the velocity vector at each ghost cell. As the distance between the center of ghost cell and the IB is equal to the distance between the image point and the IB, the no-slip boundary condition is satisfied on the IB surface; thus, the desired velocity field is computed. A sketch showing the classification of the cells, and interpolation of the velocity vector to an image point is given in Figure 5.2.
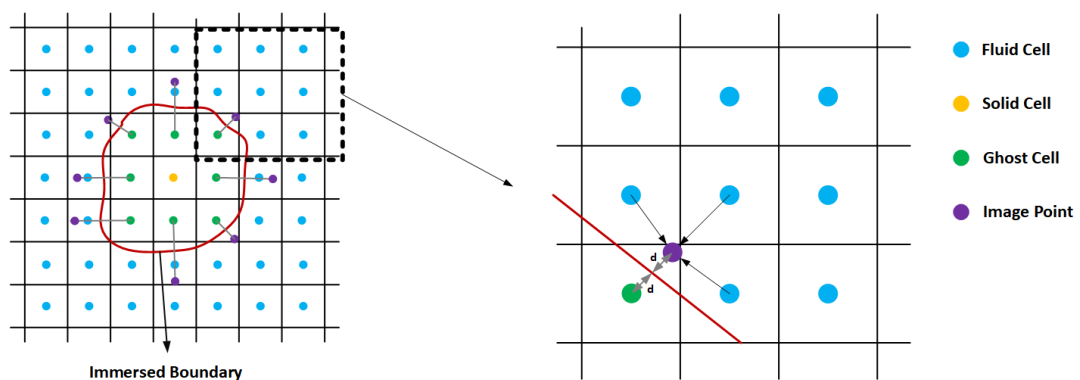
Figure 5.2. Classification of the cells for body-force immersed boundary method using ghost-cell algorithm and interpolation of the velocity vector to an image point

The interpolation schemes used to determine the velocity vector at the image points directly affect the accuracy of the IBM (Nasr-Azadani and Meiburg, 2011; Jensen, 2014). In the present study, Shepard interpolation scheme is used to find the velocity at the image points ($U_{IP,i}$) given by Equation 5.6 which is a particular case of the radial basis functions (Press et al., 1990; Buhmann, 2003).

$$U_{IP,i} = \frac{\sum_{j=0}^{N-1} u_j \left| x - x_j \right|^{-m}}{\sum_{j=0}^{N-1} \left| x - x_j \right|^{-m}} \qquad \text{Eq. 5.6}$$

In Equation 5.6, N is the number of interpolation cells, u_j is the velocity at the j_{th} interpolation cell, $\left| x - x_j \right|$ is the radial distance, and m is a constant that is selected between 1 and 3.

5.2.2.1   Turbulence Modelling

As stated in Chapter 3, turbulence modelling is generic in OpenFOAM where two-equation models in the framework of RANS equations or Large Eddy Simulations (LES) can be applied directly. In the scope of the present numerical solver, relation of turbulence modelling with the porous media modelling and body-force IBM are the two items to be clarified. Away from the porous media and the immersed boundaries, the generic turbulence modelling in OpenFOAM can be used.

For porous media modelling, there are volume averaged versions of several two-equation models (del Jesus et al., 2012; Higuera et al. 2014a), and there are LES based porous media models (Wu et al., 2014). Furthermore, Jensen et al. (2014) discussed that there is no need for a turbulence model in the presence of porous media if the main research question is not related to turbulence since the effect of turbulence is already included in the calibrated resistance coefficients based on experimental data.

For body-force IBM, the difficulty is to implement wall functions as the wall surface is implicit (Liu, 2013). Therefore, the present model might have accuracy issues to resolve the boundary layer around the immersed boundaries accurate enough for research problems such as sediment transport and scouring, where the effect of the boundary layer becomes vital. However, as the focus of the established numerical model and the validation studies is wave-structure interaction in larger scales, there are no significant accuracy problems in the results of validation cases presented in Chapter 6.

5.2.3   Free-Surface Capturing using the VOF Method in ibmPorFoam

The VOF methodology is partly discussed in Section 3.2.1. The discussions are extended here; however, several equations are repeated for the completeness of this section. In the VOF method, an indicator function (α) is defined at each cell in the computational domain. This function takes a value of 1 when the cell is full of liquid; on the other hand, it takes a value of 0 when the cell is empty, i.e., full of gas. An additional equation referred to as the VOF-advection equation derived from the continuity equation is solved to employ the VOF method given by Equation 5.7.

$$\frac{\partial \alpha}{\partial t} + \frac{\partial \alpha u_i}{\partial x_i} = 0 \qquad\qquad \text{Eq. 5.7}$$

According to the variation of the VOF function, density and molecular viscosity are updated at those cells at the gas and liquid interface by the relations given by Equation 5.8 and Equation 5.9, respectively.

$$\rho = \alpha \rho_l + \left(1-\alpha\right)\rho_g \qquad\qquad \text{Eq. 5.8}$$

$$\mu = \alpha \mu_l + \left(1-\alpha\right)\mu_g \qquad\qquad \text{Eq. 5.9}$$

where l stands for liquid and g stands for the gas phase.

There are two available VOF algorithms called Multidimensional Universal Limiter Explicit Solver (MULES) and isoAdvector in OpenFOAM ESI distribution. MULES

and isoAdvector algorithms are used in OpenFOAM multiphase flow solvers interFoam and interIsoFoam, respectively. In interFoam, a modified version of Equation 5.7 is solved presented in Equation 5.10.

$$\frac{\partial \alpha}{\partial t} + \frac{\partial \alpha\, u_i}{\partial x_i} + \frac{\partial \alpha (1-\alpha) u_i^r}{\partial x_i} = 0$$ Eq. 5.10

where u_i^r is the compression or relative velocity given by Equation 5.11.

$$u_i^r = u_i^l - u_i^g$$ Eq. 5.11

where u_i^l is the velocity of the liquid phase and u_i^g is the velocity of the gas phase. Initially, the last term containing u_i^r is not available in the VOF advection equation. In interFoam, this additional convection term is included to provide a sharper interface in the solution (Berberovic et al., 2009). In the MULES scheme, a limiter factor is used to bound the value of the VOF function between 1 and 0. The reader is referred to Deshpande et al. (2012) for further details of the implementation of the MULES scheme. Equation 5.10 is volume averaged (Higuera et al., 2014a; Higuera, 2015) as given in Equation 5.12. The MULES scheme is modified to account for the porous media flow by Higuera et al. (2014a).

$$\frac{\partial \alpha}{\partial t} + \frac{1}{n}\frac{\partial \alpha \langle u_i \rangle}{\partial x_i} + \frac{1}{n}\frac{\partial \alpha (1-\alpha) \langle u_i^r \rangle}{\partial x_i} = 0$$ Eq. 5.12

On the other hand, Equation 5.7 is solved in interIsoFoam using isoAdvector algorithm developed by Roenby et al. (2016). isoAdvector is a geometric scheme, but it is applicable to general meshes. It works in two steps namely interface reconstruction and advection. The interface position and orientation in the intersected cells are calculated using iso-surfaces. In the advection step, the face-interface intersection line is computed sweeping a mesh face during a time step. The boundedness of the resulting VOF function values between 1 and 0 is ensured following a redistribution and recalculation step. For the details of this scheme, the reader is referred to Roenby et al. (2016). Equation 5.7 is volume-averaged by

Higuera (2015) given in Equation 5.13. In the present study, the isoAdvector algorithm implementation is modified to correctly represent flow through porous medium. Simply, the effect of the porosity is reflected in the convection term in Equation 5.7 based on Equation 5.13.

$$\frac{\partial \alpha}{\partial t} + \frac{1}{n}\frac{\partial \alpha \langle u_i \rangle}{\partial x_i} = 0 \qquad \text{Eq. 5.13}$$

In ibmPorFoam, the free surface capturing is optional. When the MULES scheme is selected, Equation 5.12 is solved using this scheme in the same way as IHFOAM. When the isoAdvector scheme is selected, Equation 5.13 is solved in a geometric manner using the modified version of this scheme. Basically, the same framework with interIsoFoam is used; however, the effect of porosity is included in the momentum equations and the isoAdvector scheme.

Another issue that must be addressed is the relation of free-surface capturing and immersed boundary methods. In free surface capturing, there are different approaches to treat immersed boundaries. One way is to add a source term to the VOF advection equation similar to the body-force added to the momentum equation to impose the IB (e.g.: Jensen et al., 2017). The second approach is to solve the VOF advection equation without modifying (e.g.: Shen and Chan, 2008; Liu, 2013, 2014). In this study, the second approach is implemented; therefore, the same VOF advection equations are solved to capture the free surface using MULES and isoAdvector schemes given by Equation 5.12 and Equation 5.13, respectively, while applying the IBM with a source term in the momentum equation.

5.2.4   Inclusion of the Air Compressibility Term

In engineering applications, the effect of air compressibility becomes more important, as an accurate prediction of the impact pressures may depend on the compression of trapped air. Air compressibility term is included in ibmPorFoam based on the equations given by Arikawa et al. (2007), and this new variant of

ibmPorFoam is called as ibmPorFoam-C. The modified continuity and momentum equations solved in ibmPorFoam-C are given by Equation 5.14 and 5.15, respectively.

$$\frac{\partial \langle u_i \rangle}{\partial x_i} = -\frac{(1-\alpha)}{\rho_G} \hat{\rho}_G$$

Eq. 5.14

$$\frac{(1+C)}{n} \frac{\partial \rho \langle u_i \rangle}{\partial t} + \frac{1}{n} \frac{\partial}{\partial x_j} \left(\frac{\rho \langle u_i \rangle \langle u_j \rangle}{n} \right) = -\frac{\partial \langle p \rangle^f}{\partial x_i} + \rho g_i +$$

$$\frac{1}{n} \frac{\partial}{\partial x_j} \left(\mu_{eff} \frac{\partial \langle u_i \rangle}{\partial x_j} \right) - A \frac{\langle u_i \rangle}{n} - B \langle u_i \rangle \frac{\sqrt{\langle u_j \rangle \langle u_j \rangle}}{n} + F_i - \langle u_i \rangle \frac{(1-\alpha)}{\rho_G} \hat{\rho}_G$$

Eq. 5.15

In Equation 5.14 and 5.15, ρ_G is the density of air and $\hat{\rho}_G$ is the material derivative of the air density given by Equation 5.16.

$$\hat{\rho}_G = \frac{\partial \rho_G}{\partial t} + \frac{\langle u_i \rangle}{n} \frac{\partial \rho_G}{\partial x_i}$$

Eq. 5.16

The terms included in the continuity and momentum equations related to the air compressibility depends on the value of VOF function (α). In other words, these terms are activated at the interface between the air and liquid phase, and in the full air phase.

The density field is calculated using Equation 5.17:

$$\rho_G = \frac{p + p_0}{R_{gas} \, T_{emp}}$$

Eq. 5.17

In Equation 5.17, p is pressure, p_0 is the reference atmospheric pressure, R_{gas} is gas constant and T_{emp} is temperature. Different from the fully compressible equations, the temperature is considered as constant throughout the simulation.

5.3   Development of rubbleFoam

As stated in the introduction of Chapter 5, rubbleFoam is developed modifying
IHFOAM solver described in Section 3.2. There are three major differences between
rubbleFoam and IHFOAM. These differences are itemized below in comparison with
ibmPorFoam.

- The porous media models are slightly different in these two models. In
  rubbleFoam, the porous media parameters are the same as ibmPorFoam. This
  issue and the differences between ibmPorFoam and IHFOAM are discussed
  in Section 5.2.1.
- In rubbleFoam, the cut-cell immersed boundary method (IBM) is used to
  represent stationary and moving solid boundaries inside the computational
  domain. In ibmPorFoam, the body-force IBM is used to represent stationary
  solid boundaries, whereas the conventional body-fitted mesh configurations
  are used in IHFOAM.
- The VOF method is used to capture free-surface in all models. In IHFOAM,
  MULES algorithm is used, whereas both MULES and isoAdvector
  algorithms are used in ibmPorFoam. In rubbleFoam, the VOF-advection
  equation is solved using standard linear solvers available in OpenFOAM
  CFD library.

A flowchart is given in Figure 5.3, summarizing the solution sequence and properties
of rubbleFoam. The methodologies related to the items in the flowchart are described
within the following sub-sections in relation to the abovementioned items.
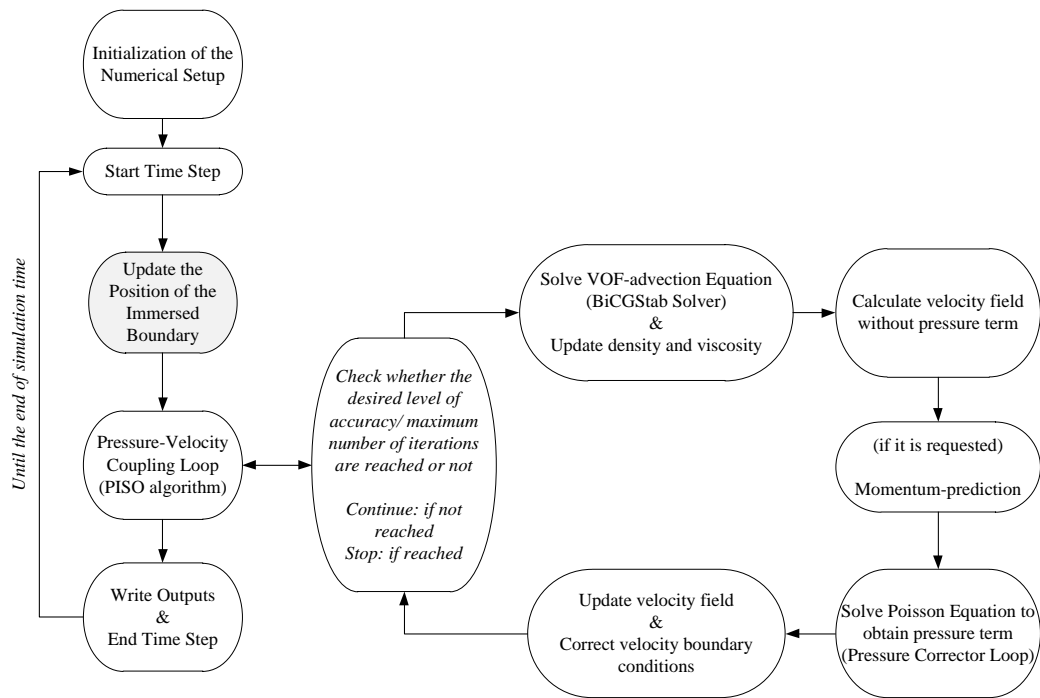
Figure 5.3. The structure of rubbleFoam

In Figure 5.3, the different part from ibmPorFoam is colored with grey. Other than the grey box, same algorithm described for ibmPorFoam at the beginning of Section 5.2 is followed; therefore, it is not repeated here once again. In the step indicated by grey color, the position of the IB is updated according to the inputted path of the IB. This path could be defined as a function or it could be directly given to the code. As the position of the IB is updated, the cells are cut, reorganized and the Space Conservation Law is applied. The cells that are free from the IB at the present time step are converted to regular cells.

5.3.1   Implementation of Cut-Cell Immersed Boundary Method

The cut-cell immersed boundary method has recently been implemented in the foam-extend version 4.1 (Jasak, 2018). The capabilities of this library are used to improve IHFOAM to obtain rubbleFoam. The equations solved in rubbleFoam are the original VARANS equations given by Equations 3.3 and 3.4. There is no modification in these equations similar to the modification in ibmPorFoam; however, the motion of

solid boundaries is reflected in the solution with a methodology called Moving Mesh Finite Volume Method described by Ferziger and Peric (2002). This methodology is explained later in this section.

In the cut-cell IBM, the computational cells are cut by the boundary of the solid particles. Cell volume, face area and cell center of the affected cells are recalculated. The schematic representation of the cut-cell IBM is given in Figure 5.4.
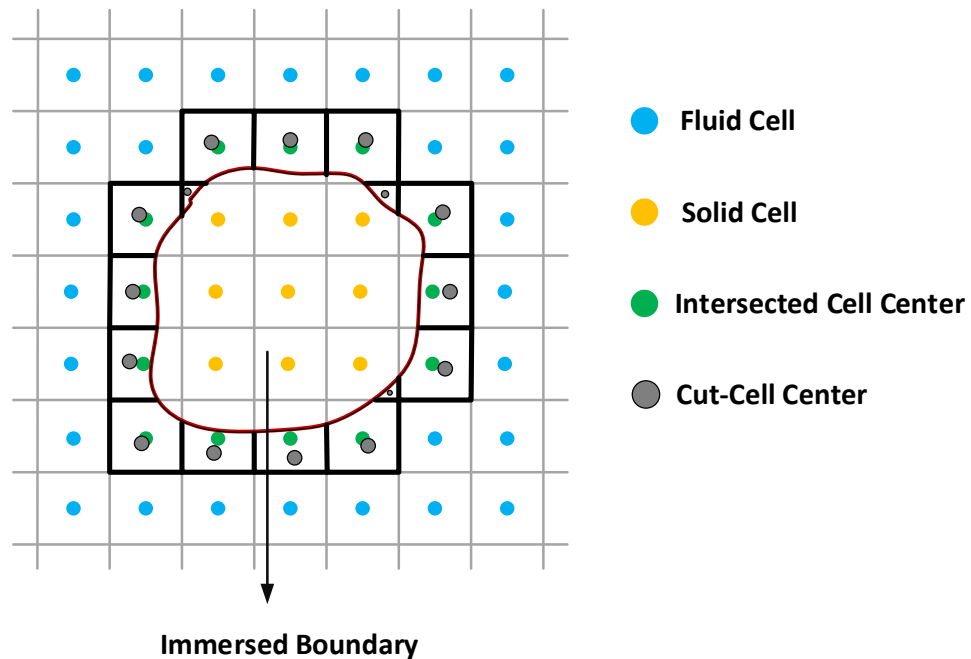
Figure 5.4. Schematic representation of the cut-cell immersed boundary method

In Figure 5.4, it is shown that the computational cells are divided into two groups according to their position: i) Fluid cells that are not affected ii) Intersected cells which are cut by the immersed boundary. Intersected cells are divided into new cells. The cells staying inside the IB are called as solid cells. The new centers of the intersected cells outside the IB are also shown in Figure 5.4. The change in the cells are schematized Figure 5.5 as the boundary moves.
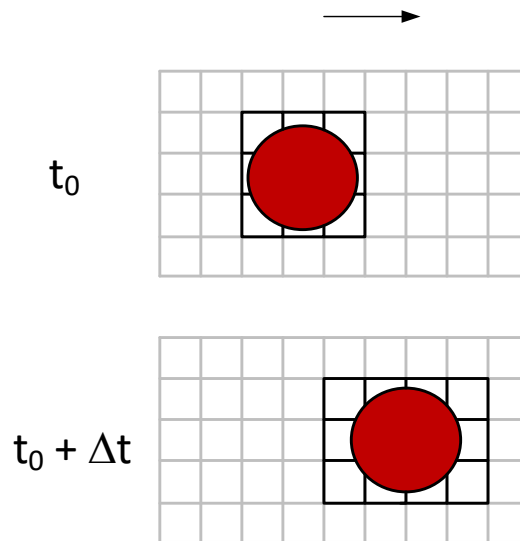
Figure 5.5. Change in the mesh configuration as the immersed boundary moves

For the moving boundaries, the computations are performed on the new mesh configuration in the same way as the conventional body-fitted finite volume method at each time step. Therefore, the accuracy of the computation is theoretically the same as conventional methods. As the IB moves, the computational cells are updated as shown in Figure 5.5.

It should be stressed that a totally new mesh configuration is not generated in the present cut-cell IBM. As it is pointed out by Mittal and Iaccarino (2005), regeneration of the mesh configuration at each time step has a negative impact on the accuracy, robustness and computational cost of the numerical modelling. Furthermore, it requires a procedure to conform the computations on the new computational domain (Tezduyar, 2001). In the present cut-cell IBM, the mesh configuration is locally modified, and the effect of motion is represented in the governing equations using Moving Mesh Finite Volume Method (MMFVM).

In order to describe MMFVM (Ferziger and Peric, 2002), the integral form of the mass conservation and momentum conservation (i^{th} component) equations given by Equations 5.18 and 5.19, respectively, are used:

$$\frac{\partial}{\partial t} \int_{CV} \rho d\Omega + \int_{CS} \rho(\vec{v} - \vec{v}_b) \cdot \vec{n} \, dY = 0 \qquad \text{Eq. 5.18}$$

$$\frac{\partial}{\partial t} \int_{CV} \rho u_i d\Omega + \int_{CS} \rho u_i (\vec{v} - \vec{v}_b) \cdot \vec{n} \, dY = \int_{CS} (\tau_{ij}\vec{j} - p\vec{i}) \cdot \vec{n} \, dY + \int_{CV} b_i d\Omega \qquad \text{Eq. 5.19}$$

In Equations 5.18 and 5.19, t is time; ρ is density of fluid; $\vec{v}$ is velocity vector of fluid particles; $\vec{v}_b$ is the velocity vector of moving immersed boundary; $\vec{n}$ is normal vector; u_i is the ith component of the velocity vector; τ_{ij} is stress tensor; p is pressure; b_i is the body force; $\vec{i}$ and $\vec{j}$ are unit vectors in ith and jth directions, respectively; CV stands for the control volume; CS stands for the control surface; Ω is volume and Y is surface. The only change in these conservation equations is the appearance of the relative velocity $(\vec{v} - \vec{v}_b)$ in the convective terms.

In sequential solution methods like PISO that is used to solve governing equations in rubbleFoam, the mass fluxes are treated as known in all other conservation equations except for the continuity equation. Therefore, other equations may be treated as they are being solved on a stationary grid. Special attention must be given on the continuity equation given by Equation 5.18.

In incompressible flows, the contribution of the grid movement to the mass fluxes must cancel the unsteady term. In other words, the following equation must be satisfied; otherwise, the continuity equation is not satisfied, and artificial mass sources are produced in the solution as a result.

$$\frac{\partial}{\partial t} \int_{CV} \rho d\Omega = -\int_{CS} \rho(\vec{v} - \vec{v}_b) \cdot \vec{n} \, dY \qquad \text{Eq. 5.20}$$

Equation 5.20 can be written in the limit of zero fluid velocity as given by Equation 5.21. This equation is known as "Space Conservation Law".

$$\frac{\partial}{\partial t} \int_{CV} d\Omega = \int_{CS} \vec{v}_b \cdot \vec{n} \, dY \qquad \text{Eq. 5.21}$$

By the Space Conservation Law, the total volume is conserved when the control volume changes its shape and/or its position. Therefore, Space Conservation Law guarantees the accuracy of the solution in the case of cut-cell IBM as the cell shapes change.

A first-order temporal discretization of Equation 5.21 can be written as given by Equation 5.22.

$$\frac{(\Delta\Omega)^{k+1} - (\Delta\Omega)^{k}}{\Delta t} = \sum_{c} (\vec{v}_b \cdot \vec{n})_c \, dY \qquad \text{Eq. 5.22}$$

In Equation 5.22, $k+1$ and k stand for next and present timesteps, and c stands for the cell face. This equation shows that the difference between the volumes is the summation of the swept volumes by the cell faces that can be written as follows:

$$\frac{(\Delta\Omega)^{k+1} - (\Delta\Omega)^{k}}{\Delta t} = \frac{\sum_{c} \delta\Omega_c}{\Delta t} \qquad \text{Eq. 5.23}$$

Space Conservation Law is applied to assure the conservation of mass when the mass fluxes are calculated. The calculation of the mass fluxes is carried out as given in Equation 5.24 for any cell face "c" having a surface area of S_c.

$$\int_{S_c} \rho(\vec{v} - \vec{v}_b) \cdot \vec{n} \, dY \approx \rho_c (\vec{v} \cdot \vec{n}) Y_c - \rho_c (\vec{v}_b \cdot \vec{n}) Y_c = \rho_c (\vec{v} \cdot \vec{n}) Y_c - \rho_c \frac{\delta\Omega_c}{\Delta t} \qquad \text{Eq. 5.24}$$

Thus, the effect of the swept volumes due to the motion of the immersed boundary is distributed to the related cells.

5.3.1.1   Turbulence Modelling

The discussions on the turbulence modelling given in Section 5.2.2.1 are valid for rubbleFoam in the scope of the generic turbulence modelling in OpenFOAM and the turbulence modelling inside the porous media.

On the other hand, the conditions are changed for the immersed boundary method applied in rubbleFoam. As the cells are cut according to the geometry of the IB, the location of the wall is well-known in each time step even if the solid boundary moves. Therefore, rubbleFoam is capable of resolving the boundary layer around the coastal structures.

5.3.2   Free-Surface Capturing using the VOF Method in rubbleFoam

Free-surface capturing in rubbleFoam is handled solving the VOF-advection equation as in the case of ibmPorFoam. Indeed, Equation 5.12 is solved in rubbleFoam. Although the VOF-advection equation is solved using either MULES algorithm or isoAdvector algorithm is ibmPorFoam, this equation is solved using a standard linear equation solver of OpenFOAM. In particular, Bi-Conjugate Gradient Stabilized (BiCGStab) method solver (van der Vorst, 1992) is found out to be the most robust methodology for the present solver.

MULES and isoAdvector algorithms cannot be used as artificial bubbles are formed around the moving boundary in the test cases. The reasons for this situation have not been clarified yet, and investigations on this issue are left as a future study.

5.4   Summary of the Capabilities of the Numerical Models

In this chapter, two CFD solvers are established, modifying IHFOAM presented in Chapter 3. Both models are capable of solving flow properties inside porous media in a computational domain, free-surface is captured using the VOF method with both

models, and these solvers are linked to the wave generation and absorption boundary conditions given by Higuera et al. (2013).

In ibmPorFoam, compiled with ESI distribution of OpenFOAM version 1706, the body-force immersed boundary method is applied to represent stationary solid boundaries in the computational domain. The VOF-advection equation is solved with either MULES or isoAdvector algorithms noting that it is the first time that isoAdvector algorithm is used with the immersed boundary method and within the porous medium. Furthermore, a variant of the ibmPorFoam is also established to account for the effect of air compressibility.

In rubbleFoam, compiled with foam-extend version 4.1, the cut-cell immersed boundary method is applied to represent stationary and moving boundaries in the computational domain. The VOF-advection equation is solved with a standard linear equation solver of OpenFOAM. To the author's knowledge, it is the first time that a numerical model that accounts for the moving boundaries, porous media flow and free-surface capturing.

Overall, ibmPorFoam is an initial step for the immersed boundary method. At the beginning of this chapter, it is aimed to develop a numerical model that resolves the flow properties around moving boundaries that could be coupled with a particle motion solver. This aim is achieved by establishing rubbleFoam, which is ready for coupling with a particle motion solver.

CHAPTER 6

MODEL VALIDATION

6.1   Validation of ibmPorFoam

ibmPorFoam is validated against four experimental datasets. These datasets are specially selected to present the capabilities of the numerical model that are the representation of the solid boundaries using the immersed boundary method. Furthermore, different wave-porous structure modelling approaches, that are macroscopic and microscopic porous media modelling approaches, are exemplified in the validation studies. All the validation cases are studied using ibmPorFoam solver with MULES and isoAdvector schemes in capturing the free surface separately. The numerical results of ibmPorFoam with MULES scheme and ibmPorFoam with isoAdvector scheme are referred to respectively as "ibmPorFoam (MULES)" and "ibmPorFoam (isoAdvector)" hereafter. Furthermore, all these cases are studied using IHFOAM, which also solves the VARANS equations on body-conformal mesh configurations. Note that both ibmPorFoam and IHFOAM are compiled with OpenFOAM ESI distribution version 1706.

The primary aim of these studies is apparently the validation of the numerical model. On the other hand, the secondary aim of these studies is to answer the following questions:

- What are the differences in representing impervious boundaries using body conformal mesh configurations and using IBM?
- Is isoAdvector scheme applicable in capturing free surface when the impervious boundaries are represented using IBM?

- Is the modification of isoAdvector scheme that is presented for macroscopic porous media flow modelling approach appropriate?
- What are the advantages and disadvantages of using IBM compared to body conformal mesh configurations when using microscopic porous media modelling approach?
- Does isoAdvector scheme improve the results in free surface capturing compared to MULES scheme when different types of waves are concerned rather than progressive waves?

Description of the validation cases is presented in Table 6.1 for ibmPorFoam stating the porous media modelling approach and solid boundary representation methodology.

Table 6.1 Description of the validation cases for ibmPorFoam

#	Case Name	Porous Media Modelling	Solid Boundary Representation
1	Interaction of Dam Break Flow with an Impervious Static Box (Kleefsman et al., 2005)	Not Available	A solid static box represented as an IB.
2	Interaction of Dam Break Flow with Porous Material (Lin, 1998)	Flow-through the porous material is modelled with the macroscopic porous media modelling approach.	Not Available
3	Solitary Wave Propagation over a Submerged Permeable Breakwater (Wu and Hsiao, 2013)	Porous media modelling with the macroscopic approach is not available. However, the microscopic porous media modelling approach is tested.	The permeable breakwater is represented as an IB.
4	Solitary Wave Attack on a Rubble Mound Breakwater (Chapter 3)	Porous layers of the breakwater are modelled with the macroscopic porous media modelling approach.	The crown-wall is represented as an IB.

6.1.1   Case 1: Interaction of Dam Break Flow with an Impervious Static Box

The present numerical model, ibmPorFoam, is firstly validated against the data from the physical model experiments studying 3D interaction of dam-break flow with an impervious static box (Kleefsman et al., 2005). This case is selected to validate ibmPorFoam, and compare the differences in between ibmPorFoam (MULES), ibmPorFoam (isoAdvector) and IHFOAM. The physical model experiments were conducted in a 3.22 m long, 1.00 wide and 1.00 m high wave tank. An impervious static box is placed inside the wave tank in addition to the dam. The water surface elevation is measured using four-wave gauges; however, data from two wave gauges (WG2 and WG4) is available. In Figure 6.1, details of the experimental configuration including dimensions and indicating the positions of the wave gauges are presented.
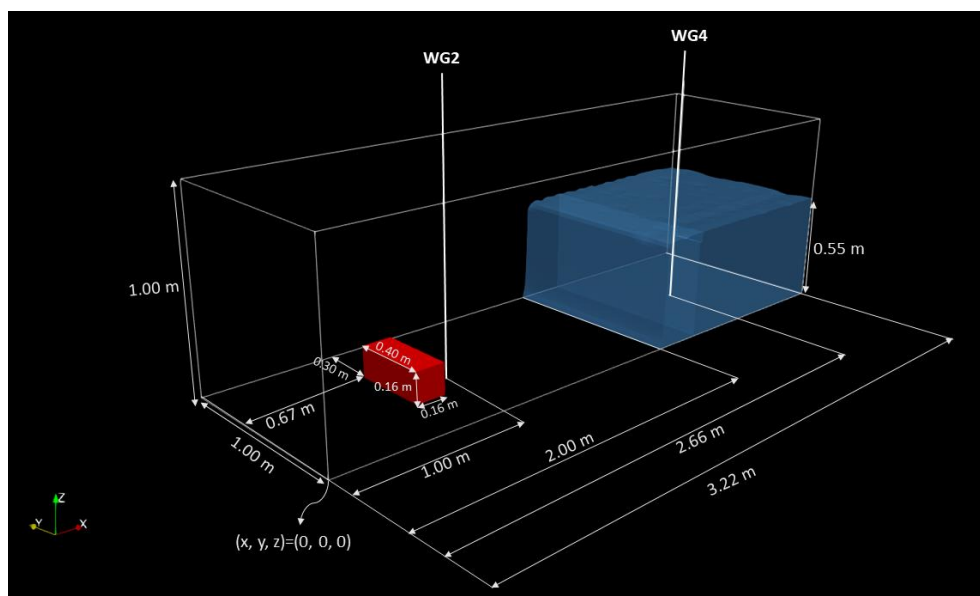
Figure 6.1. Experimental setup (Case 1)

Pressure on the face of the box that is closer to the water body, and at the top of the box are recorded with eight pressure gauges. In the present study, the available data from four pressure gauges (P1, P3, P5, and P7) are compared with the results from

the numerical simulations. The locations of the four pressure gauges are given in Table 6.2.

Table 6.2 Location of the pressure gauges

Gauge #	Coordinates*		
	X (m)	Y (m)	Z (m)
P1	0.830	0.474	0.025
P3	0.830	0.474	0.099
P5	0.806	0.526	0.160
P7	0.733	0.526	0.160
*Origin is indicated in Figure 6.1.			

The computational domain is constructed in the same way with the experimental setup for the simulations with ibmPorFoam. The mesh sizes along x, y and z-axes are uniformly selected as 2, 4 and 2 cm, respectively. The impervious static box is represented as an IB. Additional mesh refinement is applied around the box resulting in 1, 2 and 1 cm mesh sizes along x, y, and z-axes. This configuration reveals approximately 242000 cells in the computational domain for ibmPorFoam simulations. The maximum Grid Convergence Index (GCI) is found to be as 1.7% which is acceptable. All the faces except for the top one are defined as reflective walls; the top face is defined as the atmosphere boundary condition. No-slip boundary condition is applied along the IB. k-ω SST model is used as the turbulence closure in this case, and the simulation duration is kept as 2 seconds. A similar numerical setup is used for the simulation with IHFOAM. The only difference is the representation of the box. In IHFOAM simulation, the box is extracted from the computational domain revealing 221000 cells including the additional refinement around the extracted region. As the geometry of the box is regular, the extraction of the box from the computational domain is simple. However, it is still time-consuming compared to the mesh generation process for ibmPorFoam. Snapshots from the simulation with ibmPorFoam (MULES) are presented in Figure 6.2.
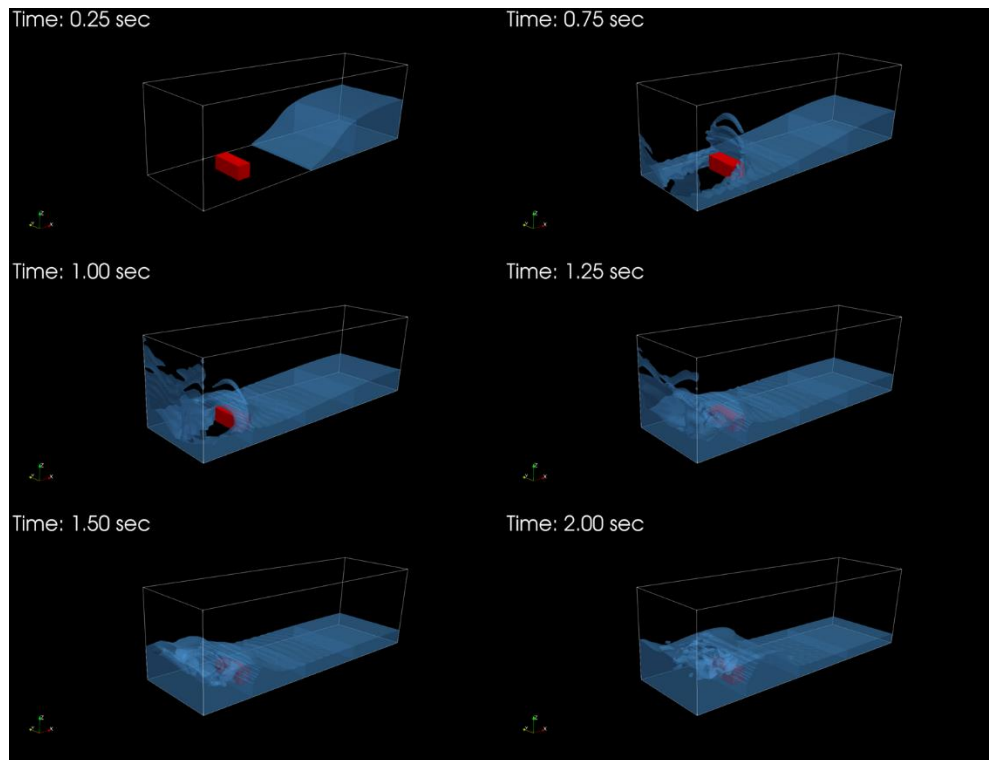
Figure 6.2. Snapshots from the simulation, ibmPorFoam (MULES)

In Figure 6.2, the motion of the dam break flow is observed. As the water body approaches to the box, the water level is smooth until it hits the box. The violent impact and the splashing of the waves are observed after that. In Figure 6.3, the comparison of the numerical results with the experimental results at the wave gauges is presented.
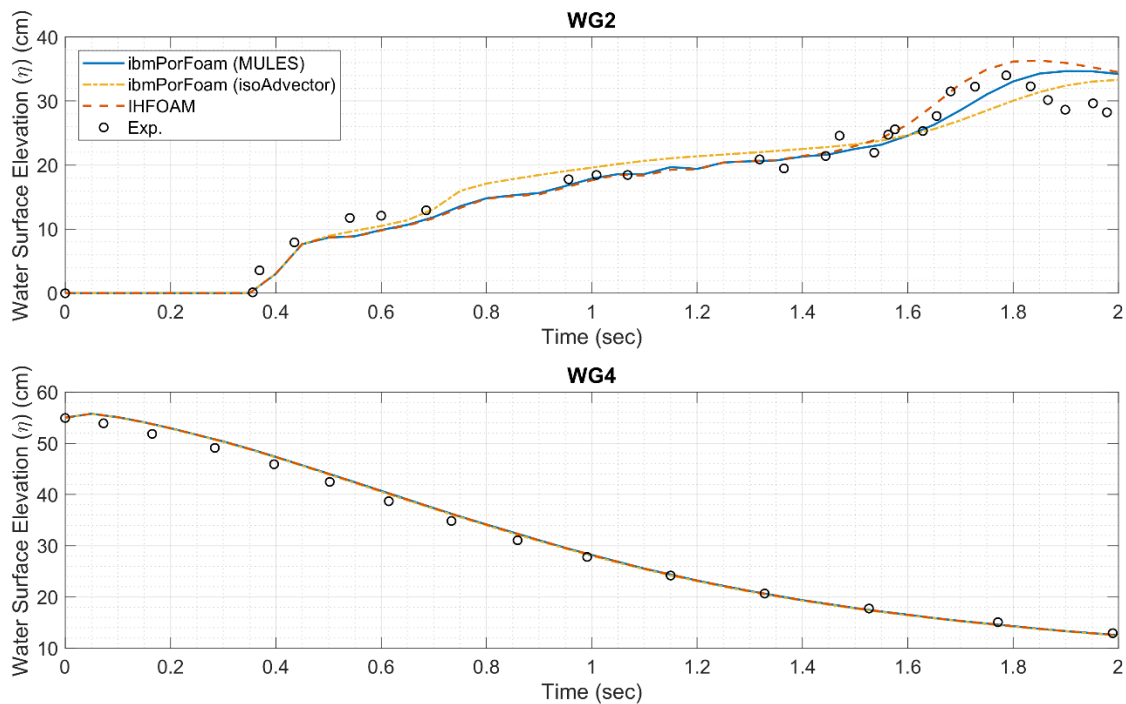
Figure 6.3. Comparison of water surface elevations of the numerical models with the experimental data: ibmPorFoam (MULES) (solid blue line), ibmPorFoam (isoAdvector) (dotdashed yellow line), IHFOAM (dashed orange line), Experiment (black circles)

It is observed that at the top panel of Figure 6.3 (WG2) that ibmPorFoam (MULES) and IHFOAM give the same results until t=1.5 sec. On the other hand, ibmPorFoam (isoAdvector) gives higher results until t=1.5 sec compared to other models. Overall, all the models are in a very good agreement with the experimental data until this point. After that time, differences arise mainly due to the trapped air as the water bounces back. However, the numerical and experimental data are still in a reasonably good agreement until the end of the simulation. Moreover, it is seen from the lower panel in Figure 6.3 for WG4 that all numerical solvers give exactly the same results, and the decay shape is almost captured. In Figure 6.4, the comparison of the numerical data with experimental results at the pressure gauges is given.
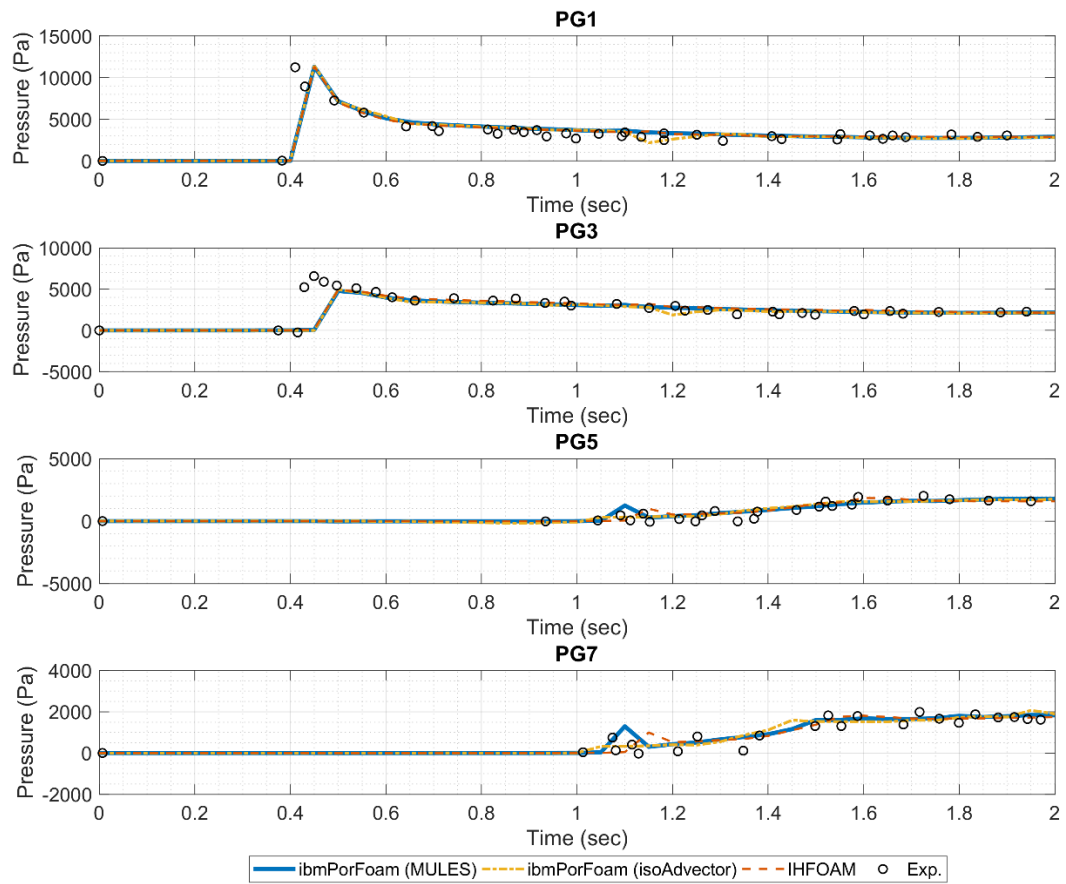
Figure 6.4. Comparison of pressure values of the numerical models with the experimental data: ibmPorFoam (MULES) (solid blue line), ibmPorFoam (isoAdvector) (dotdashed yellow line), IHFOAM (dashed orange line), Experiment (black circles)

It is seen from Figure 6.4 that all numerical solvers give almost the same results in PG1 and PG3. The impact pressures cannot be resolved accurately with any of the models even if the temporal resolution of the solution is increased, although the magnitude of the pressure is captured with all the models in PG1. There are also small variations in PG5 and PG7 at the impact instants between the numerical models. ibmPorFoam (isoAdvector) gives better results at these gauges. Other than the impact instants, the numerical data from all the numerical models are in a fairly well agreement with the experimental data in all of the pressure gauges as the quasi-

static pressure is observed in the rest of the data. The numerical modelling of the impact pressures is further discussed in more details in Section 6.1.1.1.

Overall, it can be said that ibmPorFoam performed well in replicating this experiment, and the accuracy is almost same with IHFOAM. Furthermore, it is possible to use the isoAdvector algorithm in combination with the IBM.

6.1.1.1 Further Discussions on the Numerical Modelling of the Impact Pressures in Case 1

As it is presented in the previous part, the impact pressures measured at PG1 and PG3 are not captured accurately using any of the models. The possible reasons for this issue can be the effect of the discretization scheme of the convection term (Arikawa et al., 2018), the effect of the turbulence modelling and the effect of air compressibility (Dias and Ghidaglia, 2018).

In this part, extra simulations are carried out with ibmPorFoam (MULES) to extend the discussions on the numerical modelling of the impact pressures. ibmPorFoam (MULES) is preferred as there is no difference in capturing the impact pressures with any of the models. The extra simulations are limited to a simulation time of 0.6 sec and pressure computations are only presented for PG1 and PG3 to focus on impact pressures only. Unless otherwise stated, the other parameters in the simulations are the same as the reference simulation presented in the previous part.

6.1.1.1.1 The Effect of Discretization Scheme of the Convection Term

The convection term in the integral generic equation is given by Equation 6.1.

$$\int_{cs} \rho\phi\vec{V}\cdot dA \qquad\qquad \text{Eq. 6.1}$$

In Equation 6.1, ρ is the density of the fluid, $\vec{V}$ is the velocity vector and ϕ is a general variable. This term stands for the net flux of ϕ due to convection across to control surface out of the control volume in the finite volume discretization.

This convection term can be discretized for a cell in a two-dimensional domain as given in Equation 6.2:

$$\int_{CS} \rho\phi\vec{V} \cdot dA = \sum_{ensw} \rho\phi u \, \Delta y - \sum_{ensw} \rho\phi v \, \Delta x \qquad \text{Eq. 6.2}$$

In Equation 6.2, u is the velocity component along x-direction, v is the velocity component along y-direction, Δx and Δy are cell sizes along x and y directions, respectively. "ensw" stands for "east", "north", "south" and "west" edges of a single cell having a center point denoted with P. A single cell in a cartesian grid constructed for the finite volume method is schematized in Figure 6.5. In this configuration, the values of the variables at cell-centers are known.
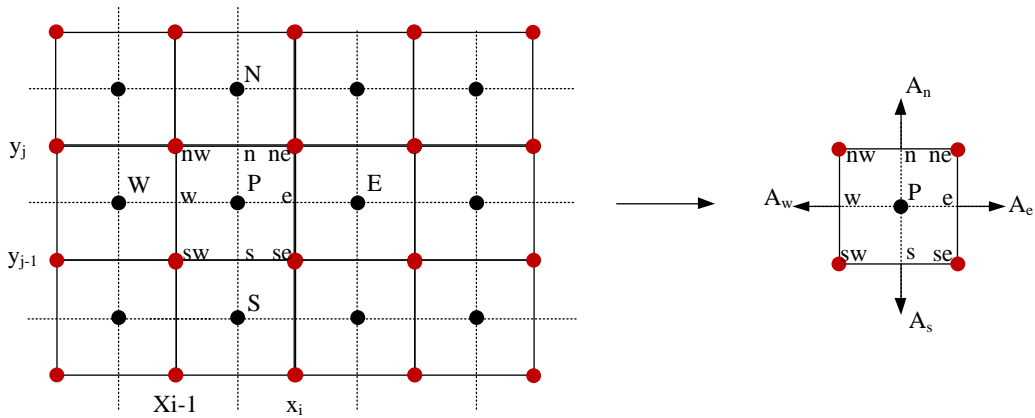
Figure 6.5. Schematic representation of a finite volume method grid and a single cell in two-dimensions (Adopted from Aydın, 2016)

The component for the east face shown in Figure 6.5 can be written as $\rho\phi_e u_e \Delta y$. As the value of ϕ_e is not known, it should be interpolated based on the values at the

surrounding cell centers. For example, one may use linear interpolation to estimate the value of ϕ_e at the cell face "e" as given in Equation 6.3.

$$\phi_e = (1 - \lambda_e) \phi_P + \lambda_e \phi_E \quad \text{where } \lambda_e = \frac{x_e - x_P}{x_E - x_P}$$

Eq. 6.3

Linear interpolation corresponds to the central differences discretization scheme which is used frequently in discretizing the convection term. The schemes to find ϕ_e are called discretization scheme of the convection term.

Arikawa et al. (2018) argued that the numerical prediction of the impact pressures strongly depends on the discretization scheme of the convection term and proposed a new discretization scheme. In this algorithm, a blending factor is determined depends on the fraction of water volume in a cell, i.e. the value of VOF indicator function (α). The upwinding and central differences schemes are blended using this factor. Although there are many discretization schemes available in OpenFOAM CFD library, this scheme is not available. Therefore, this algorithm is implemented in the framework of the present study with the name of vofBlended in ESI distribution of OpenFOAM v1706. The vofBlended scheme is applied according to Equation 6.4.

$$
\begin{aligned}
W &= 1 && \text{if } \alpha = 0 \\
W &= w && \text{if } (\alpha \, \alpha_x) > 1 \\
W &= 1 - (1 - w) \alpha \, \alpha_x && \text{otherwise}
\end{aligned}
$$

Eq. 6.3

In Equation 6.3., w is the initial weight, W is the updated weight according to the algorithm and α_x is a calibration parameter. The W is applied to find the value of ϕ_e as presented in Equation 6.4.

$$\phi_e = W \phi_{e,upwinding} + (1 - W) \phi_{e,central}$$

Eq. 6.4

In Equation 6.4, $\phi_{e,upwinding}$ is the value of ϕ_e obtained using the upwinding scheme whereas $\phi_{e,central}$ is the value of ϕ_e obtained using the central differences scheme.

The simulation presented in the previous section is conducted with vanLeerV discretization scheme of the convection term. Taking the pressure computations at PG1 and PG3 presented in Figure 6.4 as a reference, 32 additional simulations with the discretization schemes listed in Table 6.3 are carried out. These discretization schemes include second order and higher-order schemes previously available in OpenFOAM CFD library and also vofBlended scheme described above.

Table 6.3 Discretization schemes used in the extra simulations

#	Name of the Discretization Scheme in OpenFOAM	Explicit Name of the Method & Value of Related Parameters
1	linearUpwind grad(U)	Linear-upwind, employs upwind interpolation weights with and explicit correction based on the local cell gradient
2	linear	Central differences
3	Minmod	Min-Mod
4	midPoint	Mid-Point
5	MUSCL	Monotonic Upwind Scheme for Conservation Laws
6	QUICK	Quadratic Upstream Interpolation for Convective Kin.
7	UMIST	Upstream Monotonic Interpolation for Scalar Transport
8	upwind	Upwinding
9	vanLeer	Van Leer
10	limitedLinear 1	Limited Linear scheme with its coefficient
11	limitedLinear 0.8	
12	limitedLinear 0.6	
13	limitedLinear 0.4	
14	limitedLinear 0.2	
15	MUSCLV	MUSCL scheme based on the dir. of the steepest gradient
16	MinmodV	Min-Mod scheme based on the dir. of the steepest gradient
17	QUICKV	QUICK scheme based on the dir. of the steepest gradient
18	UMISTV	UMIST scheme based on the dir. of the steepest gradient
19	SuperBee	Super Bee
20	Gamma 1.0	Gamma with its coefficient
21	GammaV 1.0	Gamma scheme based on the dir. of the steepest gradient
22	SFCD	Self-filtered central differencing
23	SFCDV	SFCD scheme based on the dir. of the steepest gradient
24	SuperBeeV	Super Bee scheme based on the dir. of the steepest gradient
25	vanAlbada	Van Albada

Table 6.3 (continued)

26	vanAlbadaV	Van Albada scheme based on the dir. of the steepest grad.
27	vofBlended: 0.2 10	
28	vofBlended: 0.2 8	vofBlended, the first number is the initial weighting factor and the second number is the calibration factor
29	vofBlended: 0.2 6	
30	vofBlended: 0.2 4	
31	vofBlended: 0.2 2	
32	vofBlended: 0.2 1	

There are cases where the impact pressures are significantly overestimated. Also, there are cases where the simulations do not converge. The best alternative compared to vanLeerV is vofBlended algorithm with a calibration factor of 10 where a slight improvement in estimating impact pressure at PG3 is achieved presented in Figure 6.6.
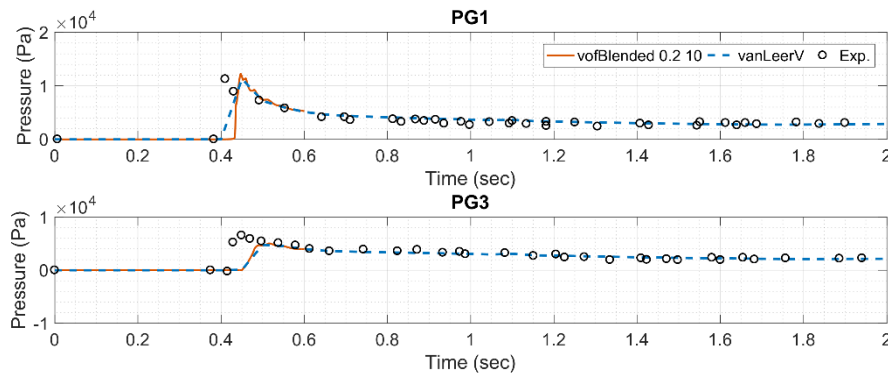
Figure 6.6. Comparison of the discretization schemes vanLeerV (dashed blue line) and vofBlended (solid orange line) in predicting the impact pressures with experimental data (black circles)

It is seen from Figure 6.6 that the discretization scheme directly affects the solution; however, the effect is minimal for the selected set of experiment. Furthermore, it is observed that the frequently used vanLeerV scheme for the convection term is an appropriate choice in Figure 6.6.

6.1.1.1.2 The Effect of Turbulence Modelling

The turbulence models used to close Reynolds-Averaged Navier-Stokes (RANS) equations tend to over-produce turbulence beneath surface waves (Larsen and Fuhrman, 2018. k-ω SST turbulence model is used as the closure model in the simulations presented for Case 1. In this section, another simulation is carried out based on the laminar flow assumption using vanLeerV as the discretization scheme of the convection term. The results are presented in Figure 6.7.
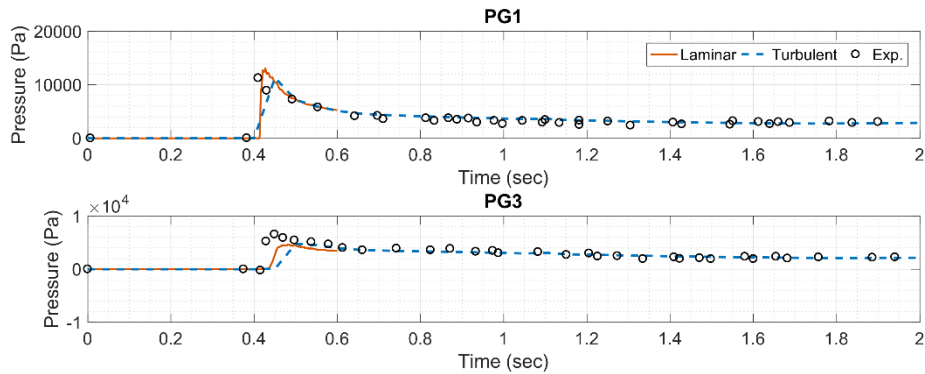
Figure 6.7. Effect of the turbulence modelling in predicting the impact pressures: Laminar (solid orange line), Turbulent (dashed blue line), Experiment (black circles)

It is seen from Figure 6.7 that the results are significantly improved at both PG1 and PG3. Therefore, it is seen that the closure model overestimates the turbulence.

6.1.1.1.3 The Effect of Air Compressibility

An extra simulation is carried out using ibmPorFoam-C which considers the effect of air compressibility. The simulation is carried out under laminar flow assumption and compared to the laminar case simulation conducted with ibmPorFoam. The results are plotted in Figure 6.10 for without air compression term (ibmPorFoam) and with air compression term (ibmPorFoam-C).
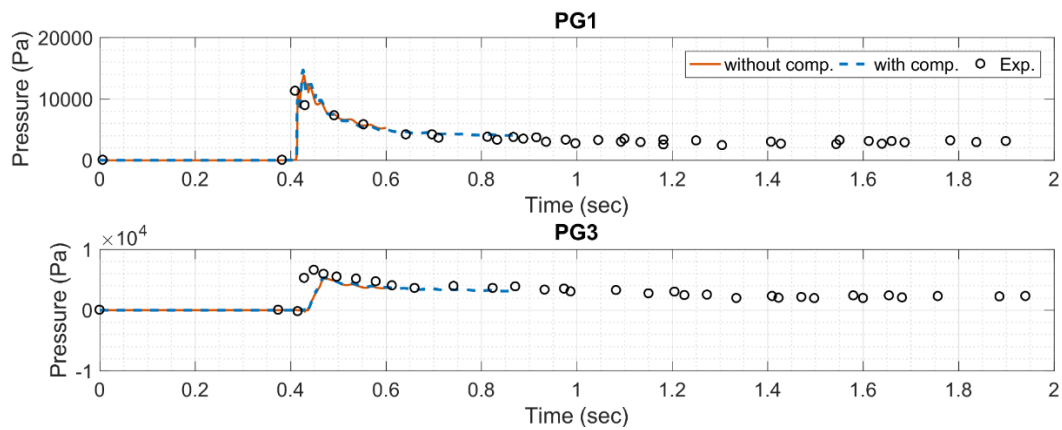
Figure 6.8. Effect of air compressibility in predicting impact pressures: With compressibility (dashed blue line), Without compressibility term (solid orange line) Experiment (black circles)

It is observed from Figure 6.10 that there is no practical difference between these simulations, although there are very small improvements in the results. Therefore, there is no effect of air compressibility for the selected case. This might be related to the elementary loading processes (Dias and Ghidaglia, 2018). The loading process can be regarded as the building jet along with the structure. In this type of loading, the air is trapped; however, it is not compressed. Therefore, the experimental and numerical results are in parallel for this case showing that the effect of air compressibility is not overpredicted by ibmPorFoam-C.

6.1.1.1.4   Remarks from the Assessment on the Numerical Prediction of Impact Pressures

In Section 6.1.1.1, an investigation on the numerical prediction of the impact pressure is carried out for the selected validation case of ibmPorFoam. The possible effects which are the discretization scheme of the convection term, the effect of the turbulence modelling and the effect of the air compressibility are investigated. A new discretization scheme is included in OpenFOAM Library, and the variant of

114

ibmPorFoam which takes the effect of air compressibility into account called ibmPorFoam-C is applied to this problem.

Overall, it is seen that the discretization scheme of the convection term is limited and there is no effect of air compressibility for the selected case. However, turbulence modelling has a significant effect on the numerical prediction of the impact pressures. The closure model used in the simulations overpredicts the turbulence which dissipates more energy than the actual dissipated energy.

This section is included to discuss the reasons why the impact pressures could not be captured in the actual validation study. In order to understand this process, a more detailed study with additional cases should be carried out. This issue is not the major aim of the present thesis study; therefore, it is left as a future study.

6.1.2 Case 2: Interaction of Dam Break Flow with Porous Material

The present numerical model is validated against the data from the physical model experiments studying 2D interaction of dam-break flow with porous material (Lin, 1998) conducted in a glass tank. Note that these experiments are widely studied in the literature discussing porous media modelling with the macroscopic approach (Liu et al., 1999; del Jesus et al. 2012; Jensen et al., 2014; Higuera et al. 2014a). When there is no immersed body defined in the computational domain such as in this validation case, the equations solved by ibmPorFoam reduce to the equations solved by IHFOAM. From this point of view, one might consider studying this case as not very novel and necessary. However, it is the first time that isoAdvector algorithm is used within the porous media flow, and it is still important to observe the performance of isoAdvector algorithm in simulating Lin (1998) experiments as this is a well-defined and widely studied reference study in the literature.

The porous material used in the experiments was crushed rocks with a nominal diameter of (D_{50}) 1.59 cm and porosity of 0.49. The height and width of the porous medium was 58 cm and 29 cm, respectively, and the height of the dam is 35 cm with

an initial water level of 2.5 cm. The experiments presented by Lin (1998) were conducted considering 2D behaviour, and the free surface is measured all along with the glass tank by the use of video recordings. The experimental setup is presented in Figure 6.9.
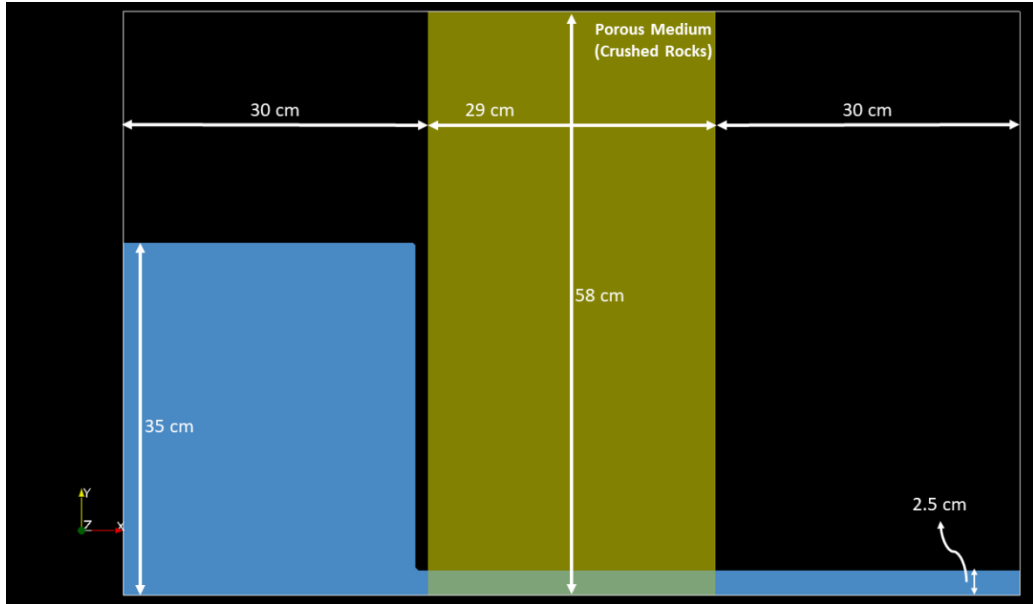
Figure 6.9. Experimental setup

The computational domain is constructed as a 2D configuration for ibmPorFoam. Uniform mesh size of 0.25 cm is used along x and y-axes revealing approximately 83000 cells. Grid Convergence Index (GCI) analysis is performed to achieve mesh independency. GCI is calculated as 1.9% that could be regarded as an acceptable value. All the faces except for the top one are defined as reflective walls, and the top face is defined as the atmosphere boundary condition. The simulation duration is kept as 2.0 seconds. No turbulence models are used in the simulations as Jensen et al. (2014) argued that there is no need for a turbulence model in the presence of porous media as the friction and added mass coefficients can be calibrated to account for the variations in the flow properties due to the turbulence. In the present study, the linear friction (a) and non-linear friction (b) coefficients are used as 500 and 2.0 for ibmPorFoam simulations, respectively, as Jensen et al. (2014) calibrated these parameters considering a wide range of flow regimes. In other words, no specific

calibration study for these parameters are carried out in this study, these parameters are taken from the literature. As given in Equations 5.2 and 5.3, definitions of porous media closure term *A* are different in IHFOAM and ibmPorFoam by a factor of *(1-n)*. Therefore, the linear friction coefficient is taken as 980 in IHFOAM to have the same numerical setup, and the non-linear friction coefficient is again taken as 2.0. In both models, the added mass coefficient (C) is taken as 0.34 (del Jesus et al., 2012). Snapshots from the simulation are presented in Figure 6.10, and the comparisons of the free-surface elevations from the experimental and numerical results are presented in Figure 6.11.
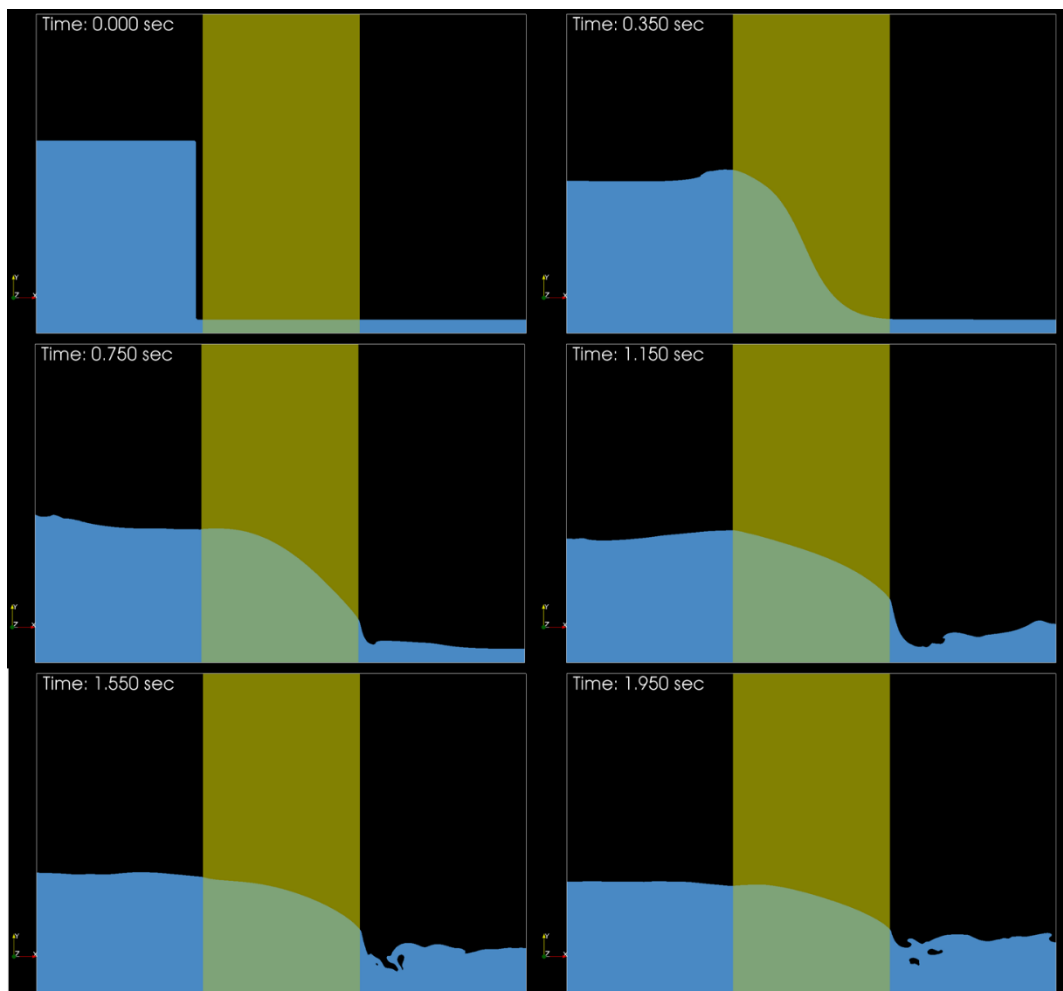
Figure 6.10. Snapshots from the simulation, ibmPorFoam (MULES)
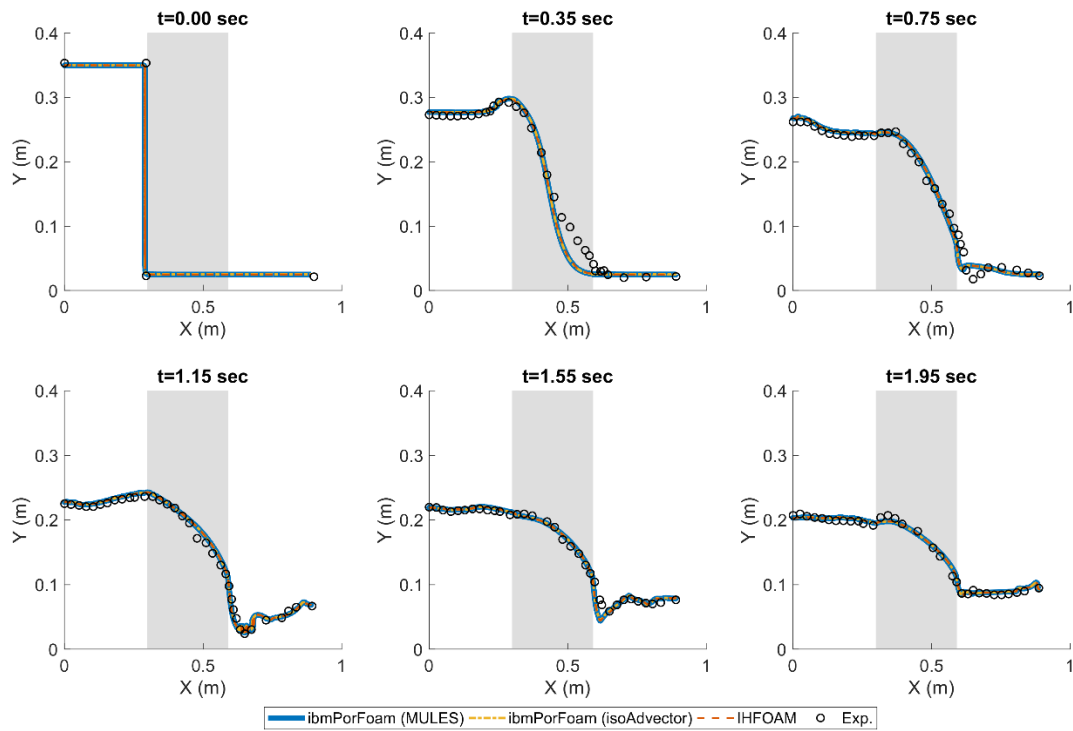
Figure 6.11. Comparison of free surface elevations of the numerical models with the experimental data (Grey region indicates the porous region.): ibmPorFoam (MULES) (solid blue line), ibmPorFoam (isoAdvector) (dotdashed yellow line), IHFOAM (dashed orange line), Experiment (black circles)

In Figure 6.10 and Figure 6.11, it is seen that the dam break flow moves slower in the porous medium due to the friction; therefore, the water level inside the porous region firstly increased, and then decreased slowly. At the right-hand side of the porous medium, relatively random motion and air entrainment are observed due to the interaction of flow with the porous region. It is observed that the free surface is captured in a reasonably well agreement with all models. The deviation from the experimental data at t=0.35 sec is most probably related to the speed of the plate that blocks the water body, i.e., dam. All the numerical models give approximately the same result at each time step. In summary, ibmPorFoam (MULES) and ibmPorFoam (isoAdvector) are capable of replicating interaction of dam break flow with a porous material, and they give approximately same results with IHFOAM concluding that

118

the isoAdvector algorithm is appropriately modified to account for the porous media flow.

6.1.3 Case 3: Solitary Wave Propagation over a Submerged Permeable Breakwater

The third experimental dataset used in the validation studies is the solitary wave propagation over a submerged permeable breakwater by Wu and Hsiao (2013). The experimental data is used to validate numerical models in several studies (Wu et al., 2013; Wu and Hsiao, 2013; Khayyer et al., 2018); however, it is the first time that a numerical model based on OpenFOAM is validated against this dataset. Furthermore, this experimental data set is one of the good examples in the literature to apply microscopic porous media modelling approach as the geometry of the structure is well-defined. Thus, it is aimed to show the differences in representing impervious solid boundaries for microscopic porous media modelling approach using the IBM and using the body conformal mesh configurations. It is noted that we do not compare the macroscopic and microscopic porous media modelling approaches in this case, as Wu et al. (2013) previously studied this question and showed that both approaches are applicable. The experiments were carried out in a 25 m long, 0.5 m wide and 0.6 m deep channel. A permeable breakwater was mounted on the bottom of the flume with dimensions 13 cm in length, and 6.5 cm in height. The permeable breakwater was constructed using spheres with a diameter of 1.5 cm placed in a non-staggered pattern yielding a porosity of 0.52. The spheres are connected with the material. The water level is set to 10.6 cm, and solitary waves with a height of 4.77 cm were used in the experiments. The water surface elevation was recorded with two wave gauges in front and at the back of the breakwater, and the velocity field in the vicinity of the breakwater was measured by a Particle Image Velocimetry system. The reader is referred to the original paper for further details on the experimental setup and measurement systems. Side view of the experimental

setup is given in Figure 6.12. Note that a shorter wave channel is illustrated in the figure.
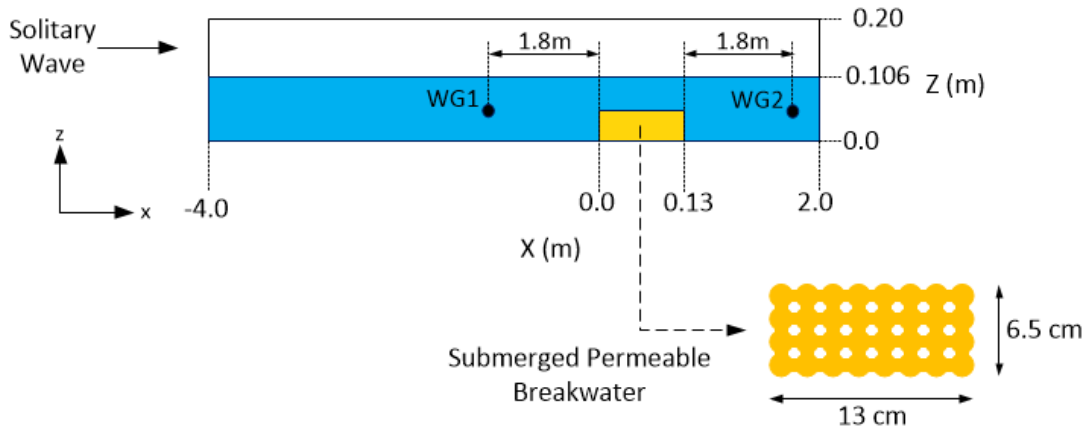
Figure 6.12. Experimental setup (Figure is not to scale!)

The computational domain in xz plane is constructed in the same way presented in Figure 6.12 for ibmPorFoam. The length of the computational domain in the y-direction is selected as 3.25 cm to reduce the computational time. The breakwater model is constructed as shown in Figure 6.13 with two spheres in y-direction.
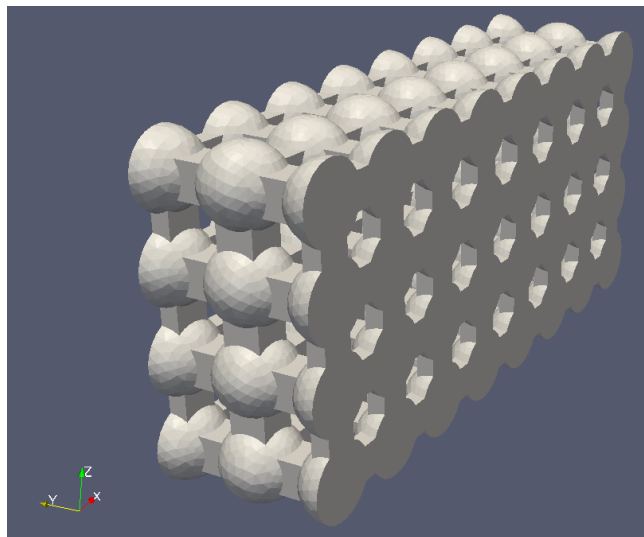
Figure 6.13. Permeable breakwater model

There is extra material between the spheres yielding a porosity of 0.52 as in the case of the experiments. The breakwater is represented as an IB in the computations, and

the no-slip boundary condition is applied to this IB. k-ω SST model is used as the turbulence closure in this case, and the simulation duration is kept at 7.5 seconds. A uniform mesh size of 0.5 cm and 0.25 cm are used in x- and y-directions, respectively. Along z-direction, a variable mesh size starting from 0.1 cm at the bottom increasing up to 0.5 cm at the top is used. Additional mesh refinement around the breakwater is applied reducing the mesh sizes to 0.25 cm in the x-direction and 0.125 cm in the y-direction. In total, the number of cells is approximately 1.4 million. The mesh independency tests are performed using GCIs that is found to be 1.6% at most which are regarded as acceptable. The face at the left-hand side in Figure 6.12 is defined as a wave generating boundary with active wave absorption whereas the face at the right-hand side is defined as a purely absorbing boundary. The face at the bottom is defined as a wall, and the face at the top is defined as the atmosphere boundary condition. The front and back faces where the breakwater along the y-axis are defined as a symmetry boundary condition. Symmetry boundary conditions at the front and back faces for the same problem were successfully applied by Wu et al. (2013). For the simulation with IHFOAM, the same numerical setup is used except for the representation of the breakwater. In Figure 6.14, the mesh configurations for IHFOAM and ibmPorFoam simulations are presented to show the differences.
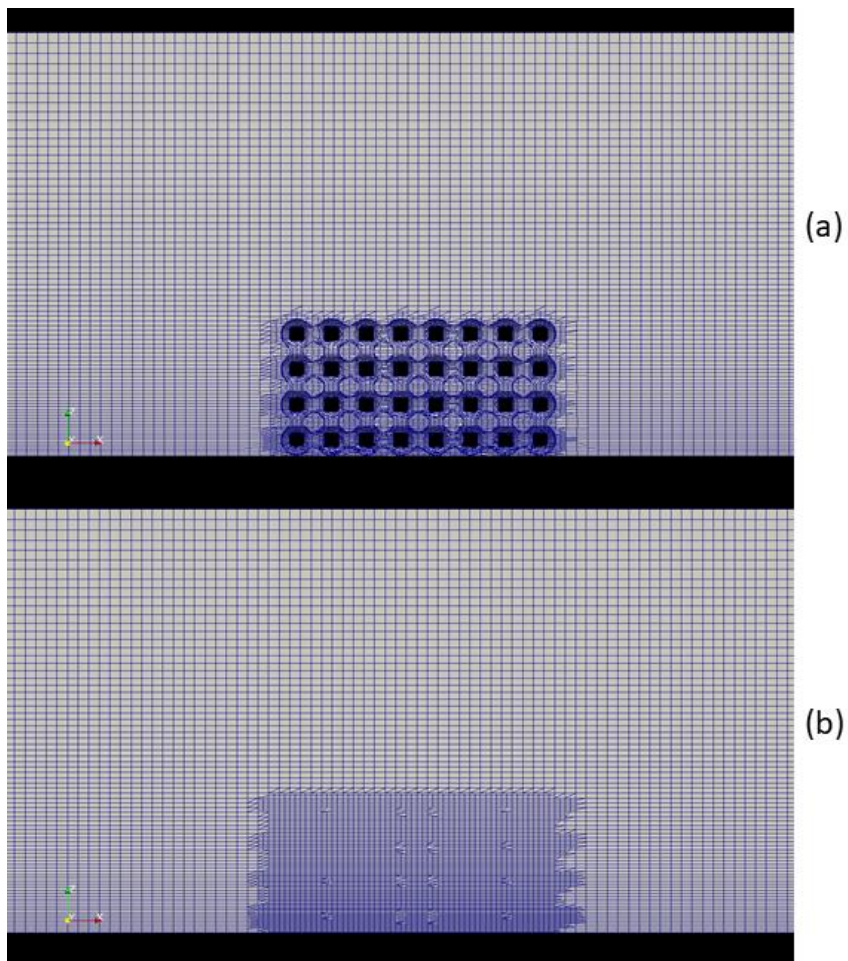
Figure 6.14. Mesh configurations for (a) IHFOAM (b) ibmPorFoam

The breakwater is extracted from the computational domain for IHFOAM simulation (Figure 6.14a) that is rather challenging as the geometry of the breakwater is relatively complex. Thus, body-conformal mesh configuration is used in the simulation. In Figure 6.14b, the region for the breakwater can be seen as a refined region as additional mesh refinement is performed around the breakwater that is represented as an IB in ibmPorFoam simulations. The snapshots from the simulation with ibmPorFoam (MULES) are presented in Figure 6.15 indicates the velocity field.
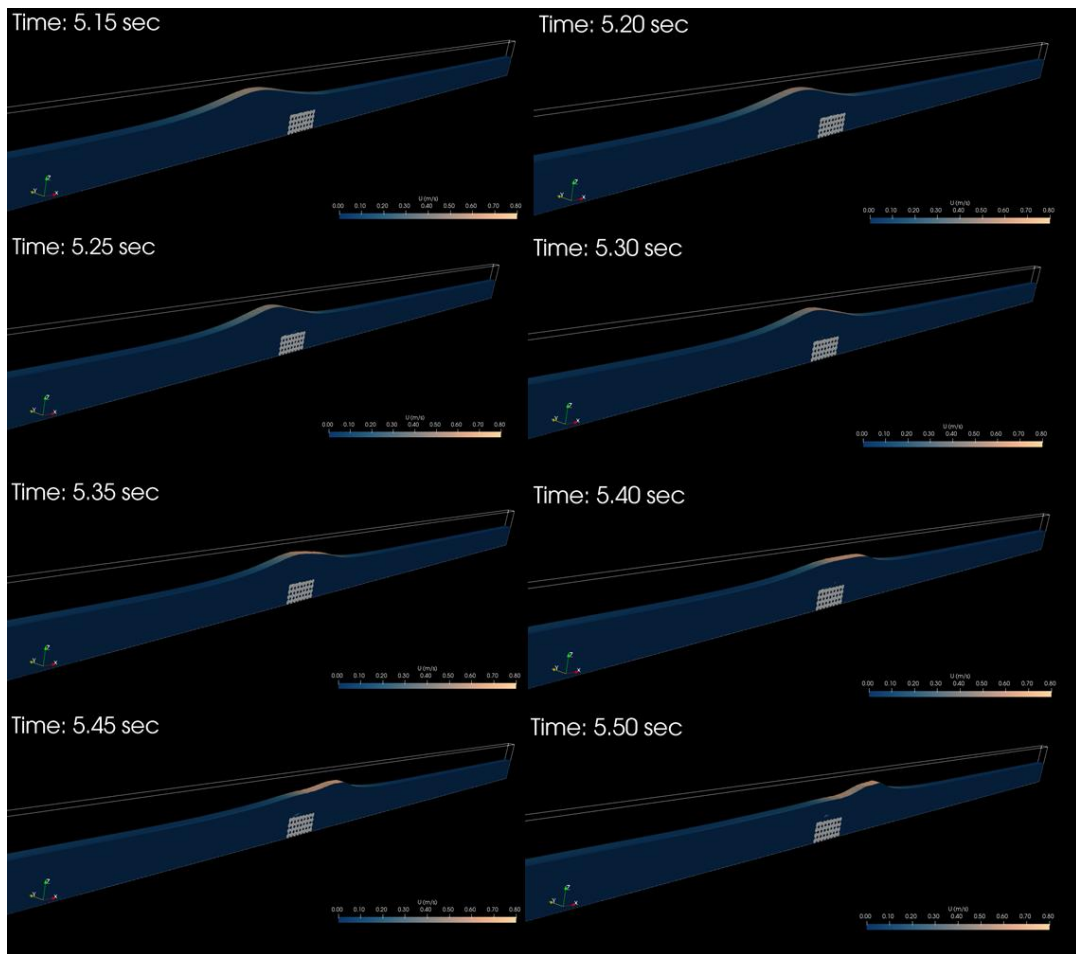
Figure 6.15. Snapshots from the simulation, ibmPorFoam (MULES)

It is clearly seen in Figure 6.15 that the form of the solitary wave is affected by the submerged breakwater. The velocity at the front of the wave approaches to 0.8 m/s after the breakwater. The comparison of the water surface elevation data from the numerical models and experiments at the wave gauges are presented in Figure 6.15.
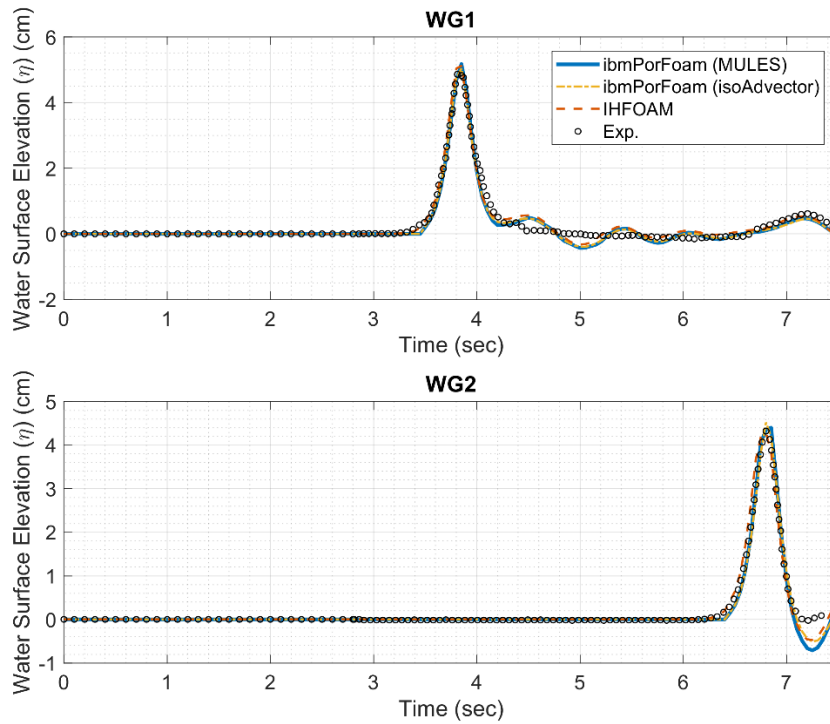
Figure 6.16. Comparison of water surface elevations of the numerical models with the experimental data: ibmPorFoam (MULES) (solid blue line), ibmPorFoam (isoAdvector) (dotdashed yellow line), IHFOAM (dashed orange line), Experiment (black circles)

It is observed from Figure 6.16 that all the models captured the free surface accurately at both gauges. There are some minor deviations from the experimental data due to the reflection from the outlet that could not be absorbed. In Figure 6.17, Figure 6.18 and Figure 6.19, the numerical data and the experimental data for the velocity profiles along the selected lines around the breakwater are compared at t=5.3 sec, t=5.7 sec and t=6.1 sec, respectively. The velocity profiles are given for both the horizontal velocity component in the x-direction (u), and the vertical velocity component in the z-direction (w) at the y=0.375 cm lateral slice. Note that the origin is indicated in Figure 6.12.
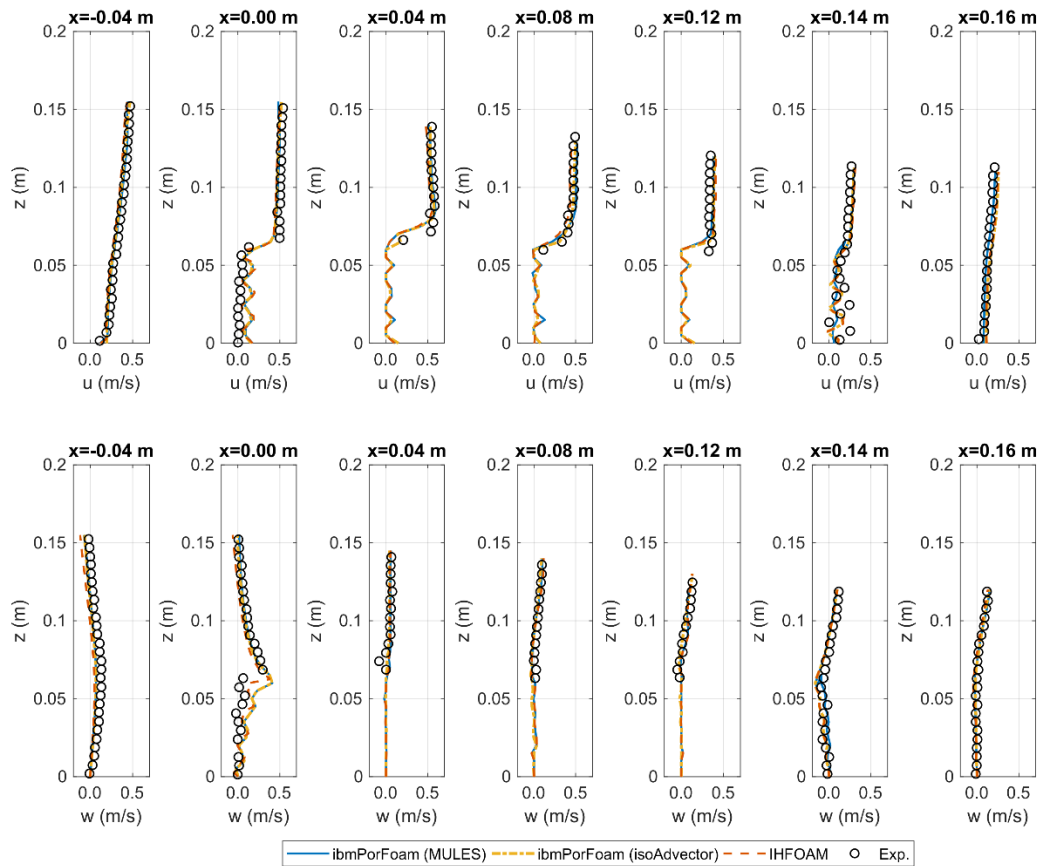
Figure 6.17. Comparison of the velocity profiles along the selected lines of the numerical models with the experimental data at t=5.3 sec: ibmPorFoam (MULES) (solid blue line), ibmPorFoam (isoAdvector) (dotdashed yellow line), IHFOAM (dashed orange line), Experiment (black circles)

In Figure 6.17, it is seen that the numerical and the experimental data are in good agreement. At x=0.00m, oscillations in u and w are observed in the numerical data as this line is the boundary of the breakwater. The variations in the horizontal component of the particle velocities at x=0.14m (rear side of the breakwater) are seen and captured in a reasonable accuracy with all the models. These variations are due to the flow injection (Wu, Yeh and Hsiao, 2013).

125
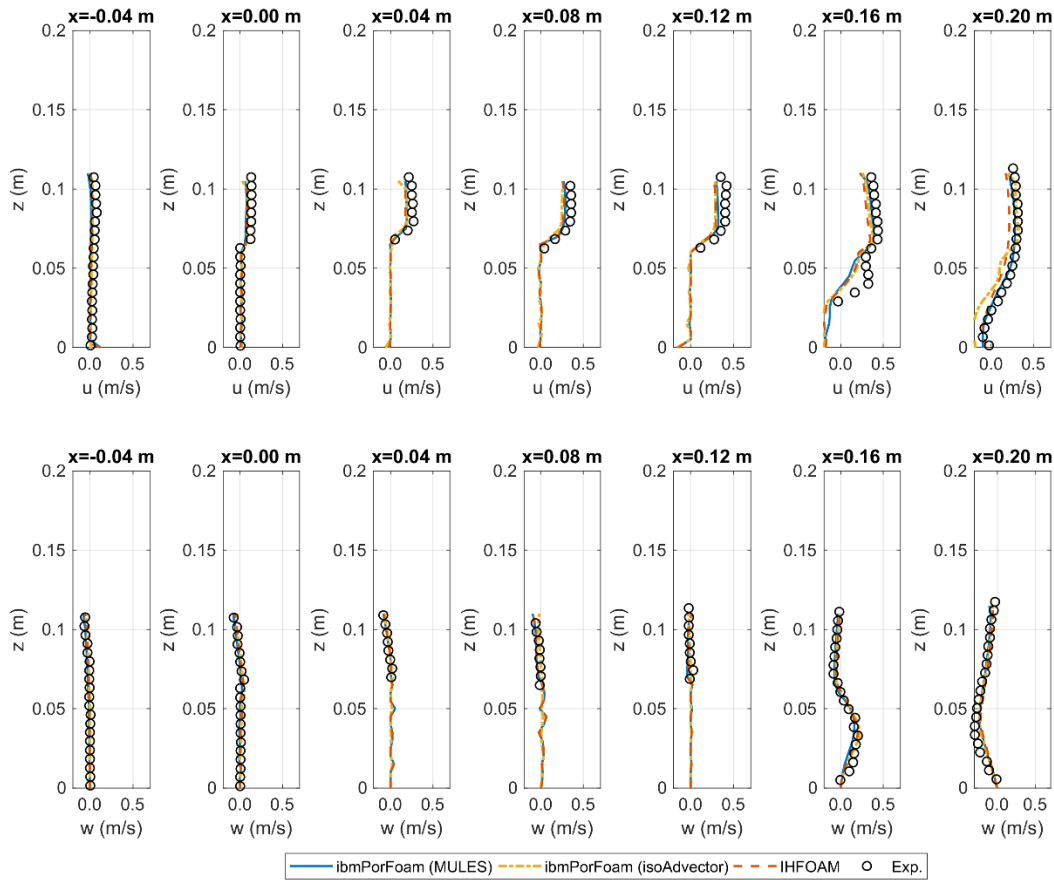
Figure 6.18. Comparison of the velocity profiles along the selected lines of the numerical models with the experimental data at t=5.7 sec: ibmPorFoam (MULES) (solid blue line), ibmPorFoam (isoAdvector) (dotdashed yellow line), IHFOAM (dashed orange line), Experiment (black circles)

In Figure 6.18, the numerical data is in a good agreement with the experimental data; however, at x=0.12m all the models underestimated the horizontal particle velocities. At x=0.16m, the velocity profile in the horizontal direction could not be captured accurately between z=0.02m and z=0.05m even the magnitudes are in a good agreement. Further, at x=0.20m, the horizontal particle velocities are captured accurately by ibmPorFoam (MULES) and ibmPorFoam (isoAdvector) above z=0.06m whereas IHFOAM underestimates. On the other hand, ibmPorFoam (isoAdvector) overestimates the magnitudes of the horizontal particle velocities under z=0.06m.

126
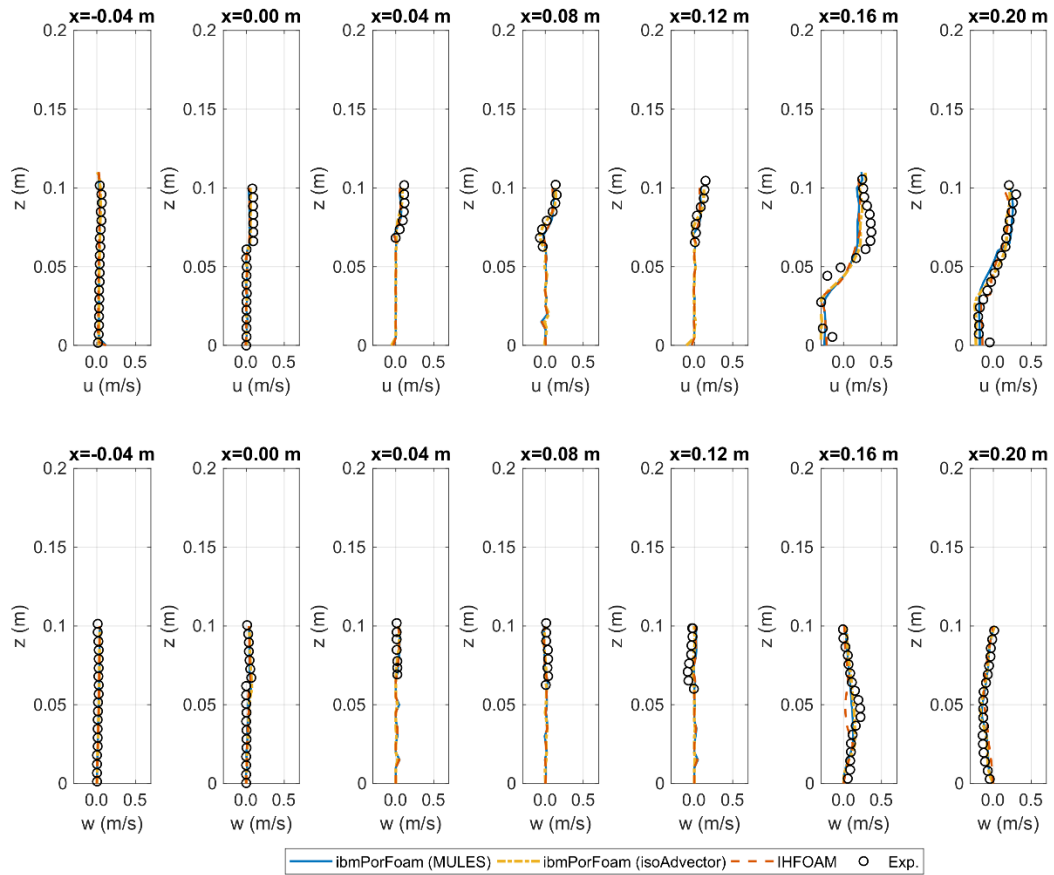
Figure 6.19. Comparison of the velocity profiles along the selected lines of the numerical models with the experimental data at t=6.1 sec: ibmPorFoam (MULES) (solid blue line), ibmPorFoam (isoAdvector) (dotdashed yellow line), IHFOAM (dashed orange line), Experiment (black circles)

In Figure 6.19, the velocity profiles computed by the numerical models fit the experimental data with good accuracy except for the horizontal velocity profiles at x=0.16m. At x=0.16m, the velocity profile could not be resolved very well in shape; however, the magnitudes of the velocities are captured at an acceptable accuracy.

Overall, the selected experiment is replicated accurately with all the models. There are some minor differences between the models that could be seen in the velocity profiles. This is mainly because the representation of the porous breakwater is different in the models. Furthermore, these comparisons show that isoAdvector algorithm can be used in combination with IBM.

6.1.4   Case 4: Solitary Wave Attack on a Rubble Mound Breakwater

The final case is the solitary wave attack on a rubble mound breakwater presented in Chapter 3. In Chapter 3, this case and several other cases are studied using IHFOAM discussing the performance of Haydarpaşa Breakwater under tsunami attack. Note that IHFOAM solver used in Chapter 3 i compiled with OpenFOAM version 2.1.1 (OpenFOAM, 2012) and the porous media coefficients are particularly calibrated in that section. This case is again simulated in the scope of the validation studies of ibmPorFoam using IHFOAM solver compiled with OpenFOAM version 1706 (OpenFOAM, 2017) and with porous media coefficients suggested by Jensen et al. (2014). This case is selected to validate ibmPorFoam in presence of an impervious boundary (the crown-wall of the breakwater) represented by the IBM and porous medium (armour, filter and core layers of the breakwater) represented using macroscopic porous media flow modelling approach. The experimental configuration indicating the measurement devices is given in Figure 3.1, and a closer look to the breakwater is presented in Figure 3.2.

The computational domain is constructed as given in Figure 3.6 for ibmPorFoam shorter than the actual wave channel to reduce computational cost. As the physical model experiments can be regarded as 2D, the numerical simulations are also carried out in a 2D numerical wave tank. Uniform mesh size of 1 and 0.5 cm along x and z-axes are used, respectively. Mesh independence is guaranteed by GCI analysis where it is calculated as 1.8%. The crown-wall of the rubble mound breakwater is defined as an IB. Additional refinement is performed around the crown-wall reducing the mesh sizes in x and z directions to 0.5 and 0.25 cm, respectively. The total number of cells used in the simulations is around 1 million. The wave generating boundary condition is defined using the measured water surface elevation and the measured water particle velocity time series at WG1 and ADV1, respectively, at the right-hand side boundary in Figure 3.6b. Wave absorbing boundary condition is defined at the left-hand side boundary in Figure 3.6b. The bottom face is defined as a wall whereas the top face is atmosphere boundary condition. The simulation duration is kept as 20

seconds, and k-ω SST turbulence model is used in the simulations. A similar numerical configuration is used for IHFOAM simulations. The major difference is the representation of the crown-wall. For IHFOAM, the crown-wall is extracted from the computational domain revealing almost 1 million cells (still less than the total number of cells for ibmPorFoam) including the additional refinement around the extracted region. Extracting the crown-wall from the computational domain is simpler than for Case 3 and more challenging than Case 1 as the geometry of the crown-wall is simpler than the permeable breakwater (Case 3) and more complex from the box (Case 1). However, it is still more time-consuming than the mesh generation process for ibmPorFoam. In both numerical simulations, the slope is extracted from the computational domain to reduce the computational time. In the present study, the linear friction (*a*) and non-linear friction (*b*) coefficients are used as 500 and 2.0 for ibmPorFoam simulations in all layers of the breakwater based on the discussions by Jensen et al. (2014). For IHFOAM, the linear friction coefficients are recalculated as discussed in Section 6.1.3 to have the same numerical setup with ibmPorFoam simulations, and the non-linear porous media coefficient is used as 2.0. Added mass coefficient (*C*) are taken as 0.34 for all the models (del Jesus et al.). Friction and added mass coefficients in addition to the porosity and nominal stone diameters of the porous layers, i.e., parameters for porous media modelling, are presented in Table 6.4.

Table 6.4 Parameters for porous media modelling (Case 4)

Layers	Nominal Diameter of Stones (D_{n50}) in meters	Porosity (*n*)	ibmPorFoam Porous Media Coefficients			IHFOAM Porous Media Coefficients		
			a	*b*	*C*	*a*	*b*	*C*
Armour	0.040	0.40	500	2.0	0.34	833	2.0	0.34
Filter	0.033	0.35	500	2.0	0.34	770	2.0	0.34
Core	0.015	0.30	500	2.0	0.34	715	2.0	0.34

In Figure 6.20, snapshots from the simulation with ibmPorFoam (MULES) are presented showing the velocity field around the breakwater.
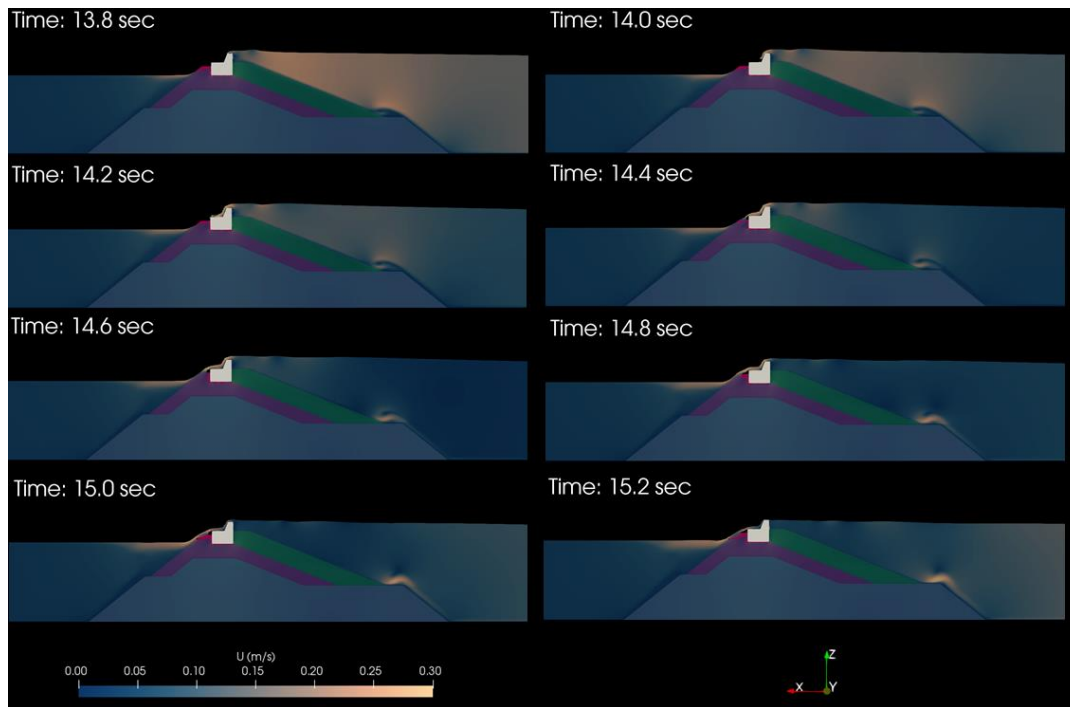
Figure 6.20. Snapshots from the simulation, ibmPorFoam (MULES)

It is seen from Figure 6.20 that solitary wave overflows the rubble mound breakwater between t=13.8 sec and t=15.2 sec. The magnitude of the velocity around the breakwater reaches to 0.3 m/s on the top of the crown-wall and at the rear-side of the breakwater near the free surface. Velocity magnitudes are higher on the stones at the seaside compared to velocity magnitudes on the stones at the rear-side of the breakwater associated with the minor damage at the seaside of the breakwater. This observation is matched with the experimental observation reported in Chapter 3. Furthermore, the separation of flow at the seaside toe of the breakwater is seen in the snapshots. In Figure 6.21, the water surface elevation from the numerical simulations is compared to the physical model experiments at eight wave gauges.
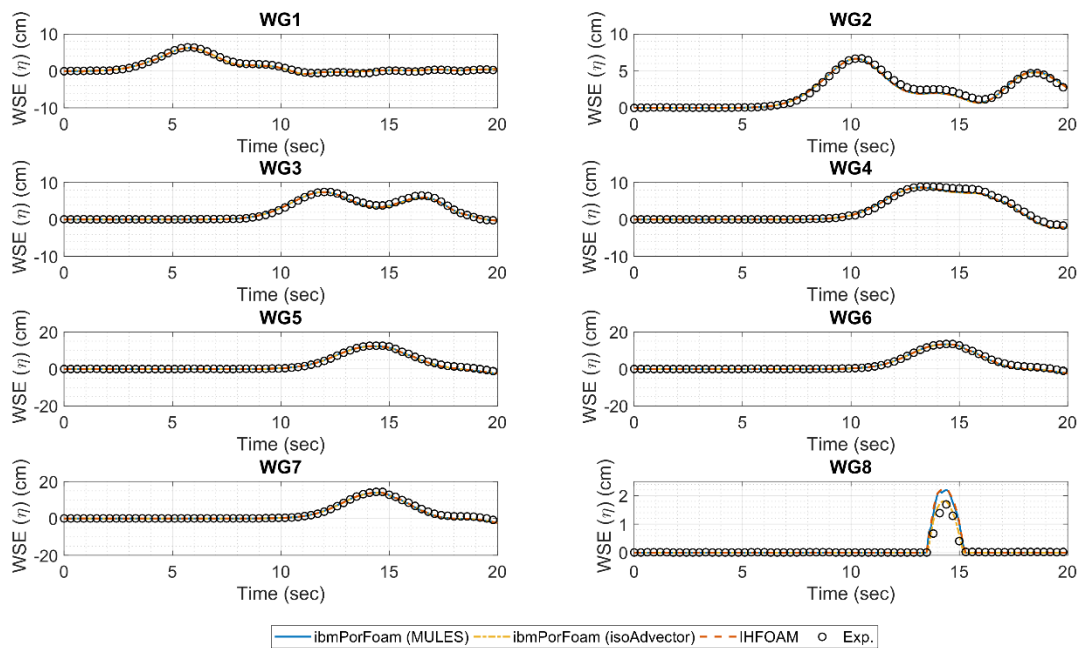
Figure 6.21. Comparison of water surface elevations of the numerical models with the experimental data: ibmPorFoam (MULES) (solid blue line), ibmPorFoam (isoAdvector) (dotdashed yellow line), IHFOAM (dashed orange line), Experiment (black circles)

It is seen from Figure 6.21 that all the models give almost the same results, and these numerical results are in a good agreement with the experimental data. The only deviation from the experimental data is at WG8. ibmPorFoam (MULES) and IHFOAM slightly overestimate the water surface elevation above the crown-wall (referred to as overflow height). On the other hand, ibmPorFoam (isoAdvector) predicts the overflow height in good accuracy. In Figure 6.22, the numerical results and experimental results for the horizontal component of the particle velocities are compared at three ADVs.
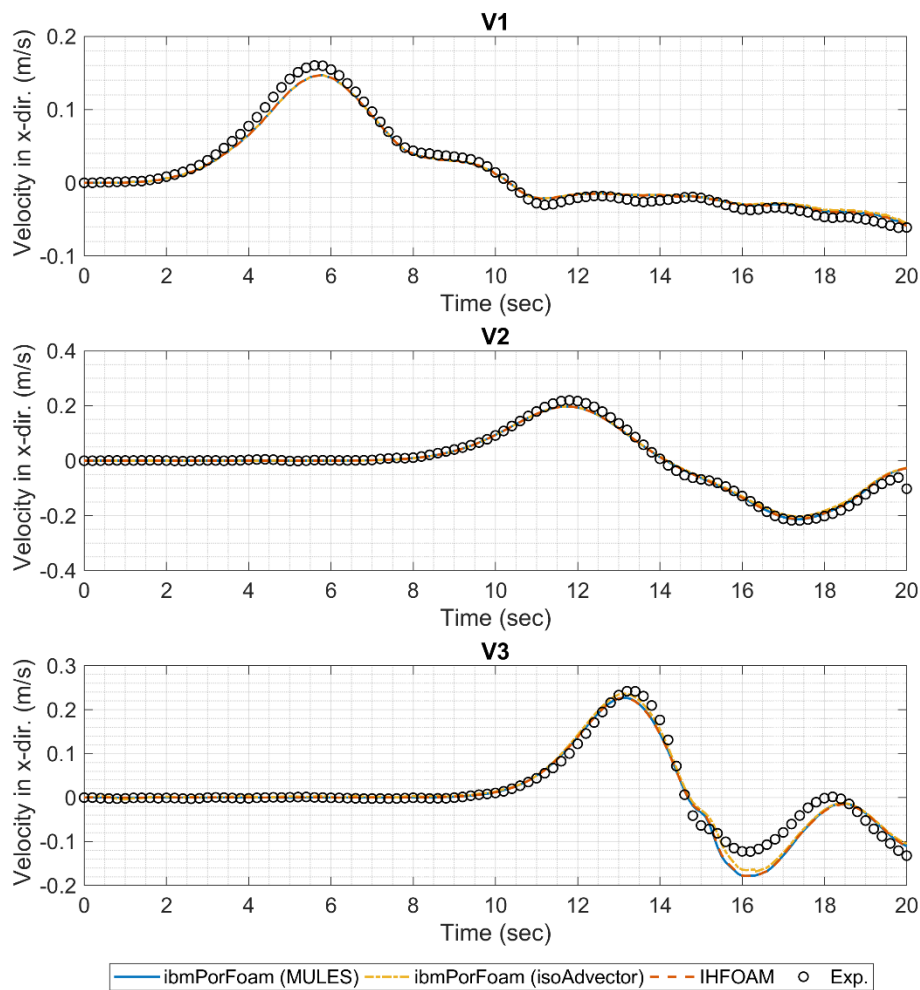
Figure 6.22. Comparison of velocity measurements of the numerical models with the experimental data: ibmPorFoam (MULES) (solid blue line), ibmPorFoam (isoAdvector) (dotdashed yellow line), IHFOAM (dashed orange line), Experiment (black circles)

Figure 6.22 shows that the horizontal component of the particle velocities in the x-direction are calculated similarly by all the numerical models, and the numerical computations fit the experimental data in a reasonably well accuracy. Minor deviations are observed at ADV3 after the wave reflects from the breakwater. As the location of this measurement device is so close to the toe of the breakwater, this deviation might be originated from macroscopic porous media modelling approach, i.e., volume averaging. Another possibility is the 2D/3D effects that could not be

132

replicated in these simulations. However, it is still reasonable to state that the general trend and magnitudes of the particle velocities are captured.

As a summary from this final validation study, ibmPorFoam is validated against an experimental configuration involving both an impervious region represented as an IB and porous regions are taken into account using the macroscopic porous media modelling approach. In this case, it is again seen that isoAdvector algorithm is modified appropriately for porous media flows, and it can be used in combination with the IBM. Furthermore, even if the mesh generation procedures and VOF schemes are different, all the models give almost the same computational results.

6.1.5   Overall Conclusions from the Validation Studies of ibmPorFoam

ibmPorFoam is validated in Section 6.1 against four experimental datasets. Overall, it is seen that ibmPorFoam is capable of replicating the selected experiments in a similar accuracy with IHFOAM.

A brief discussion of the numerical prediction of the impact pressures is given. It is seen that turbulence modelling can be significantly effective as the closure models for RANS equations can be dissipative. The effect of the discretization scheme of the convection term is found to be limited for this validation case. No effect of air compressibility is observed for the selected case, as the loading process does not include compression of the trapped air.

At the beginning of the validation studies, several questions are stated regarded as the secondary aim of these validation studies. The questions and the answers for these questions are given below:

- "What are the differences in representing impervious boundaries using body conformal mesh configurations and using IBM?": Throughout all the validation studies, these differences are discussed comparing IHFOAM with ibmPorFoam. The accuracy of the ibmPorFoam is quite similar to the IHFOAM. This result is essential as both models solve the same equations

even if the solid body representation methodologies differ. The advantage of IBM is mainly the ease of mesh generation process. On the other hand, the computational time required for ibmPorFoam is approximately 50% higher than IHFOAM depending on the size of the solid boundaries in the computational domain represented by the IBM.

- "Is isoAdvector scheme applicable in capturing free surface when the impervious boundaries are represented using IBM?": In Cases 1, 3 and 4, the performance of the isoAdvector scheme is tested when this free surface capturing algorithm is used in combination with the IBM. It is seen that the numerical results are in a reasonably well agreement with the experimental data when isoAdvector scheme is used in combination with the IBM.

- "Is the modification of isoAdvector scheme that is presented for macroscopic porous media flow modelling approach appropriate?": Behavior of the slightly modified isoAdvector scheme for macroscopic porous media modelling approach is tested in Case 2 and Case 4. The results show that the modification in the isoAdvector algorithm is appropriate.

- "What are the advantages and disadvantages of using IBM compared to body conformal mesh configurations when using microscopic porous media modelling approach?": In Case 3, flow around a porous breakwater is studied using the microscopic porous media modelling approach. The major advantage of using IBM that is the ease in mesh generation becomes more significant in this type of cases as the complex geometries of the porous structures can be represented in a straightforward manner with the body force IBM whereas it is required to remove the porous structure from the computational domain when the body conformal mesh configurations are considered.

- "Does isoAdvector scheme improve the results in free surface capturing compared to MULES scheme when different types of waves are concerned rather than progressive waves?": In the present study, dam break flow (Case 1 and Case 2) and solitary waves (Case 3 and Case 4) are in interaction with

the structures. No significant differences are observed in between MULES and isoAdvector algorithms in the scope of the selected problems even if there are minor improvements in several comparisons when we use isoAdvector algorithm with different wave types namely dam-break flow and solitary waves.

The computational times of the simulations conducted with ibmPorFoam and IHFOAM are compared in Table 6.5 for each of the validation cases. The resuts for ibmPorFoam are from the simulations conducted with the MULES algorithm in order to make a reasonable comparison with IHFOAM noting that IHFOAM also uses the same algorithm.

Table 6.5 Comparison of computational times

Case #	Number of Cells		Computational Time Needed for (hours)		Number of Threads	Computational Power
	ibmPorFoam	*IHFOAM*	*ibmPorFoam*	*IHFOAM*		
1	242,004	220,909	~1.50	~0.92	4	Intel® Xeon® E5-2630 v4 2.2 GHz with 64 GB RAM
2	82,592	82,592	~0.50	~0.38	1	Intel® Xeon® E5-1650 v3 3.5 GHz with 16 GB RAM
3	1,338,895	1,279,739	~11.48	~4.92	20	Intel® Xeon® E5-2630 v4 2.2 GHz with 64 GB RAM
4	999,286	996,169	~30.86	~23.11	12	Intel® Xeon® E5-2630 v4 2.2 GHz with 64 GB RAM

It is observed from Table 6.5 that the computational demand for the ibmPorFoam is more than IHFOAM. The major explanation for that is the total number of cells used for ibmPorFoam is always higher than IHFOAM whenever an IB is defined. Furthermore, as the equations are modified for the IBM in ibmPorFoam, more iterations are usually required for convergence. However, even if the theoretically same equations are solved as in Case 2, the computational time required for

ibmPorFoam is still higher. The reason why is there are some extra computations in ibmPorFoam related to the IBM such as computation of body forces even if there is no IB. On the other hand, the time for mesh generation used for IHFOAM is clearly higher than ibmPorFoam. As the geometry of the solid objects gets more complex, the time required for mesh generation is getting higher. Furthermore, advanced meshing tools are usually needed for the more complex geometries.

The main drawback of ibmPorFoam is that the wall functions around the immersed boundaries are not implemented at this stage. This might cause some inaccuracies to resolve the boundary layer around the immersed boundaries. However, it is seen from the validation studies that this does not cause vital problems in the scope of the wave-structure interaction problems; therefore, it is left as a future study.

6.2   Validation of rubbleFoam

As introduced in Section 5.3, VARANS equations are solved in rubbleFoam based on the cut-cell immersed boundary method for stationary and moving boundaries in the computational domain. The free-surface is captured using the VOF method in this solver. The most important improvement in rubbleFoam compared to ibmPorFoam is that it is capable of simulating flow fields around the moving boundaries. Therefore, it is planned to validate this solver with problems where the moving boundaries and the free-surface are concerned. However, there is a lack of experimental data involving free-surface. Therefore, a test study focusing on the motion of an oscillating cylinder without comparison with experimental/analytical data and a validation study focusing on the sinking of a cylinder in comparison with analytical data are presented in this section.

6.2.1   Test Study: An Oscillating Cylinder with Free-Surface

In this test study, the changes in the free-surface due to the motion of an oscillating cylinder are presented with a two-dimensional simulation. A computational domain

of 3 m in length (x-direction) and 1.6 m in height (y-direction) is constructed shown in Figure 6.23. A cylinder having a diameter of 0.5 m is placed inside the computational domain where the center of the cylinder is at x=1 m and y=0.5 m. A constant mesh size of 4 cm in both horizontal and vertical directions is selected. The water level is set as 1 m. The simulation duration is kept as 4 sec. The required computational time is approximately 6 hours on a single thread (Intel® Xeon® E5-2630 v4 2.2 GHz with 64 GB RAM).
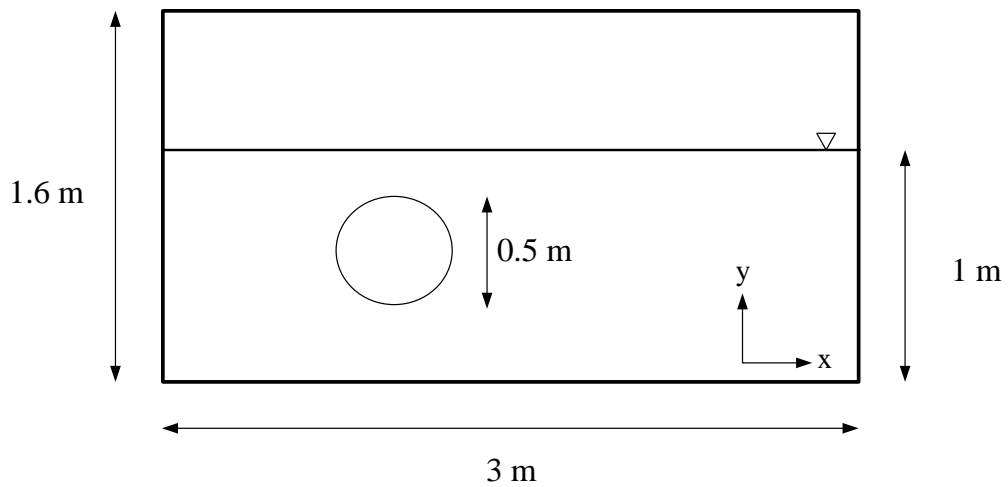
Figure 6.23. Dimensions of the computational domain

The cylinder is oscillating according to simple harmonic motion equation given by Equation 6.5.

$$x(t) = a_{osc} \, cos\left(\omega_{osc} t\right) \qquad\qquad \text{Eq. 6.5}$$

In Equation 6.5, x is the path of the center of the cylinder; t is time; a_{osc} and ω_{osc} are the amplitude and frequency of the harmonic motion. The amplitude and frequency of the motion are taken as 0.5 m and 0.4 s^{-1}. The snapshots from the simulation are given in Figure 6.24.
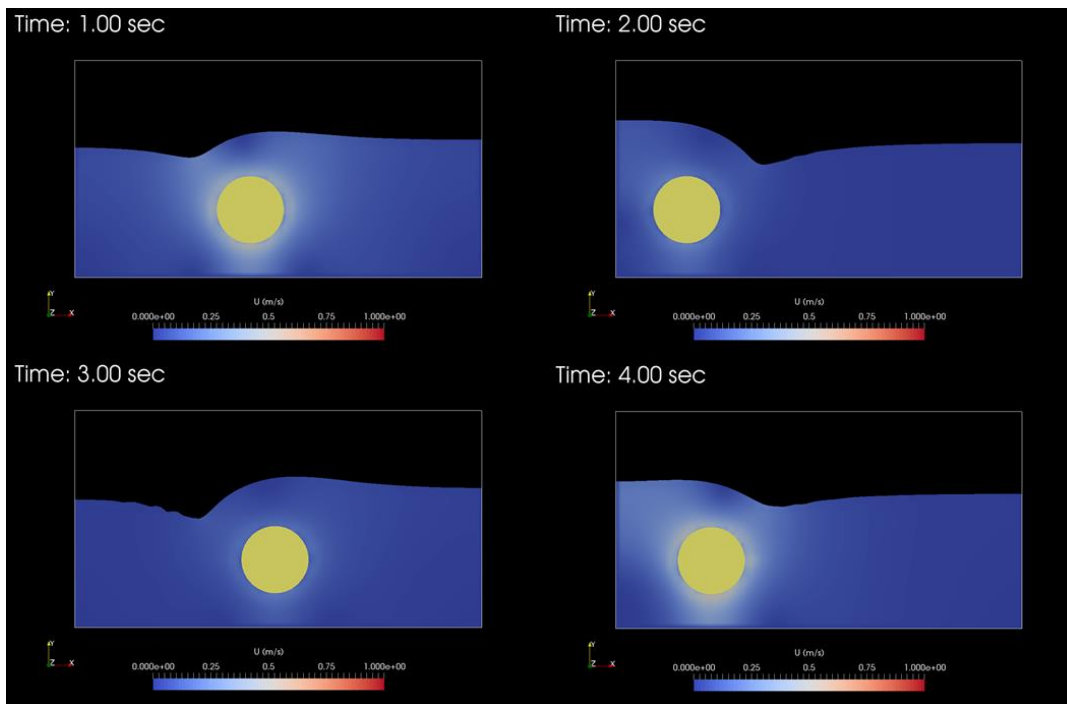
Figure 6.24. Snapshots from the test case presenting the velocity field

In Figure 6.24, it is observed that the free-surface changes according to the movement of the cylinder. Although there is no comparison with any experimental/analytical data, the shape of free-surface follows an acceptable pattern.

6.2.2　Validation Study: Sinking of a Cylinder with Free-Surface

In this validation study, an analytical solution to the "sinking of cylinder with free-surface" problem given by Tyvand and Miloh (1995) is used. Previously, this analytical data used to validate numerical models described by Lin (2007) and Mnasri et al. (2010). In the analytical solution, the boundaries of the domain are taken as infinitely long. In the validation study, a computational domain similar to the ones used in Lin (2007) and Mnasri et al. (2010) is constructed which is sufficiently long. The computational domain is 40 m in length (x-direction) and 24 m in height (y-direction), as presented in Figure 6.25. A constant mesh size of 5 cm is used along both x- and y- direction revealing 384000 cells in total. A GCI analysis

is also performed where the maximum GCI is found to be as 0.5% which is acceptable.
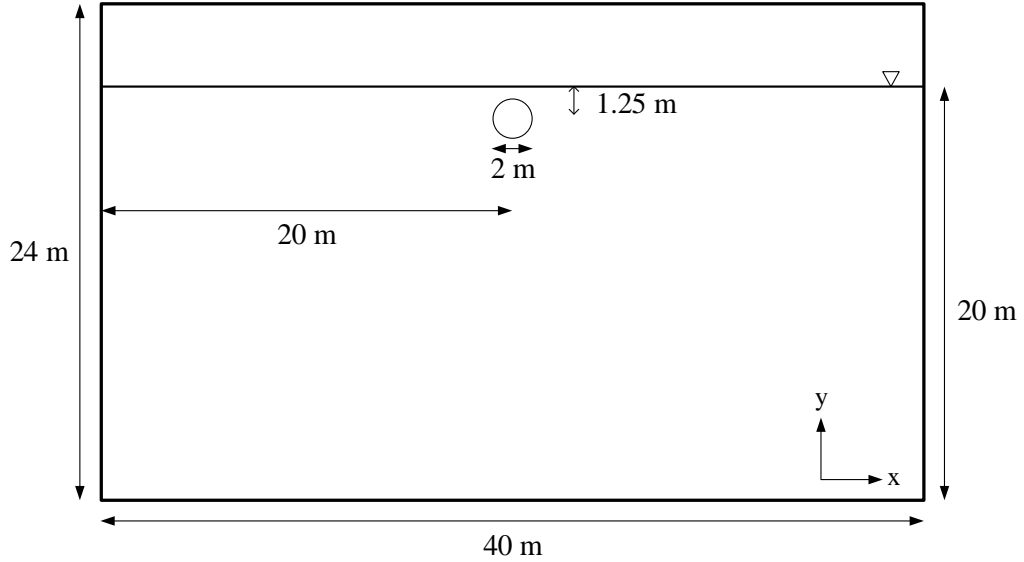
Figure 6.25. Dimensions of the computational domain

The cylinder is moving with a constant velocity (*V*) of 0.39 m/s, and the gravitational acceleration is taken as g=1 m/s^2 in the negative y-direction. The diameter of the cylinder is 2 m. The water depth is set as 24 m. The results are given in terms of *T* which is the non-dimensional time parameter given by Equation 6.6.

$$T = \frac{Vt}{d_{center}}$$

Eq. 6.6

In Equation 6.6, *t* is time and d_{center} is the distance between the center of the cylinder and the free-surface which is 1.25 m. The analytical data is only available at *T=0.4*; therefore, the simulation is carried out until *T=0.4*. The required computational time is approximately 24 hours on a single thread (Intel® Xeon® E5-2630 v4 2.2 GHz with 64 GB RAM). Snapshots from the simulation are given in Figure 6.26.
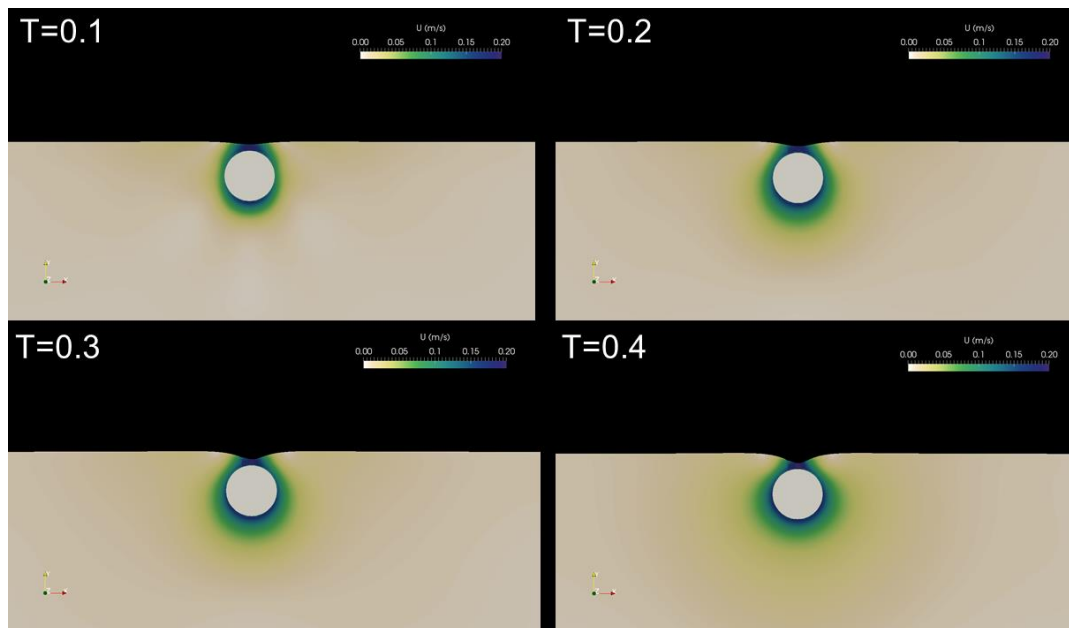
Figure 6.26. Snapshots from the validation case presenting the velocity field

In Figure 6.26, it is observed that the free-surface is deforming as the cylinder sinks. The velocity field around the cylinder is also presented in this figure. The magnitude of the velocity around the cylinder is starting from 0.39 m/s and decreasing towards 0. In Figure 6.27, the comparison of the numerical and analytical solution at T=0.4 is presented.
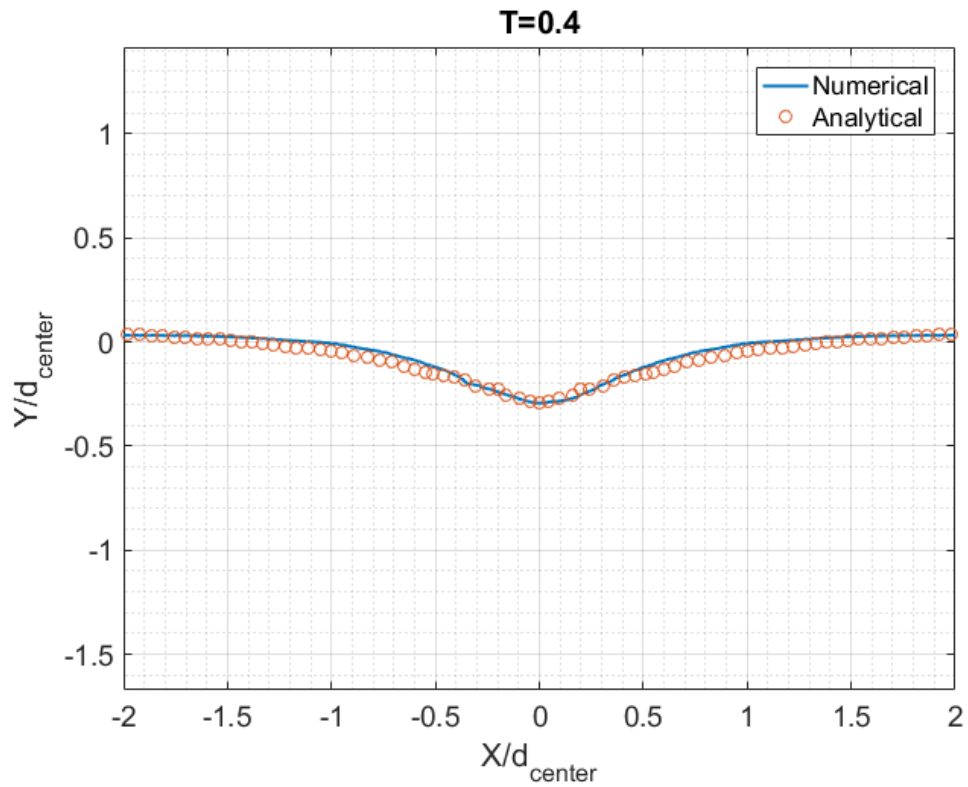
Figure 6.27. Comparison of numerical (blue solid line) and analytical results (orange circles)

It is observed in Figure 6.27 that the numerical results and the analytical results are in a good agreement. Therefore, it can be concluded that rubbleFoam is validated in scope of this validation study.

CHAPTER 7

CONCLUSIONS AND FUTURE RECOMMENDATIONS

"Great hopes, little truths."

A. H. Tanpınar, The Time Regulation Institute

The major focus of this thesis study is the CFD modelling of wave-structure interaction. In addition to that, several physical model experiments were carried to understand the physics behind these problems and to form experimental datasets for the validation of the numerical models.

In the first part of the study (Chapter 3 and Chapter 4), available numerical models were applied to the selected problems stressing the strengths and weaknesses of these models. Furthermore, the physical model experiments conducted within the scope of these chapters were presented in detail. Recommendations for practical engineering applications were also given.

In the second part of the study (Chapter 5 and Chapter 6), the development and validation of the two CFD solvers based on the immersed boundary method were described.

Although the conclusions are given previously at the end of each chapter, the highlights and novelties of this thesis study are itemized below to give an overall impression of the results:

- The experimental and numerical assessment studies on the rubble mound breakwater of Haydarpaşa Port under tsunami attack show that it is relevant to use both solitary waves and tsunami overflow to represent tsunamis in a wave flume. Both experimental and numerical studies are examples of the

limited number of studies in this topic. In these studies, it is concluded that the major failure mechanism of Haydarpaşa Breakwater is the sliding of the crown-wall of the breakwater. Furthermore, the stability of the stones located at the harbour side of the breakwater is also significant for the failure mechanism, as these stones support the crown-wall.

- The numerical model IHFOAM based on the OpenFOAM CFD library is capable of replicating the physical model experiments in general. According to the numerical results, design recommendations for rubble mound breakwaters are presented in the scope of the stability of the single stone located at the harbour side of the breakwater. However, the damage along the cross-section of the breakwater can only be evaluated qualitatively with this numerical model, as it does not solve the motion and collision of the structural units. Therefore, it is stressed that a numerical model is required to handle the motion and collision of the structural units of a rubble mound breakwater.

- As a next step, an experimental and numerical study was carried out on the motion and collision of the spherical particles under solitary wave attack, which is the first study in this context. A non-resolving CFD-DEM numerical model called CADMAS-2VF-DEM is used in the numerical simulations. The DEM part of this model is slightly modified. Although the experimental and numerical results are in agreement to a certain extent, there is still a need for improvement that might be achieved by resolving the flow properties around the particle in detail at the CFD solver part that is referred to as resolving CFD solver. Thus, this CFD solver can be strongly coupled to a DEM model.

- A resolving CFD solver can be developed using the immersed boundary method. As a first attempt, ibmPorFoam is developed working around stationary solid boundaries, which is a numerical model based on the body-force immersed boundary method solving VARANS equations to account for the porous media flow. In this numerical model, free-surface is captured using the VOF method applying two different algorithms which are MULES

144

and isoAdvector. It is the first time that isoAdvector algorithm is used with the IBM and within the porous media.

- ibmPorFoam is validated against four experimental datasets. The results show that ibmPorFoam is capable of replicating these experiments with either using MULES or isoAdvector algorithms to apply the VOF method. Furthermore, the accuracy of the model is consistent with IHFOAM, which is working on conventional body-fitted mesh configurations.

- The questions related to the use of the new algorithms within the framework of ibmPorFoam are also discussed. One of the important results that should be highlighted is that the isoAdvector algorithm does not have a clear improvement compared to the MULES algorithm when the solitary waves and dam-break flow are considered.

- In the validation studies of ibmPorFoam, an extended study is also carried out on the numerical prediction of the impact pressures. It is shown that there is no significant effect of the discretization scheme of the convection term and air compressibility (as the trapped air is not compressed) for the selected case study. However, it is observed that the turbulence modelling can be significantly effective for the selected case study.

- As it is seen that the body-force immersed boundary method is not robust enough for the moving boundaries and does not resolve the boundary layers around the solid boundaries accurately, another CFD model called rubbleFoam is developed based on the cut-cell immersed boundary method for moving boundaries solving VARANS equations to account for the porous media flow. To the author's knowledge, this numerical model is the first example that considers the moving boundaries, porous media flow, free-surface capturing and wave generation/absorption at the same time.

- rubbleFoam is validated against an analytical solution concerning sinking of a circular cylinder. It is seen that rubbleFoam is capable of capturing free-surface accurately when there is a moving body in the computational domain moving with a constant velocity.

This study is believed to be a humble attempt to evaluate the available tools and put a step forward in the numerical modelling of wave-structure interaction problems. However, there exist several drawbacks of this study stated throughout the chapters. Based on these drawbacks, several recommendations are given below as items that may constitute a future research agenda:

- It is discussed that there is a difficulty in the implementation of wall functions for the body-force IBM, as the wall surface is implicit in this method. This issue should be studied to find a way to implement wall functions.

- The studies on the numerical prediction of the impact pressures should be extended with the use of other appropriate experimental datasets. These datasets should involve all the elementary loading processes affecting the impact pressures.

- The number of validation cases for rubbleFoam is not satisfactory. rubbleFoam should be tested with new experimental datasets. As there is a lack of experimental data appropriate for these tests, relevant physical model experiments should be designed and conducted to form a dataset.

- It is not clear that why MULES or isoAdvector algorithms do not work with rubbleFoam. This issue should be investigated.

- rubbleFoam is ready to be coupled with a DEM model. The coupled version of this model can be validated against the experimental dataset given by Goral et al. (2020) in addition to the physical model experiments presented in this thesis study. The results of the numerical modelling studies conducted with CADMAS-2VF-DEM should be compared with the coupled version of rubbleFoam to quantify the change in the accuracy of the predictions.

REFERENCES

Aniel-Quiroga, I., Vidal, C., Lara, J. L. and Gonzalez, M. 2019. Pressures on a Rubble-Mound Breakwater Crown-Wall for Tsunami Impact, Coastal Engineering 152:103533.

Aniel-Quiroga, I., Vidal, C., Lara, J. L., Gonzalez, M. and Sainz, A. 2018. Stability of Rubble-Mound Breakwaters under Tsunami First Impact and Overflow Based on Laboratory Experiments, Coastal Engineering 135:39-54.

Arikawa, T. and Igarashi, H. 2018. Consideration on Accuracy and Computational Efficiency of Gas-Liquid Two-Phase Fluid Simulation Against Tsunami Bore Force, Journal of Japan Society of CivilEngineers, Ser. B2 (Coastal Engineering), Vol 74-2. (in Japanese)

Arikawa, T., Akiyama, M. and Yamazaki, N. 2011. Development of Solid-Gas-Liquid Coupling System by using CADMAS-SURF/3D, J. of JSCE, Ser. B2 (Coastal Engineering), 67, 2 (in Japanese).

Arikawa, T., Sato, M., Shimosako, K., Hasegawa, I., Yeom, G. S., Tomita, T. 2012. Failure Mechanism of Kamaishi Breakwaters due to the Great East Japan Earthquake Tsunami, International Conference on Coastal Engineering (ICCE) Proceedings, COPRI, ASCE.

Arikawa, T., Yamano, T. and Akiyama, M. 2007. Advanced Deformation Method for Breaking Waves by Using CADMAS-SURF/3D, Annual Journal of Coastal Engineering JSCE 54:71-75 (in Japanese).

Aydın, I. 2016. Unpublished Lecture Notes on Computational Fluid Dynamics Techniques (CE580), METU Department of Civil Engineering.

Aytore, B. 2015. Assessment of Tsunami Resilience of Ports by High Resolution Numerical Modelling: A Case Study for Haydarpaşa Port in the Sea of Marmara, MSc Thesis, METU.

Aytore, B., Yalciner, A. C., Zaytsev, A., Cankaya, Z. C. and Suzen, M. L. 2016. Assessment of Tsunami Resilience of Haydarpasa Port in the Sea of Marmara by High-Resolution Numerical Modelling, Earth Planets and Space, 68:139.

Azadbakht, M. and Yim, S. 2014. Simulation and Estimation of Tsunami Loads on Bridge Superstructures, Journal of Waterway, Port, Coastal, Ocean Eng., 141 (2) 04014031.

Barnocky, G. and Davis, R. 1988. Elastohydrodynamic Collision and Rebound of Spheres: Experimental Verification, Physics of Fluids, 31, 1324-1329.

Berberovic, E., van Hinsberg, N., Jakirlic, S., Roisman, I. and Tropea, C.. 2009. Drop Impact onto a Liquid Layer of Finite Thickness: Dynamics of the Cavity Evolution, Physical Review E 79:036306.

Bihs, H. and Kamath, A. 2017. A Combined Level-Set/Ghost-Cell Immersed Boundary Representation for Floating Body Simulations, International Journal for Numerical Methods in Fluids 83:905-916.

Bilger, C., Aboukhedr, M., Vogiatzaki, K. and Cant, R.S. 2017. Evaluation of Two-phase Flow Solvers using Level Set and Volume of Fluid Methods, Journal of Computational Physics, 345, 665-686.

Bricker, J. D. and Nakayama, A. 2014. Contribution of Trapped Air, Deck Superelevation and Nearby Structures to Bridge Deck Failure during a Tsunami, Journal of Hydraulic Engineering 40(5), 05014002-1-7.

Bricker, J. D., Takagi, H. and Mitsui, J. 2013. Turbulence Model Effects on VOF Analysis of Breakwater Overtopping during the 2011 Great East Japan Tsunami, in Proceedings of 35th IAHR World Congress, Chengdu, Sichuan, China.

Broderick, L. L. 1984. Riprap Stability versus Monochromatic and Irregular Waves, MSc Thesis, George Washington University, USA.

Buhmann, M. D. 2003. Radial Basis Functions: Theory and Implementations. Cambridge: Cambridge University Press.

Burcharth, H. and Andersen, O. 1995. On the One-Dimensional Steady and Unsteady Porous Flow Equations, Coastal Engineering 24:233-257.

Canelas, R.B., Crespo, A.J.C., Dominguez, J.M., Ferreira, R.M.L. and Gomez-Gesteira, M. 2016. SPH-DCDEM Model for Arbitrary Geometries in Free Surface Solid-Fluid Flows, Computer Physics Communications, 202, 131-140.

Chella, M., Bihs, H., Myrhaug, D. and Muskulus, M. 2017. Breaking Solitary Waves and Breaking Wave Forces on a Vertically Mounted Slender Cylinder over an Impermeable Sloping Seabed, Journal of Ocean Engineering and Marine Energy 3:1-9.

CIRIA, CUR and CETMEF. 2007. The Rock Manual: The Use of Rock in Hydraulic Engineering 2nd Edition, C683, CIRIA, London.

Davis, R., Rager, D. and Good, B. 2002. Elastohydrodynamic Rebound of Spheres from Coated Surfaces, Journal of Fluid Mechanics, 468, 107-119.

Davis, R., Serayssol, J. and Hinch, E. 1986. The Elastohydrodynamic Collision of Two Spheres, Journal of Fluid Mechanics, 163, 479-497.

Dean, R.G. and Dalyrmple, R.A. Water Wave Mechanics for Engineers and Scientists (1st Edition), Singapore: World Scientific.

del Jesus, M., Lara, J. L. and Losada, I. J. 2012. Three-Dimensional Interaction of Waves and Porous Structures. Part I: Numerical Model Formulation, Coastal Engineering 64:57–72

Dentale, F., Donnarumma, G. and Carratelli, E. P. 2014a. Numerical Wave Interaction with Tetrapods Breakwater, International Journal of Naval Architecture and Ocean Engineering 6 (4):800-812.

Dentale, F., Donnarumma, G. and Carratelli, E. P. 2014b. Rubble Mound Breakwater: Run-Up, Reflection and Overtopping by Numerical 3D Simulation, Coasts, Marine Structures and Breakwaters 2013: From Sea to Shore – Meeting the Sea 2:1164-1173.

Deshpande, S.S., Anumolu, L. and Trujillo, M. F. 2012. Evaluating the Performance of the Two-Phase Flow Solver interFoam, Computational Science and Discovery 5 (1):014016.

Dias, F. and Ghidaglia, J.M. 2018. Slamming: Recent Progress in the Evaluation of Impact Pressures, Annual Review of Fluid Mechanics, 50:243-73.

Donahue, C., Hrenya, C. and Davis, R. 2010a. Stokes's Cradle: Newton's Cradle with Liquid Coating, Physics Review Letters, 105, 034501.

Donahue, C., Hrenya, C., Davis, R., Nakagawa, K., Zelinskaya, A. and Joseph, G. 2010b. Stoke's Cradle: Normal Three-Body Collisions between Wetted Particles, Journal of Fluid Mechanics, 650, 479.

Engelund, F. 1953. On the Laminar and Turbulent Flow of Ground Water Through Homogeneous Sand, Transactions of the Danish Academy of Technical Sciences 3.

Esteban, M., Jayaratne, R., Mikami, T., Morikubo, I, Shibayama, T., Thao, N. D., Ohira, K., Ohtani, A., Mizuno, Y., Kinoshita, M. and Matsuba, S. 2013. Stability of Breakwater Armor Units against Tsunami Attacks, Journal of Waterway, Port, Coastal and Ocean Engineering 140 (2):188-198.

Fenton, J.D. 1988. The Numerical Solution of Steady Water Wave Problems, Computers and Geosciences, 14(3), 357-368.

Ferziger, J.H. and Peric, M. 2002. Computational Methods for Fluid Dynamics 3rd Edition, Springer.

Foam-extend. 2020. The Open-Source CFD Toolbox by Wikki Ltd. version 4.1, foam-extend Team http://www.foam-extend.org.

Gondret, P., Hallouin, E., Lance, M. and Petit, L. 1999. Experiments on the Motion of A Solid Sphere Toward a Wall: From Viscous Dissipation to Elastohydrodynamic Bouncing, Physics of Fluids, 11, 2803-2805.

Gondret, P., Lance, M. and Petit, L. 2002. Bouncing Motion of Spherical Particles in Fluids, Physics of Fluids, 14, 643-652.

Goral, K. D., Guler, H. G., Baykal, C. and Yalciner, A. C. 2020. An Experimental Study on the Motion of Solid Spheres under Solitary Wave Attack. (under review)

Goring, D. G. 1979. Tsunamis – The Propagation of Long Waves onto Shelf, PhD Dissertation, California Institute of Technology, Pasedane, California, USA.

Grigoriadis, D. G. E., Dimas, A. A. and Balaras, E. 2012. Large-Eddy Simulation of Wave Turbulent Boundary Layer Over Rippled Bed, Coastal Engineering: 174-189.

Guler, H. G., Arikawa, T., Baykal, C., Goral, K. D. and Yalciner, A.C. 2018b. Motion of Solid Spheres Under Solitary Wave Attack: Physical and Numerical Modelling, International Conference on Coastal Engineering (ICCE) Proceedings 2018, Baltimore, USA.

Guler, H. G., Liu, X., Jensen, B., Tomaselli, P. D., Baykal, C., Arikawa, T. and Yalciner, A. C. 2018c. A New Numerical Flow Solver for Simulating Porous Media Flow Based on Immersed Boundary Method, AGU Fall Meeting 2018, Washington D.C., USA.

Guler, H.G., Arikawa, T., Aytore, B., Tomita, T., Zaytsev, A. and Yalciner, A.C. 2014. High Performance Computing for Comparing the Performance of 2D/3D Hybrid Tsunami Simulation Models: A Case Study in Haydarpaşa Port in Istanbul, the Sea of Marmara, Asia Ocenia Geosciences Society (AOGS) General Assembly 2014, Sapporo, Japan.

Guler, H.G., Arikawa, T., Oei, T., Yalciner, A. C. 2015. Performance of Rubble Mound Breakwaters Under Tsunami Attack, a Case Study: Haydarpasa Port, Istanbul, Turkey, Coastal Engineering 104:43-53.

Guler, H.G., Baykal, C., Arikawa, T., Yalciner, A. C.2018a. "Numerical Assessment of Tsunami Attack on a Rubble Mound Breakwater using OpenFOAM®." Applied Ocean Research 72:76-91.

Harbitz, C. B., Nakamura, Y., Arikawa, T., Baykal, C., Dogan, G. G., Frauenfelder, R., Glimsdal, S., Guler, H. G., Issler, D., Kaiser, G., Kanoglu, U., Kisacik, D., Kortenhaus, A., Lovholt, F., Maruyama, Y., Sassa, S., Sharghivand, N., Strusinska-Correia, A., Ozyurt Tarakcioğlu, G. and Yalciner, A. C. 2016. Risk Assesment and Design Prevention Structures for Enhanced Tsunami Disaster Resilience (RAPSODI)/Euro-Japan Collaboration, Coastal Engineering Journal 58 (4).

Heisenberg, W. 1927. Ueber den Anschaulichen Inhalt der Quantentheoretischen Kinematik und Mechanik, Zaitschrift für Physik, 43:172-198. English translation in Wheeler and Zurek (1983).

Higuera, P. 2015. Application of Computational Fluid Dynamics to Wave Action on Structures, PhD diss., Doctoral Thesis, Universidad de Cantabria.

Higuera, P., Lara, J. L. and Losada, I. J. 2013. Realistic Wave Generation and Active Wave Absorption for Navier–Stokes Models: Application to OpenFOAM, Coastal Engineering 71:102–118

Higuera, P., Lara, J. L. and Losada, I. J. 2014a. Three–Dimensional Interaction of Waves and Porous Coastal Structures using OpenFOAM Part I: Formulation and Validation, Coastal Engineering 83:243-258.

Higuera, P., Lara, J. L. and Losada, I. J. 2014b. Three–Dimensional Interaction of Waves and Porous Coastal Structures using OpenFOAM Part II: Application, Coastal Engineering 83:259–270.

Hirt, C. W. and Nichols, B. D. 1981. Volume of Flud (VOF) Method for Dynamics of Free Boundaries, Journal of Computational Physics 39:201-225.

Hsiao, S. C. and Lin, T-C. 2010. Tsunami-like Solitary Waves Impinging and Overtopping an Impermeable Seawall: Experiment and RANS Modelling, Coastal Engineering 57:1-18.

Hudson, R. Y. 1959. Laboratory Investigations of Rubble Mound Breakwaters, WES Report, Vicksburg, Mississippi, USA.

Hydralab. 2017. Guidelines for Wave Modelling in Flumes and Basins: Hydraulic Model Testing in Waves, DHI, Denmark.

Isobe, M., Takahashi, S., Yu, S.P., Sakakiyama, T., Fujima, K., Kawasaki, K., Jiang, Q., Akiyama, M. and Oyama, H. 1999. Interim Report on Development of Numerical Wave Flume for Maritime Structure Design, Proceedings of Civil Eng. in the Ocean, 15, 321-326 (in Japanese).

Issa, R. I. 1986. Solution of Implicitly Discretized Fluid Flow Equations by Operator-Splitting, Journal of Computational Physics 62:40-65.

Itoh, K., Higuchi, Y., Toue, T. and Katsui, H. 2002. Numerical Simulation of Rubble Structures by DEM and VOF, Proceedings of the 12. ISOPE, Kitakyushu, Japan, May 26-31.

Jacobsen, N. G., Fuhrman, D. R. and Fredsoe, J. 2012. A Wave Generation Toolbox for the Open-Source CFD Library: OpenFOAM®, International Journal for Numerical Methods in Fluids 70:1073-1088.

Jasak, H. 2018. Immersed Boundary Surface Method in Foam-Extend, The 13th OpenFOAM Workshop, Shanghai, China.

Jasak, H., Rigler, D and Tukovic, Z. 2014. Design and Implementation of Immersed Boundary Method with Discrete Forcing Approach for Boundary Conditions, 11th World Congress on Computational Mechanics, 5th European Conference

on Computational Mechanics, 6th European Conference on Computational Fluid Dynamics, (eds) E. Onate, J. Oliver and A. Huerta.

Jensen, B. 2014. Wave Interaction with Porous Coastal Structures, Ph.D. diss., Technical University of Denmark.

Jensen, B., Jacobsen, N. G. and Christensen, E. D. 2014. Investigations on the Porous Media Equations and Resistance Coefficients for Coastal Structures, Coastal Engineering 84:56-72.

Jensen, B., Liu, X., Christensen, E.D., Roenby, J. 2017. Porous Media and Immersed Boundary Hybrid Modelling for Simulating Flow in Stone Cover-Layers, Paper presented at Coastal Dynamics 2017, Helsingoer, Denmark, June 12-16.

Joseph, G. 2003. Collisional Dynamics of Macroscopic Particles in a Viscous Fluid, PhD Dissertation, California Institute of Technology, Pasedana, California, USA.

Joseph, G., Zenit, R., Hunt, M. and Rosenwinkel, A. 2001. Particle Wall Collisions in a Viscous Fluid, Journal of Fluid Mechanics, 433, 329-346.

Kempe, T. and Fröhlich, J. 2012. Collision Modelling for the Interface-Resolved Simulation of Spherical Particles in Viscous Fluids, Journal of Fluid Mechanics, 709, 445-489.

Khayyer, A., Gotoh, H., Shimizu, Y., Gotoh, K., Falahaty, H. and Shao, S. 2018. Development of a Projection-Based SPH Method for Numerical Wave Flume with Porous Media of Variable Porosity, Coastal Engineering 140:1-22.

Kleefsman, K. M. T., Fekken, G., Veldman, A. E. P., Iwanowski, B. and Buchner, B. 2005. A Volume-of-Fluid Based Simulation Method for Wave Impact Problems, Journal of Computational Physics 206:363-393.

Kobayashi, N. and Greenwald, J. H. 1986. Prediction of Wave Run-up and Riprap Stability, International Conference on Coastal Engineering (ICCE) Proceedings, COPRI, ASCE.

Kobayashi, N. and Otta, A. 1987. Hydraulic Stability Analysis of Armor Units, Journal of Waterway, Port, Coastal and Ocean Engineering 113 (2).

Laplace, P. S. M. 1820. Theorie Analyique des Probabilities, Paris: Couvier.

Lara, J.L., Garcia, N. and Losada, I.J. 2006. RANS Modelling Applied to Random Wave Interaction with Submerged Permeable Structures, Coastal Engineering, 53, 395-417.

Larsen, B. E. and Fuhrman, D. R. 2018. On the Over-Production of Turbulence Beneath Surface Waves in Reynolds-Averaged Navier-Stokes Models, Journal of Fluid Mechanics 853:419-460.

Larsen, B. E., Fuhrman, D. R. and Roenby, J. 2019. Performance of interFoam on the Simulation of Progressive Waves, Coastal Engineering Journal 61 (3):380-400.

Larsen, B. E., Fuhrman, D. R., Baykal, C. and Sumer, B. M. 2017. Tsunami-Induced Scour around Monopile Foundations, Coastal Engineering 129:36-49.

Latham, J. P., Anastasaki, E. and Xiang, J. 2013. New Modelling and Analysis Methods for Concrete Armour Unit Systems using FEMDEM, Coastal Engineering 77:151-166.

Lee, J. J., Skjelbreia, E. and Raichlen, F. 1982. Measurement of Velocities in Solitary Waves, Journal of Waterway, Port, Coastal, and Ocean Engineering 108:200–218.

Lin, P. 1998. Numerical Modeling of Breaking Waves, PhD diss., Cornell University.

Lin, P. 2007. A Fixed-Grid Model for Simulation of a Moving Body in Free Surface Flows, Computers&Fluids 36:549-561.

Liu, P., Lin, P., Chang, K. and Sakakiyama, T. 1999. Numerical Modelling of Wave Interaction with Porous Structures, Journal of Waterway, Port, Coastal, and Ocean Engineering 125:322-330.

Liu, X. 2013. Realistic Flow Simulations Around and Inside Porous Scour Protections, Paper presented at 35th International Association for Hydro-Environment Engineering and Research Congress, Chengdu, China, September 8-13.

Liu, X. 2014. A New Immersed Boundary Method for Simulating Free Surface Flows Around Arbitrary Objects, Paper presented at 7th International Conference on Fluvial Hydraulics "River Flow 2014", Lausanne, Switzerland, September 3-5.

Losada, I. J., Gonzalez-Ondina, J. M., Diaz, G. and Gonzalez, E. M. 2008. Numerical Simulation of Transient Non-Linear Response of Semi-Enclosed Water Bodies: Model Description and Experimental Validation, Coastal Engineering 55 (1):21-34.

Losada, I.J., Lara, J.L. and del Jesus, M. 2016. Modelling the Interaction of Water Waves with Porous Coastal Structures, Journal of Waterway, Port, Coastal and Ocean Engineering, 142-6.

Madsen, P. and Fuhrman, D. R. 2008. Run-Up of Tsunamis and Long Waves in terms of Surf-Similarity, Coastal Engineering 55:209-223.

Madsen, P., Fuhrman, D. R. and Schaffer, H. A. 2008. On the Solitary Wave Paradigm for Tsunamis, Journal of Geophysical Research 113.

Malek-Mohammadi, S. and Testik, F. Y. 2010. New Methodology for Laboratory Generation of Solitary Waves, Technical Note, Journal of Waterway, Port, Coastal and Ocean Engineering 136 (5).

McKee, S., Tom, M. F., Ferreira, V. G., Cuminato, J. A., Castelo, A., Sousa, F. and Mangiavacchi, N. 2008. The MAC Method, Computers and Fluids 37:907-930.

McLaughin, M. 1968. An Experimental Study of Particle-Wall Collision Relating to Flow of Solid Particles in Fluid, MSc Thesis, California Institute of Technology, Pasedana, California, USA.

Mendez, F.J., Losada, I.J. and Losada, M.A. 2001. Wave-induced Mean Magnitudes in Permeable Submerged Breakwater, Journal of Waterway, Port, Coastal and Ocean Engineering, 127, 7-15.

Menter, F. 1994. Two-Equation Eddy-Viscosity Turbulence Models for Engineering Applications, AIAA Journal 32:1598-1605.

Mirjalili, S., Jain, S. S. and Dodd, M.S. 2017. Interface-Capturing Methods for Two-Phase Flows: An Overview and Recent Developments, Center for Turbulence Research Annual Research Briefs 2017.

Mittal, R. And Iaccarino, G. 2005. Immersed Boundary Methods, Annual Review of Fluid Mechanics, 37:39-261.

Mnasri, C., Hafsia, Z., Omri, M. and Maalel, K. 2010. A Moving Grid Model for Simulation of Free-Surface Behaviour Induced by Horizontal Cylinders Exit and Entry, Engineering Applications of Computational Fluid Mechanics 4(2):260-275.

Moukalled, F., Mangani, L. and Darwish, M.. 2012. The Finite Volume Method in Computational Fluid Dynamics: An Advanced Introduction with OpenFOAM® and Matlab®, Fluid Mechanics and Its Applications Book Series Vol. 113, Switzerland: Springer.

Nasr-Azadani, M. M. and Meiburg, E. 2011. TURBINS: An Immersed Boundary, Navier–Stokes Code for the Simulation of Gravity and Turbidity Currents Interacting with Complex Topographies, Computers & Fluids 45 (1):14–28.

Nielsen, A. W., Liu, X., Sumer, B. M. and Fredsøe, J. 2013. Flow and Bed Shear Stresses in Scour Protections Around a Pile in a Current, Coastal Engineering 72:20–38.

Norouzi, H. R., Zarghami, R., Sotudeh-Gharebagh, R. and Mostoufi, N. 2016. Coupled CFD-DEM Modelling: Formulation, Implementation and Application to Multiphase Flows, Wiley.

OpenFOAM®. 2012. The Open-Source CFD Toolbox version 2.1.1, OpenFOAM® Team http://www.openfoam.org.

OpenFOAM®. 2017. The Open-Source CFD Toolbox version 1706 by ESI-OpenCFD. OpenCFD Team. http://www.openfoam.com.

Pedersen, J. 1996. Wave Forces and Overtopping on Crown Walls of Rubble Mound Breakwaters: An Experimental Study, PhD Thesis, Aalborg University.

Peng, W., Lee, K. H. and Mizutani, N. 2012. Application of Direct-Forcing IB-VOF Method to the Simulation of Wave Deformation by Submerged Structures, Journal of Coastal Research 28 (3):658-670.

Peskin, C. S. 1972. Flow Patterns Around Heart Valves: A Numerical Method, Journal of Computational Physics 10 (2): 252-271.

Petit, H. A. H., Tonjes, P., van Gent, M. R. A. and van den Bosch, P. 1994. Numerical Simulation and Validation of Plunging Breakers Using a 2D Navier-Stokes Model, International Conference on Coastal Engineering (ICCE) Proceedings, Kobe, Japan, October 23-28.

Pianet, G., Ten Cate, A., Derksen, J. and Arquis, E. 2007. Assessment of the 1-Fluid Method for DNS of Particulate Flows: Sedimentation of a Single Sphere at Moderate to High Reynolds Numbers, Computer and Fluids, 36, 359-375.

Press, W., Teukolsky, S., Vetterling, W. and Flannery, B. 1990. Numerical Recipes: The Art of Scientific Computing, Cambridge: Cambridge University Press.

Pringle, W. J., Yoneyama, N. and Mori, N. 2016. Two-way Coupled Long Wave-RANS Model: Solitary Wave Transformation and Breaking on a Plane Beach, Coastal Engineering 114:96-118.

Roache, P. J. 1998. Verification of Codes and Calculations, AIAA Journal 36-5.

Roenby, J., Bredmose, H. and Jasak, H. 2016. A Computational Method for Sharp Interface Advection, Royal Society of Open Science 3 (11):160405.

Sainflou, G. 1928. Essai sur les Digues Maritime Verticales, Annual Ponts et Chaussees 98 (1):5-48.

Sakayima, T. 2013. Flow Fields of Tsunamis Passing on Rubble Mound Breakwater, Proceeding of the 23rd ISOPE, Alaska, USA.

Salem, H., Mohssen, S., Kosa, K. and Hosoda, A. 2014. Collapse Analysis of Utatsu Ohashi Bridge Damaged by Tohoku Tsunami using Applied Element Method, Journal of Advanced Concrete Technology 12:388-402.

Sarfaraz, M. and Pak, A. 2017. An Integrated SPH-Polyhedral DEM Algorithm to Investigate Hydraulic Stability of Rock and Concrete Blocks: Applications to Cubic Armors in Breakwaters, Engineering Analysis with Boundary Elements 84:1-18.

Schäffer, H.A. and Klopman, G. 2000. Review of Multidirectional Active Wave Absorption Methods, Journal of Waterway, Port, Coastal, and Ocean Engineering 126:88–97.

Sethian, J. A. 1999. Level-Set Methods and Fast Marching Methods: Evolving Interface in Computational Geometry, Mechanics, Computer Vision and Materials Science. Cambridge University Press.

Shen, L. and Chan, E.S. 2008. Numerical Simulation of Fluid-Structure Interaction using a Combined Volume of Fluid and Immersed Boundary Method, Ocean Engineering 35:939-952.

Skjelbreja, L. and Hendrickson, J.A. 1960. Fifth-order Gravity Wave Theory, Proceedings of Coastal Engineering Conference, 184-196.

St-Germain, P., Nistor, I., Townsend, R. and Shibayama, T. 2014. Smoothed-Particle Hydrodynamics Numerical Modelling of Structures Impacted by Tsunami Bores, Journal of Waterway, Port, Coastal and Ocean Engineering 140 (1): 66-81.

Stolle, J., Nistor, I. and Goseberg, N. 2016. Optical Tracking of Floating Shipping Containers in a High-Velocity Flow, Coastal Engineering Journal 58(2) 1650005.

Sun, R. and Xiao, H. 2016. Sedifoam: A General-Purpose Open-Source CFD-DEM Solver for Particle-Laden Flow with Emphasis on Sediment Transport, Computers and Geosciences, 89, 207-219.

Suzuki, T. and Arikawa, T. 2010. Numerical Analysis of Bulk Drag Coefficient in Dense Vegetation by Immersed Boundary Method, International Conference on Coastal Engineering (ICCE) Proceedings, Shangia, China, June 30-July 5.

Svendsen, I.A. 2006. Introduction to Nearshore Hydrodynamics. Singapore: World Scientific.

Synolakis, C. E. 1990. Generation of Long Waves in Laboratory, Journal of Waterway, Port, Coastal and Ocean Engineering 116 (2):252-266.

Ten Cate, A., Nieuwstad, C., Derksen, J. and Den Akker, H.V. 2002. Particle Imaging Velocimetry Experiments and Lattice-Boltzmann Simulations on a Single Sphere Settling under Gravity, Physics of Fluids, 14, 4012-4025.

Tezduyar, T. E. 2001. Finite Element Methods for Flow Problems with Moving Boundaries and Interfaces, Archives of Computational Methods in Engineering. 8:83-130.

Tryggvason, G., Scardovelli, R. and Zaleski, S. 2011. Direct Numerical Simulations of Gas-Liquid Multiphase Flows. Cambridge University Press.

Tsuji, Y., Kawaguchi, T. and Tanaka, T. 1993. Discrete Particle Simulation of Two-Dimensional Fluidized Bed, Powder Technology, 77, 79-87.

Tyvand, P.A and Miloh, T. 1995. Free-surface Flow due to Impulsive Motion of a Submerged Circular Cylinder, Journal of Fluid Mechanics 286:67-101

Udaykumar, H.S., Mittal, R. and Rampunggoon, P. 2001. A Sharp Interface Cartesian Grid Method for Simulating Flows with Complex Moving Boundaries, Journal of Computational Physics, 174, 345-380.

Van der Vorst, H. A. 1992. Bi-CGSTAB: A Fast and Smoothly Converging Variant of Bi-CG for the Solution of Nonsymmetrical Linear Systems. SIAM Journal on Scientific and Statistical Computing 13(2):631-644.

van Gent, M. R. A., Tonjes, P., Petit, H. A. H. and van den Bosch, P. 1994. Wave Action on and in Permeable Structures, International Conference on Coastal Engineering (ICCE) Proceedings, Kobe, Japan, October 23-28.

van Gent, Marcel R. A. 1995. Wave Interaction with Permeable Coastal Structures, Ph.D. diss., Technical University of Delft.

Wang, D., Shaowu, L., Arikawa, T. and Gen, H. 2016. ISPH Simulation of Scour Behind Seawall due to Continuous Tsunami Overflow, Coastal Engineering Journal 58-3.

Wei, G. and Kirby, J.T. 1995. Time-dependent Numerical Code for Extended Boussinesq Equations, Journal of Waterway, Port, Coastal and Ocean Engineering, 121 (5), 251-261.

Wheeler, J. A. and Zurek, W. H. (eds). 1983. Quantum Theory and Measurement, Princeton NJ: Princeton University Press.

Wu, Y. T. and Hsiao, S. C. 2013. Propagation of Solitary Waves over a Submerged Permeable Breakwater, Coastal Engineering 81:1–18.

Wu, Y. T., Yeh, C. L. and Hsiao, S. C. 2014. Three-Dimensional Numerical Simulation on the Interaction of Solitary Waves and Porous Breakwaters, Coastal Engineering 85:12–29.

Xu, G and Cai, C.S. 2015. Numerical Simulations of Lateral Restraining Stiffness Effect on Bridge Deck-Wave Interaction under Solitary Waves, Engineering Structures 101:337-351.

Xu, Y. and Liu, X. 2017. Effects of Different In-Stream Structure Representations in Computational Fluid Dynamic Models – Taking Engineered Log Jams (ELJ) as an Example, Water 9(2): 110.

Zenit, R. and Hunt, M. 1999. Mechanics of Immersed Particle Collisions, Trans. ASME: Journal of Fluids Engineering, 121, 179-184.

Zhang, C., Zhang, W., Lin, N., Tang, Y., Zhao, C., Gu, J., Lin, W., Chen, X. and Qiu, A. 2013. A Two-Phase Flow Model Coupling with Volume of Fluid and Immersed Boundary Methods for Free Surface and Moving Structure Problems, Ocean Engineering 74:108-124.

Zhang, J., Fan, L., Zhu, C., Pfeffer, R. and Qi, D. 1999. Dynamic Behaviour of Collision of Elastic Spheres in Viscous Fluids, Powder Technology, 106, 98-109.

CURRICULUM VITAE

PERSONAL INFORMATION

Surname, Name: Güler, Hasan Gökhan
Nationality: Turkish (TC)
Date and Place of Birth: 4 April 1989, İzmir
Marital Status: Married
Phone: +90 533 085 64 58
email: gokhann@gmail.com, goguler@metu.edu.tr

EDUCATION

Degree	Institution	Year of Graduation
MSc	METU Civil Engineering	2014
BS (Minor)	METU Mathematics	2015
BS (Major)	METU Civil Engineering	2011
High School	Muğla 75. Yıl Science High School	2006

WORK EXPERIENCE

Year	Place	Enrollment
2011-Present	METU Dept. of Civil Engineering	Research Assistant
Oct., 2017 – Nov, 2017	Chuo University, Tokyo, Japan	Guest Researcher
Oct., 2016	Chuo University, Tokyo, Japan	Guest Researcher
Dec., 2013 – Mar., 2014	Port and Airport Research Institute (PARI), Yokosuka, Japan	Guest Researcher

FOREIGN LANGUAGES

Advanced English

PUBLICATIONS

Journals

1. **Guler, H.G.,** Arikawa, T., Oei, T., Yalciner, A.C. "Performance of Rubble Mound Breakwaters under Tsunami Attack, A Case Study: Haydarpaşa Port, Istanbul, Turkey", Coastal Engineering, 104, 43-53 (2015)

2. Harbitz, C.B., Nakamura, Y., Arikawa, T., Baykal, C., Dogan, G.G., Frauenfelder, R., Glimsdal, S., **Guler, H.G.,** Issler, D., Kaiser, G., Kanoglu, U., Kisacik, D., Kortenhaus, A., Lovholt, F., Maruyama, Y., Sassa, S., Sharghivand, N., Strusinska-Correia, A., Tarakcioglu Ozyurt, G., Yalciner, A.C. "Risk Assessment and Design of Prevention Structures for Enhanced Tsunami Disaster Resilience (RAPSODI)/ Euro-Japan Collaboration", Coastal Engineering Journal, 58:4 (2016)

3. **Guler, H.G.,** Cinar, G.E., Sharghivand, N, Dogan, G.G., Necmioglu, O., Zaytsev, A., Yalciner, A.C. "Tsunami Action on Coasts and Constructions", Fundamental and Applied Geophysics (Fundamentalnaya I Prikladnaya Gidrofzika), 10, 3, 65-72 (2017)

4. **Guler, H.G.,** Ozer Sozdinler, C., Arikawa, T., Yalciner, A.C. "Structural and Non-Structural Countermeasures and Awareness Studies After Tsunami Disaster: Case of Japan", Technical Journal, 29-5, in Turkish (2018)

5. **Guler, H.G.,** Baykal, C., Arikawa, T., Yalciner, A.C. "Numerical Assessment of Tsunami Attack on a Rubble Mound Breakwater using OpenFOAM", Applied Ocean Research, 72, 76-9 (2018)

6. Dogan G.G., Annunziato, A., Papadopoulos, G., **Guler, H.G.,** Yalciner, A.C., Cakir, T.E., Ozer Sozdinler, C., Ulutas, E., Arikawa, T., Suzen, L, Guler, I., Probst, P., Kanoglu, U., Synolakis, C. "The 20th July 2017 Bodrum-Kos Tsunami Field Survey", Pure and Applied Geophysics, doi: https://doi.org/10.1007/s00024-019-02151-1 (2019)

7. **Guler, H.G.,** Ozyurt Tarakcioglu, G., Baykal, C. "Effect of Mean Water Level Variations on the Design and Performance of Rubble-Mound Coastal Protection Structures", Technical Journal, 31-3, in Turkish (2020)

International Proceedings

1. **Guler, H.G.** "A Comparative Study on Van der Meer (1988) and Van Gent et al. (2003) Stability Formulae", ASCE COPRI Ports'13 Conference Proceedings, Student Paper Competition Volume, Seattle, Washington, USA (2013)

2. **Guler, H.G.,** Ergin, A., Ozyurt, G. "A Comparative Study on Stability Formulas of Rubble Mound Breakwaters", International Conference on Coastal Engineering (ICCE) 2014 Proceedings, ASCE, Seoul, Korea (2014)

3. **Guler, H.G.,** Arikawa, T., Baykal, C., Yalciner, A.C. "Motion of Solid Spheres under Solitary Wave Attack: Physical and Numerical Modelling", International Conference on Coastal Engineering (ICCE) 2018 Proceedings, ASCE, Baltimore, USA (2018)

National Proceedings

1. **Guler, H.G.,** Ergin, A., Baykal, C., Ozyurt, G., Guler, I. "Effect of Design Water Level on Stability of Armour Layers of Rubble Mound Breakwaters", 8th National

Coastal Engineering Symposium, Turkish Chamber of Civil Engineers, Istanbul, Turkey (2014)

2. **Guler, H.G.,** Baykal, C., Ozyurt, G., Ergin, A., Guler, I., Yalciner, A.C. "Tornado Formed in Sarıgerme Region on October, 17, 2013 and Its Effects in the Local Area", 8th National Coastal Engineering Symposium, Turkish Chamber of Civil Engineers, Istanbul, Turkey (2014)

3. Cabuk, O., **Guler, H.G.,** Ozyurt Tarakcioglu, G., Guler, I., Yalciner, A.C. "Hurricane Events Observed in the Mediterranean Coast of Turkey", 9th National Coastal Engineering Symposium, Turkish Chamber of Civil Engineers, Adana, Turkey (2018)

4. Baykal, C., Ozyurt Tarakcioglu, G., Isik, E., Gozlet, M.S., **Guler, H.G.** "A Physical Modelling Study on the Stability and Overtopping Performance of an Artificial Block Revetment", 9th National Coastal Engineering Symposium, Turkish Chamber of Civil Engineers, Adana, Turkey (2018)

5. **Guler, H.G.,** Isik, E., Sharghivand, N., Baykal, C., Guler, I., Ergin, A. "Evaluation of the Performance of the Numerical Model SWASH in Simulation of Regular Wave Propagation", 9th National Coastal Engineering Symposium, Turkish Chamber of Civil Engineers, Adana, Turkey (2018)

6. Ergin, A., Karaesmen, E., **Guler, H.G.** "Development of an Open-Source Computational Tool for Evaluation of Coastal Areas using Fuzzy Logic", 9th National Coastal Engineering Symposium, Turkish Chamber of Civil Engineers, Adana, Turkey (2018)

International Abstract Accepted Presentations

1. Yalciner, A.C., Aytore, B., **Guler, H.G.,** Kanoglu, U., Duzgun, S., Zaytsev, A., Arikawa, T., Tomita, T., Ozer Sozdinler, C., Necmioglu, O., Ozel, N.M. "High Resolution Tsunami Modelling and Assessment of Harbour Resilience: A Case Study in Istanbul", European Geosciences Union (EGU) General Assembly 2014, April 27 – May 02, 2014, Vienna Austria (2014)

2. **Guler, H.G.,** Arikawa, T., Aytore, B., Tomita, T., Zaytsev, A., Yalciner, A.C. "High Performance Computing for Comparing Performance of 2D/3D Hybrid Tsunami Simulation Models: A Case Study in Haydarpasa Port in Istanbul, the Sea of Marmara", Asia Ocenania Geosciences Society (AOGS) 2014, Sapporo, Japan (2014)

3. Yalciner, A.C., Aytore, B., Cankaya, C., **Guler, H.G.,** Suzen, L., Zaytsev, A., Arikawa, T., Tomita, T. "High Resolution Tsunami Vulnerability Assessment for Coastal Utilities: Case Studies in the Sea of Marmara", American Geophysical Union Fall Meeting 2014, San Francisco, USA (2014)

4. Baykal, C., Ergin, A., Guler, I., Ozyurt, G., Yalciner, A.C., Sogut, E., **Guler, H.G.,** Dogan, G.G. "Modelling Long Term Morphological Changes with XBeach: Case

Study of Kızılırmak River Mouth, Turkey", EGU General Assembly 2015, Vienna, Austria (2015)

5. **Guler, H.G.**, Baykal, C., Ozyurt, G., Kisacik, D. "Performance of Temporal Downscaling Techniques of Wind Speed Data over Aegean Sea", EGU General Assembly 2016, Vienna, Austria (2016)

6. **Guler, H.G.**, Arikawa, T., Baykal, C., Yalciner, A.C. "Numerical Modelling of Physical Model Experiments on Rubble Mound Breakwaters under Tsunami Attack using IHFOAM", International Conference on Coastal Engineering (ICCE) 2016, Antalya, Turkey (2016)

7. **Guler, H.G.**, Ozyurt Tarakcioglu, G., Baykal, C., Ak, H., Yilmaz, M.T. "Effect of Temporal Downscaling Methods of Long Term Wind Data on the Design Wave Parameters in the Black Sea", International Conference on Coastal Engineering (ICCE) 2016, Antalya, Turkey (2016)

8. Yalciner, A.C., Annunziato, A., Papadopoulos, G., Dogan, G.G., **Guler, H.G.**, Cakir, T.E., Ozer Sozdinler, C., Ulutas, E., Arikawa, T., Suzen, L., Kanoglu, U., Guler, I., Probst, P., Synolakis, C. "The Bodrum-Kos Strong (Mw 6.6) Earthquake and Associated Tsunami of July 20, 2017: Results of Post-Event Field Surveys", International Tsunami Symposium 2017, Bali, Indonesia (2017)

9. Cinar, E.G., **Guler, H.G.**, Baykal, C., Arikawa, T., Zaytsev, A., C., Yalciner, A.C. "Comparison of 2D and 3D Models in Application to Long Wave Motion and Its Interaction with the Structures", International Tsunami Symposium 2017, Bali, Indonesia (2017)

10. Arikawa, T., **Guler, H.G.**, Yalciner, A.C. "Comparison of Human Response Against Earthquake and Tsunami", American Geophysical Union Fall Meeting 2017, New Orleans, USA (2017)

11. Cinar, E.G., **Guler, H.G.**, Arikawa, T., Baykal, C., Yalciner, A.C. "Comparison of Numerical Wave Tanks with Various Turbulence Models in Application to Long Wave Motion and Its Interaction with the Structures", International Conference on Coastal Engineering (ICCE) 2018, Baltimore, USA (2018)

12. Yalciner, A.C., Annunziato, A., Papadopoulos, G., Dogan, G.G., **Guler, H.G.**, Ozer Sozdinler, C., Ulutas, E., Arikawa, T., Suzen, L., Kanoglu, U., Guler, I., Probst, P., Synolakis, C. "The July 20, 2017 Bodrum-Kos Earthquake and Tsunami: Field Surveys, Lessons and Modelling", International Conference on Coastal Engineering (ICCE) 2018, Baltimore, USA (2018)

National Abstract Accepted Presentations

1. Atak, D., Bezazoglu, S., Baykal, C., **Guler, H.G.**, Guler, I., Ergin, A. "Comparison of Hardly and Fully Reshaping Berm Breakwaters, A Case Study: Ordu-Giresun Airport", Turkish Ocean Sciences Conference 2016, Ankara, Turkey (2016)

2. **Guler, H.G.**, Baykal, C., Ozyurt, G., Kisacik, D. "Effect of Temporal Downscaling Techniques of Wind Speed Data on Wave Hindcasting and Wind Power Potential Models", Turkish Ocean Sciences Conference 2016, Ankara, Turkey (2016)

3. Ozyurt Tarakcioglu, G., Ergin, A., **Guler, H.G**., Baykal, C., Guler, I., Esen, M., Kirezci, C., Yalciner, A.C. "Design Wave and Risk in Coastal Engineering Applications", Turkish Ocean Sciences Conference 2016, İzmir, Turkey (2018)

4. Yalciner, A.C., Annunziato, A., Papadopoulos, G., Dogan, G.G., **Guler, H.G.**, Cakir, T.E., Ozer Sozdinler, C., Ulutas, E., Arikawa, T., Suzen, L., Kanoglu, U., Guler, I., Probst, P., Synolakis, C. "The Bodrum-Kos Earthquake and Tsunami of July 20, 2017: Face of the Event in the Sea", 71th Turkish Geology Congress, Ankara, Turkey (2018)

Poster Presentations

1. **Guler, H.G.**, Ergin, A., Yalciner, A.C. "Comparison of Results of a Selected Possible Tsunami and a Synthetic Extreme Storm Event at Gulf of Iskenderun, Turkey", 26th International Tsunami Symposium 2013, Gocek, Fethiye, Turkey (2013)

2. Ozyurt, G., Kirezci, C., **Guler, H.G.**, Baykal, C., Yalciner, A.C., Pelinovsky, E., Zaytsev, A., Kurkin, A. "Observations of Extreme Waves at South Coast of Black Sea", IUGG General Assembly 2015, Prague, Czech Republic (2015)

3. Ozyurt, G., Yalciner, A.C., Kirezci, C., Baykal, C., **Guler, H.G.**, Erol, O., Zaytsev, A., Kurkin, A. "Recent Extreme Marine Events at Southern Coast of Black Sea", EGU General Assembly 2015, Vienna, Austria (2015)

4. **Guler, H.G.**, Arikawa, T., Baykal, C., Yalciner, A.C. "Numerical Modelling of Solitary Wave Experiments on Rubble Mound Breakwaters", AGU Fall Meeting 2016, San Francisco, USA (2016)

5. **Guler, H.G.**, Arikawa, T., Baykal, C., Yalciner, A.C. "Challenges in Numerical Assessment of Tsunami Impact on Composite and Rubble Mound Breakwaters", International Tsunami Symposium 2017, Bali, Indonesia (2017)

6. **Guler, H.G.**, Liu, X., Jensen, B., Tomaselli, P.D., Baykal, C., Arikawa, T., Yalciner, A.C. "A New Numerical Solver for Simulating Porous Media Flow Based on Immersed Boundary Method", AGU Fall Meeting 2018, Washington D.C., USA (2018)

RESEARCH PROJECTS

- 2012-2015 (Scholar): "Risk Assesment and Design of Prevention Structures for Enhanced Tsunami Disaster Resilience (RAPSODI)", supported by CONCERT Japan Research and Innovation Joint Call Project; Turkish supporter: TÜBİTAK

- 2013-2017 (Researcher): "Assessment, Strategy, and Risk Reduction for Tsunamis in Europe (ASTARTE)", supported by European Union (FP-7 Project)
- 2013-2018 (Researcher): "Earthquake and Tsunami Disaster Mitigation in the Marmara Region and Disaster Education in Turkey" supported by a Japan-Turkey Joint Research Project by SATREPS
- 2018-2020 (Scholar): "Modelling the Motion of Units Forming Rubble Mound Coastal Protection Structures under Wave Attack using Immersed Boundary and Discrete Element Methods" supported by TÜBİTAK 1001 Grants

OTHER ACADEMIC ACTIVITIES

- 2019: Reviewer for "Engineering Applications of Computational Fluid Mechanics" journal
- 2019: Editor of "Coastal Engineering" textbook by Prof. Dr. Ayşen Ergin in collaboration with O. Cabuk and B.U. Senturk
- 2020: Reviewer for "Journal of Natural Hazards and Environment"